CONTROLLING EXCITON EMISSION DIRECTION THROUGH OPTICAL SPIN-ORBIT INTERACTION WITH METALLIC NANOGROOVES

by

Fatemeh HadavandMirzaee

A dissertation submitted to the faculty of
The University of North Carolina at Charlotte
in partial fulfillment of the requirements
for the degree of Doctor of Philosophy in
Optical Science and Engineering

Charlotte

2024

Approved by:

_____
Dr. Tsing-Hua Her

_____
Dr. Greg Gbur

_____
Dr. Tino Hofmann

_____
Dr. Abasifreke Ebong

ABSTRACT

FATEMEH HADAVAND-MIRZAEE. Controlling Exciton Emission Direction through Optical Spin-Orbit Interaction with Metallic Nanogrooves.
(Under the direction of DR. TSING-HUA HER)

The recently introduced class of two-dimensional materials, monolayer Transition Metal Dichalcogenides (TMDs), are emerging as highly promising candidates to enhance data transfer capacity in the field of Valleytronics. Strong “atomic spin-orbit interaction” in monolayer TMDs locks spin of electrons to degenerate valleys with different momenta. These locked valley-spin pairs respond differently to different circular polarizations of light. However, this feature vanishes at room temperature. To address this issue, the coupling between the exciton emissions and photonic modes are under extensive investigation.

This dissertation explores the control over TMD valley-polarized emission by coupling the exciton emission to the plasmonic mode. Specifically, we take advantage of the strong coupling between monolayer WS_2 and metallic nanogrooves to enhance information routing, thereby achieving higher data capacity.

The first part of this study is focused on analyzing the interdependence between the nanogroove parameters and the coupling condition. In the second part, we will demonstrate the k-space separation of valley excitons in monolayer TMDs through the "optical spin-orbit interaction." This separation implies that the helicity of photons determines a preferred emission direction.

This research can serve as a guideline for designing structures and pave the way to transport and read out the spin and valley degrees of freedom in two-dimensional

materials. By addressing current challenges in the field of Valleytronics, it offers guidance for future advancements in this area.

DEDICATION

To those who embody resilience in the face of adversity. To those who never surrender...

ACKNOWLEDGEMENTS

I am deeply thankful to my parents for their endless love and encouragement that have made this achievement possible. Their unwavering support and belief in me have been a constant source of strength. Also deserving of appreciation is Arash, for his encouragement, understanding, and support during both the challenging and rewarding moments of this endeavor. His companionship has been a constant source of motivation and joy.

TABLE OF CONTENTS

LIST OF FIGURES

LIST OF TABLES

LIST OF SYMBOLS/ABBREVIATIONS

2D	Two dimensional
3D	Three dimensional
1L	Single layer
Ag	Silver
Al_2O_3	Aluminum Oxide
Au	Gold
DCP	Degree of Circular Polarization
FDTD	Finite Difference Time Domain
FOM	Figure of Merit
LEB	Lower Energy Branch (E_-)
LH	Left-handed
ML	Multilayer
MoS_2	Molybdenum Disulfide
$MoSe_2$	Molybdenum Diselenide
NPoM	nanoparticles-over-mirror
PL	Photoluminescence
ps	Pico-second
RH	Right-handed
Si	Silicon
SPP	Surface Plasmon Polariton

TE	Transverse Electric
TM	Transverse Magnetic
TMD	Transition Metal Dichalcogenide
UEB	Upper Energy Branch (E_+)
WS_2	Tungsten Disulfide
WSe_2	Tungsten Diselenide
σ^+	Left-handed
σ^-	Right-handed
κ_{chiral}	Chiral coupling strength
θ_c	Coupling angle
θ_g	Groove angle
γ_{pl}	Plasmon linewidth
γ_{ex}	Exciton linewidth
E_{pl}	Plasmon energy
E_{ex}	Exciton energy
g	Coupling strength in coupled oscillator model

CHAPTER 1: INTRODUCTION

While most electronic systems use the electric charge of electron as a carrier, it is feasible to construct devices that utilize other characteristics of electron, instead of charge. In this way, new degrees of freedom are introduced to increase data transfer capacity. As an example, electron spin makes the basis for spintronics in which different spins of electron respond in different ways to an external field [1], [2]. Valleytronics is a relatively newer area of research that exploits materials with multiple equal energy minima levels located at different momentum positions in their band structure. In such material, the regions with minimum energy are practically identical to each other, except for their orientations with respect to the crystal axis. As a result, when electrons are excited from valence to the conduction band, they will have the same energy, yet exhibit different momenta in that region. These energy minima are called valleys and selective population of one momentum-specified valley, referred to as valley polarization, makes the foundation of Valleytronics [3].

In general, due to the weak coupling between valley state of a particle and any externally applied field, targeting valleys is not straightforward and detailed study to address the issue is desired. In this research, we investigate the potential of a strongly coupled layer of 2D semiconductor material with an array of metallic nanogrooves for efficient applications in Valleytronics. The current chapter will introduce the study by first discussing the research context and problems followed by the literature survey, the research objectives and finally the significance of the work.

1.1 Research context

1.1.1 Transition Metal Dichalcogenides (TMDs) in Valleytronics

Although the concept of using valley index as an information carrier was initially proposed in the study of conventional semiconductors like Silicon and Aluminum Arsenide [4], yet these materials do not exhibit strong coupling between valley index and an external field. Since the discovery and isolation of graphene and its unique electric and optical properties in 2004 [5]–[7], it has been widely considered as a possible solution for Valleytronics. However, in addition to spin degeneracy, we need a kind of material with asymmetric structure to differentiate between two valleys. Although graphene has the required degenerate valleys, the inversion symmetry of the material (Fig. 1.1) must be broken to be functional in Valleytronics applications [8], [9].

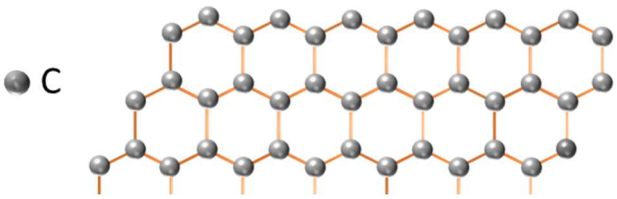

Fig. 1.1 Graphene hexagonal structure.

A recently introduced class of materials, monolayer Transition Metal Dichalcogenides (TMDs), with the hexagonal graphene-like structure (Fig. 1.2a), along

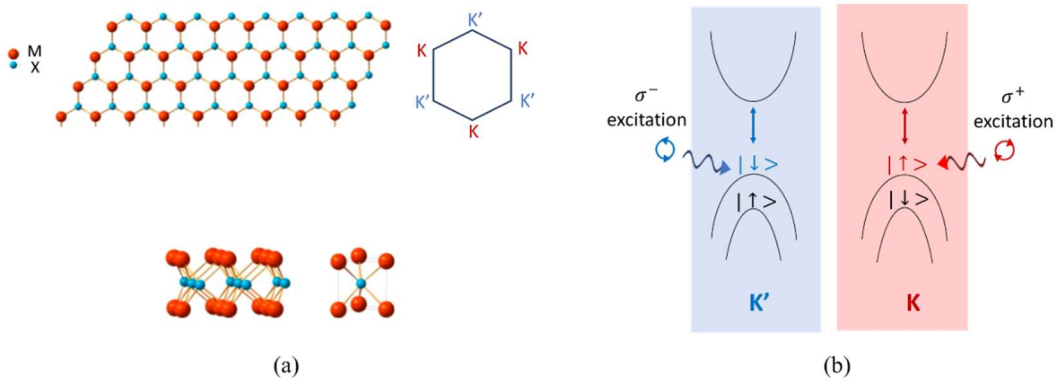

Fig. 1.2 (a) The crystal structure of a typical TMD. Upper panel: Top view of the lattice and the band structure at the band edges located at the K′ and K locations. Lower panel: 3-D unit cell view. (b) A schematic preview of the optical selection rule in TMD band structure. $\boldsymbol{\sigma^-}$: Right-handed (RH) excitation. $\boldsymbol{\sigma^+}$: Left-handed (LH) excitation.

with intrinsic broken inversion symmetry, have become a more promising candidate for Valleytronics [10]–[12]. Monolayer TMDs are atomically thin semiconductors of the type MX_2 with one layer of M atom (a transition metal atom like Mo, W, etc.) sandwiched between two layers of X atoms (a chalcogen atom like S, Se, etc.). These materials have a direct band gap with two energy degenerate valleys (Labeled by K and K′) in the visible to near infrared region. Due to the lack of inversion symmetry in these materials, a strong "atomic spin-orbit coupling" is observed that traps electrons with opposite spins at different valleys (see Fig. 1.2b). These locked valley-spin pairs, named "valley pseudospins", respond differently to different circular polarizations of light (optical spin angular momentum or helicities). In simple words, the right-handed (RH $:\sigma^-$)/ left-handed (LH $:\sigma^+$) circularly polarized light excites the valley located at K′/K [13], [14]. Due to the the time-reversal symmetry ($\mathbf{K}' = -\mathbf{K}$), the excited electron in each valley will have opposite **k**-vector. Fig. 1.3 is the pictorial explanation of this feature. Generating two

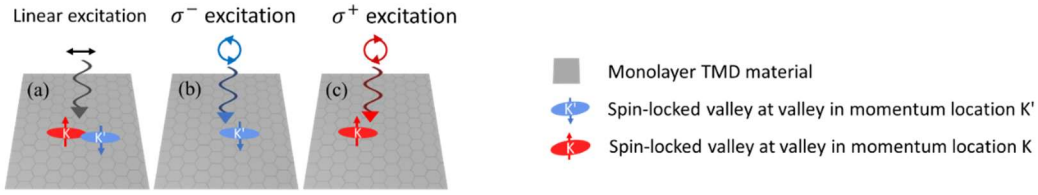

Fig. 1.3 The electrons excited in each valley with opposite **k**-vectors will propagate in opposite directions. (a) Linear excitation light (b) σ^-excitation. (c) σ^+ excitation.

distinguishable circular polarizations provides us with a binary system with potential applications in data encoding.

However, there are two challenges compromising the application of Valleytronics! 1- short propagation length & 2- fast depolarization of these valley-polarized exciton emissions at room temperature. At room temperature the exchange of phonons can supply the momentum required for inter-valley scattering (transition of electrons between valleys **K** ↔ **K′**) and disrupt the distinguishability of the two valleys [15]. Therefore, it is not easy to spatially transport the valley information except in cryogenic temperatures, which limits the applications [14], [16], [17].

It is known that the emission of a quantum emitter can be modified by the local photonic environment due to light-matter interactions [15]. Therefore, by strongly couple TMD excitons (matter) to a resonant cavity mode (light), an enhanced valley polarization for TMD excitons at room temperature can be achieved.

1.1.2 Strong coupling between TMD excitons and plasmonic modes

A strong coupling between light and matter occurs when coherent energy exchange between the two components exceeds the rate of losing energy to the medium [18]–[20]. As half-light half-matter particles, the newly formed states combine the advantages of

photons, such as negligible effective mass, fast propagation, and high spatial and temporal coherence, with the properties of matter, like strong interparticle interactions. These features make them good candidates to enhance light-matter interactions for applications such as all-optical switches, quantum information processing, etc. Such strong couplings between an emitter and resonant cavity modes have already been reported in Fabry-Perot cavities [21], semiconductor microcavities [22]–[24] and photonic crystals [25], [26]. In contrast to these mentioned structures, surface plasmons supported by plasmonic nanostructures can compress light in to a subwavelength region and provide ultrasmall mode volumes [27]–[30]. Moreover, they perform pretty well in ambient conditions. The strong coupling between plasmonic nanostructures and molecular excitons at room temperature have been reported in the literature [31]–[36].

The spectral indicator of strong coupling between two states (here light and matter) is the splitting of the -hybrid structure- absorption band into two new polaritonic states, corresponding to upper (E_+) and lower (E_-) polaritonic states (Fig. 1.4a). This phenomenon is evidenced by the anti-crossing dispersion in the angle resolved absorption spectra. The amount of energy splitting between these states quantifies the coupling strength (g) and is called **Rabi energy ($\hbar\Omega_R$)**. Fig. 1.4b shows the absorbance spectra of individual systems of light and matter, and the consequence of strong coupling between them. Fig. 1.4c schematically explains strong coupling between a nondispersive exciton and a dispersive photonic mode [37].

In general, the coupling strength is enhanced by increasing the number of coupled excitons ($g \propto \sqrt{N}$) to the cavity mode or coupling to a highly confined mode with

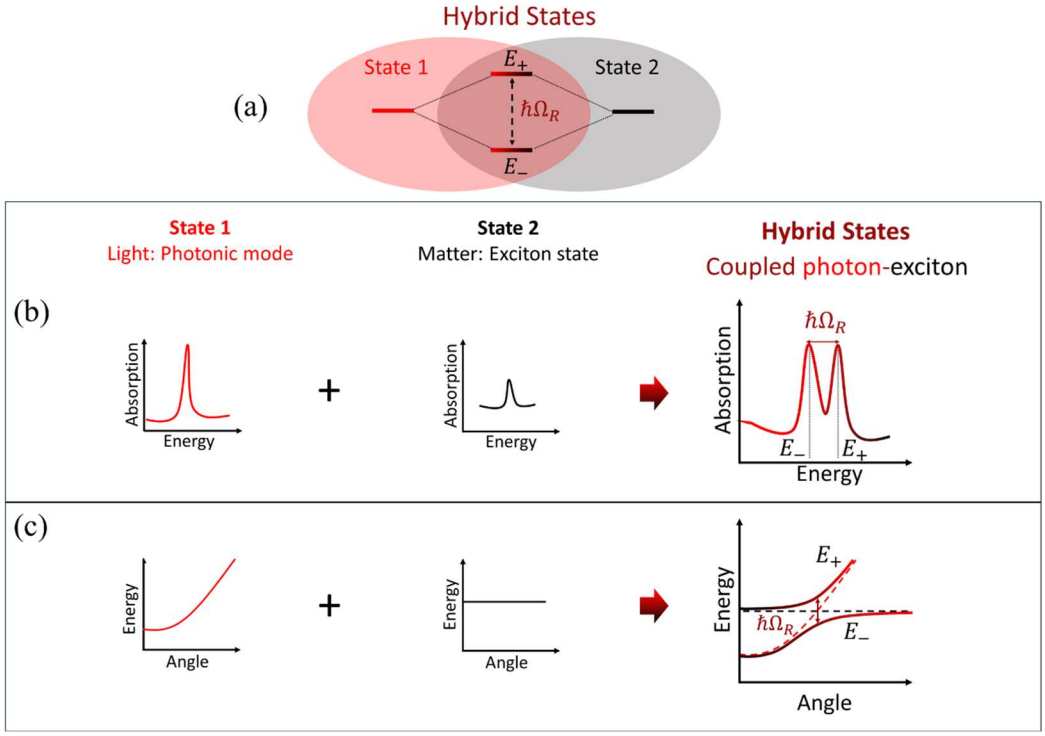

Fig. 1.4 (a) Formation of hybrid states as the result of the coupling between light and matter. (b) Absorbance spectra of an individual photonic resonance (light), excitonic resonance (matter), and the resultant coupled resonances. (c) Strong coupling between angle-dispersive photonic mode and nondispersive excitonic mode.

ultrasmall mode volume ($g \propto \frac{1}{\sqrt{V}}$) [15], [32], [33], [38]. Therefore, by providing a proper condition for strong coupling between monolayer TMD excitons and metallic nanostructures we can achieve collectively large number of excited excitons (N), with strong localization due to the small mode volume (V) feature in plasmonics. This partnership shapes plasmon-exciton hybrid states and can help short-lived valley-polarized excitons in monolayer TMDs survive up to room temperature.

In addition to the PL enhancement, when guiding the plasmon-excitons, the mediating nanostructure must also preserve the valley polarization of TMD exciton

emissions. In the next section, the ability of plasmonic nanostructures to maintain valley polarization will be discussed.

1.1.3 Chiral plasmonics and optical spin-orbit interaction

Optical spin-orbit interaction locks optical spin and the direction of propagation of the electromagnetic wave together in the presence of chiral polarization. Such coupling between the light polarization and its spatial properties is known as optical spin Hall effect, analogous to the classical Hall effect observed in the motion of charged particles in a magnetic field. This feature has been exploited during the last few years [39], [40]. The polarization-dependent propagation direction can be visualized through the near-field interference resulting from the vectorial nature of the exciting field [41]. If we assume a dipole close to a waveguide, the selective excitation of waveguide modes propagating in different directions can be achieved by destructive and constructive near-field interference or -in other words- interference between the evanescent components of the field. It has been demonstrated that circular dipoles with opposite polarizations and an out-of-plane component ($P_x \pm iP_z$) can couple to the guided modes propagating in opposite directions in a waveguide (Fig. 1.5) [41]. Based on the handedness of the polarization, the circular dipole can provide destructive interference in one specified direction and the propagation

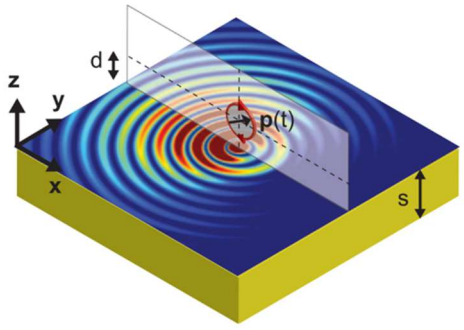

Fig. 1.5 Asymmetric excitation of the plasmonic mode by an out of plane circular dipole.

of a mode in the opposite direction. This is what we call “control over the direction of propagation of the guided mode”.

One may ask if the plasmonic structures exhibit such distinct responses to different circular polarizations of light, why do we bother using TMDs to achieve control over directionality? Well, due to the loss issue in plasmonics, we need field enhancement through strong coupling between the plasmons and excitons. However, the second and the more important reason is that such near-field interference picture can only be realized by the vectorial character of the exciting field source at the close proximity of the waveguide (here plasmonic nanogrooves). When we illuminate the hybrid structure (nanogrooves – TMD on top) with laser, the valley-polarized excitons of the TMD serve as circularly polarized dipole sources at subwavelength distance from the plasmonic nanostructure.

With these concepts in mind, we started to investigate the potential of such hybrid structure to alleviate the problem of valley depolarization in the context of Valleytronics applications. Next section is dedicated to a summary of the literature on the strong coupling between TMDs and plasmonic nanostructures, particularly for the purpose of valley polarized exciton routing.

1.2 Literature review

In this section we review the existing relevant literature and the relation to this research to identify the research aims we are targeting. As mentioned in the previous section, monolayer TMDs with degenerate valleys are good candidates for the applications in

Valleytronics. However, their strong phonon-assisted intervalley scatterings limit their applications in room temperature. Several structures have been implemented to help monolayer TMDs maintain their valley polarization in room temperature, but plasmonic nanostructures seem to be more efficient. Thanks to their very small mode volume which makes the coupling between plasmons and excitons very strong.

What follows is a brief survey summarizing: first, the recent efforts made in design and implementations of strong plasmon-exciton couplings in plasmonic nanostructures and TMDs, and second, the steps taken to achieve control over the TMD exciton emission through its interactions with plasmonic nanostructures at room temperature.

1.2.1 Strong coupling in TMDs and plasmonic nanostructures

As mentioned earlier, in light matter interactions, a strong coupling regime is the condition in which the rate of energy exchange between light and matter is fast enough to overcome the decay and dissipation rates. In this regime, the energy exchange between light and matter leads to vacuum Rabi splitting of the hybrid light-matter states. From the broader scope of strong coupling between two-dimensional semiconductors and photonic modes, we focus on the strong plasmon-exciton coupling between monolayer TMDs and plasmonic nanostructures. On the excitonic side, monolayer TMDs are the winner because of their direct bandgap, optical stability, large dipole moments and binding energy, relatively ordered transition dipole moment orientation and other intriguing features like the valley degree of freedom [42], [43]. From the photonic side, plasmonic nanostructures and nanocavities support surface plasmon polaritons and can overcome the diffraction limit to achieve sub-wavelength mode volumes.

The conventional idea of energy detuning between the resonance energy of plasmonic structures and TMDs was based on utilizing different samples with different resonance spectrums to match the TMD resonance, statistically. This approach is not ideal since it suffers from uncertainties due to different sample inhomogeneities, etc. From the very first tunable coherent coupling between single nanoparticles and monolayer TMDs, is the experimental study from Zheng et al [44], which was performed in 2017. This group have successfully measured the dispersion relation of the plasmon-exciton for a single silver nanorod strongly coupled with a monolayer WSe_2 (tungsten diselenide) by continuous deposition of alumina layers and measuring the corresponding scattering spectra (Fig. 1.6a). By successive deposition of alumina, the plasmon resonance redshifted to cross the WSe_2 exciton peak (Fig. 1.6b, Fig. 1.6c). In this way they could tune the strong coupling between excitons and plasmons and a Rabi splitting of 49.5 meV was achieved (Fig. 1.6d). The above study shows the anti-crossing behavior in the dispersion as an indicator of coherent energy exchange between excitons and plasmons, however, the detuning approach is not reversible. To perform such active and reversible control over

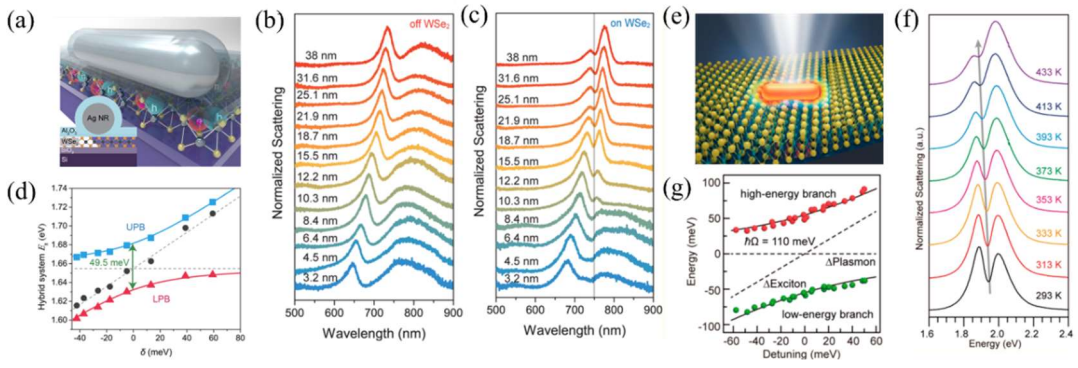

Fig. 1.6 (a) Ag nanorod-WSe_2 structure. (b),(c) The variations in the scattering spectra of Ag nanorod with successive alumina deposition without and with WSe_2, respectively. (d) The energy dispersion of the hybrid plasmon-excitons of the Ag nanorod-WSe_2 structure showing anti-crossing feature.(e) Au nanorod- monolayer WS_2. (f) Scattering spectra of the Au nanorod-WS_2 by temperature variations. (g) Energy splitting as the result of plasmon-exciton strong coupling.

the coupling, Wen et al [45] reported a temperature dependent tunable coupling between gold nanorod and monolayer WS_2 (tungsten disulfide) (Fig. 1.6e). The resonance of their structure was controlled by scanning the temperature and they were able to achieve Rabi splitting energies of 91-133 meV from the structure scattering spectra (Fig. 1.6f and Fig. 1.6g). Later in another study [46] they reported 1187-fold photoluminescence (PL) enhancement for the light emitted from the hybrid structure compared to a bare monolayer WS_2.

Although convenient tuning for the strong coupling between individual plasmonic nanoparticles and TMD excitons was reported by mentioned groups, several other works have also studied the strong plasmon-exciton coupling in TMDs and nanoparticles-over-mirror (NPoM) as depicted in Fig. 1.7 [34], [47]–[50]. The reason is that a typical plasmonic cavity made from placing nanoparticles over a flat metal film can confine the electric field to within a very small volume below 10^{-7} $(\lambda/n)^3$ in the nanogap between the particle and the metal plate [51]. As mentioned earlier, small mode volume is desired for strong coupling strength in plasmon-excitons. In such structures, the tuning is generally

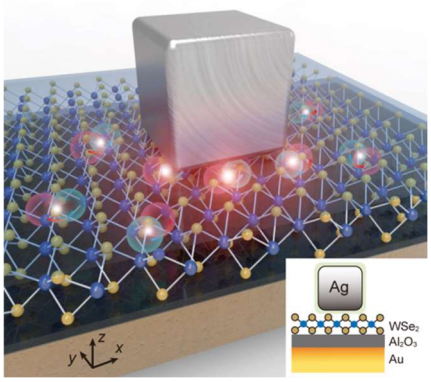

Fig. 1.7 The schematic of NPoM coupled with a monolayer TMD.

achieved through varying the size and shape of the nanoparticles and also by changing the thickness of the nanogap between the nanoparticle and the mirror.

In addition to the strong coupling, the confined mode volume can effectively decrease number of excitons to a single emitter level [49], for some applications like single atom lasers [52], single photon switches [53], [54] and quantum information processing [55]. In this regard Sun et al [49] observed the coherent coupling in a system of nanocube-over-mirror and WSe_2 by tuning the alumina coating in the gap between the gold film for various sizes of silver nanocubes. Although their achieved coupling was at the border of the weak and strong coupling regime (intermediate coupling regime) with Rabi splitting of 36.7 meV, they were able to get a large brightness for the PL emission. Later other researchers showed strong coupling of plasmon-excitons for the same structure of nanocube-over-mirror, with other TMDs. Han et al [34] were able to achieve Rabi splitting of 145 meV for the strong coupling within silver nanocube-over-silver and monolayer WS_2. They controlled the nano gap thickness and nanocube size to adjust the plasmonic resonance to match monolayer WS_2 exciton resonance. One year later, Hou et al [48] showed continuous transition from weak coupling regime to strong coupling regime with Rabi splitting up to 190 meV for the hybrid structure of MoS_2 and silver nanocube-over-gold plate.

Because of the orientation mismatch between the plasmonic field (mainly out of plane) and monolayer TMD excitons transition dipole moments (in plane) [43], [56], the resultant coupling is not usually strong enough, however, it improves by increasing TMD layers [47]. On the other hand, plasmonic periodic arrays offer significant benefits,

including local field enhancement through localized surface plasmon resonance by orders of magnitude, along with high quality factor for its coupled lattice resonances. Therefore, they appear to be promising components for a strong plasmon-exciton coupling. In 2016, Liu et al [36] demonstrated strong coupling between array of silver nanodisks and monolayer MoS_2. The strength of the coupling was controlled by the geometry of the nanodisks and Rabi splitting of 58 meV at 77 K was achieved. Although showing decline in strength, the strong coupling could survive up to the room temperature. In the same year, room temperature splitting up to 60 meV by coherent coupling of gold hole arrays and monolayer WS_2 was also reported [35]. In 2019, another group could improve the Rabi splitting of their structure from 85 meV to 300 meV at room temperature [57]. A flat silver mirror, MgF_2 spacer as a substrate for monolayer WS_2, and periodic array of silver nanodisks were employed (Fig. 1.8a). They somehow combined the idea of strong coupling between monolayer TMDs with plasmonic NPoM and arrayed nanostructures, making arrayed nanoparticles-over-mirror. Then, they achieved ultra strong coupling by placing the Ag-WS_2 heterostructure in an optical cavity to enhance the coupling (Fig. 1.8b). This is an example analogous to a system of 3 coupled oscillators (Fig. 1.8c), supporting 3 kinds of resonance between Exciton, plasmonic mode and the cavity mode.

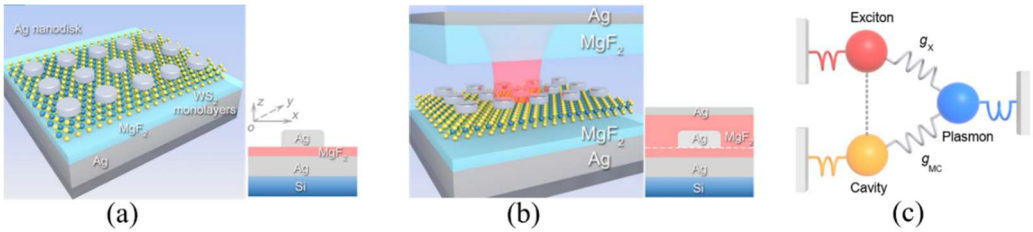

Fig. 1.8 (a) 1L WS_2 on top of the periodic array of Ag nanodisks. (b) Ag-WS_2 heterostructure in an optical cavity. (c) Three coupled oscillator model.

Finally, another group demonstrated strong coupling with Rabi splitting up to 86.5

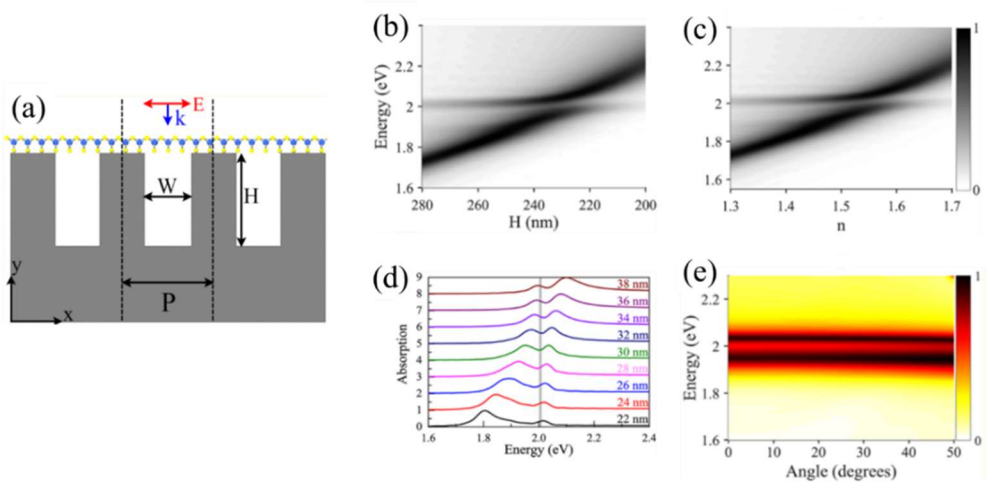

Fig. 1.9 (a) The side-view of the structure used to investigate the strong coupling between nanogrooves and 1L WS_2. (b-e) Absorption spectra of the hybrid structure with different (b) nanogroove depth, (c) medium refractive index, (d) nanogroove width and (e) incident angle.

meV for a hybrid structure of monolayer WS_2 and deep nanogrooves carved on a silver slab [58]. They investigated the strong coupling condition relation to the nanogroove depth, width and refractive index of the dielectric filled in to the nanogrooves, using TM polarized incident light (Fig. 1.9a-e). In their results they reported angle independent strong coupling within such structure (Fig. 1.9e).

The proposed structure is similar to the structure we are mainly investigating in the first part of this thesis. However, there are some points to mention. Firstly, They only investigated the TM polarized incident light in *xz* incident plane, meaning that they just considered the plasmonic modes travelling along the periodic direction (*x*). Providing a proper incident condition, *i.e.* TE polarized light in *yz* incident plane, such a structure can also support guided plasmonic modes along the grooves, which are known as channel polaritons [59], [60]. Fig. 1.10a and Fig. 1.10b picture the two kinds of supported modes

within a plasmonic nanogroove array. In the pictures θ_{inc} represents the angle between **k**-

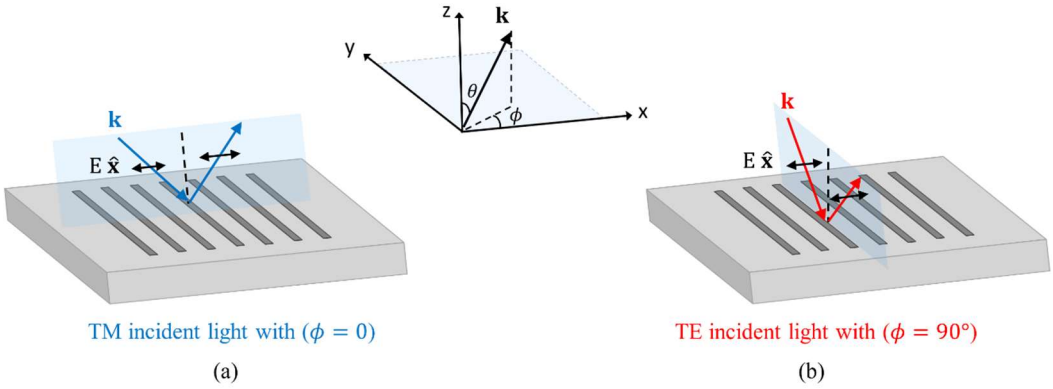

Fig. 1.10 The incident light **k**-vector (a) for the case with ϕ_{inc} = 90°, in which the incident **k**-vector has k_y (along the grooves) and k_z components. (b) for the case with ϕ_{inc} = 0, in which the incident **k**-vector has k_x (perpendicular to the grooves) and k_z components.

vector and normal to the surface and ϕ_{inc} measures the angle between the projection of **k**-vector on the surface and x-axis. TM and TE incident lights are chosen such that the electric field at the illuminated point is always along the periodicity of the structure [61].

Second, they have reported angle independent strong coupling in the structure because the magnetic field of the TM-polarized light does not change by changing the angle of incidence. We would challenge their justification with our results using TM-polarized light with other groove parameters and attribute "the angle independent coupling" limited to structures with specific parameters as theirs. Having said this, their result is not inclusive. Lastly, in addition to the mentioned parameters, we are taking into account the effect of more groove parameters, like groove wall angle and groove edge-roundness which are inherent to the nanoscale fabrication process.

In the next section we review the literature about the second part of this dissertation, which is achieving control over the TMD exciton emission direction through its interactions with plasmonic nanostructures at room temperature.

1.2.2 Separation of valley-polarized excitons

As mentioned in section 1.1, among many interesting properties of monolayer TMDs, is their valley dependent optical selection rule [62], *i.e.*, the electron located in their K′ and K valley can only be excited by right and left circularly polarized light, respectively. This feature provides monolayer TMDs with an additional degree of freedom, which makes them very promising for opto-electronic applications involving information storage and transfer [15]. The valley optical selection rule in monolayer TMDs has already been proved through several experimental studies [14]–[17], [63] at low temperature up to 90 K. However, due to the intervalley scatterings, the demonstration of this feature at room temperature faces restrictions. Recently, researchers have started to employ the coupling between monolayer TMD excitons and photonic modes not only to maintain the feature at room temperature [64], [65], but also to direct the valley polarized exciton emission to different directions. In 2017, Chen et al, [66] used a dielectric microcavity strongly coupled with monolayer MoS_2 to achieve the exciton valley-polarization at room temperature. Dielectric metasurfaces have also been investigated for this purpose [67]. Since the purpose of this thesis is plasmon assisted-valley exciton emissions, we mainly focus on the literature about valley-polarized exciton routing achieved with spin-orbit coupling in metallic structures.

The very first report of showing coupling (not STRONG coupling) of valley-polarized excitons in TMDs and plasmonic nanostructures at room temperature was the

research published in early 2018 by Gong et al [68]. This group used a few layers of WS_2 in the vicinity of a plasmonic nanowire and they were able to achieve spatial separation of valley index by directionally guiding light (Fig. 1.11a). In their structure, the propagation direction of the plasmonic guided mode of the nanowire was determined by a combination of the exciton position (in y) and helicity of the incident light as shown in Fig. 1.11b. Fig. 1.11c, d show the fluorescence images of the emission of valley polarized excitons and line cuts of the intensity profiles under left and right-handed circular polarization excitation, respectively. To quantify the directionality as a function of the position of the excitons, they defined experimental valley dependent directionality (κ_{exp}) by $\kappa_{exp}(y) = \frac{[I_L(y) - I_R(y)]}{[I_L(y) + I_R(y)]}$, where $I_L(y)$ and $I_R(y)$ are the peak intensities at the left and right end of the nanowire, showing the amount of emission which is coupled to the left- and right- propagating plasmonic modes. From Fig. 1.11e, f is clearly observed that for the same excitation spot (y), with opposite excitation helicities, the exciton emission couples to plasmonic modes propagating in opposite directions. In other words, a σ^+ (σ^-) polarized source near the nanowire at $y > 0$ will excite surface plasmon polariton (SPP) propagating to the left (right). The effect is inverted when the source is positioned at $y < 0$. So, the propagation direction of the mode in the nanowire is locked to the helicity of the incident light in the presence of the layered WS_2. In this way, valley information can be transferred to other valley devices on a chip for Valleytronics applications.

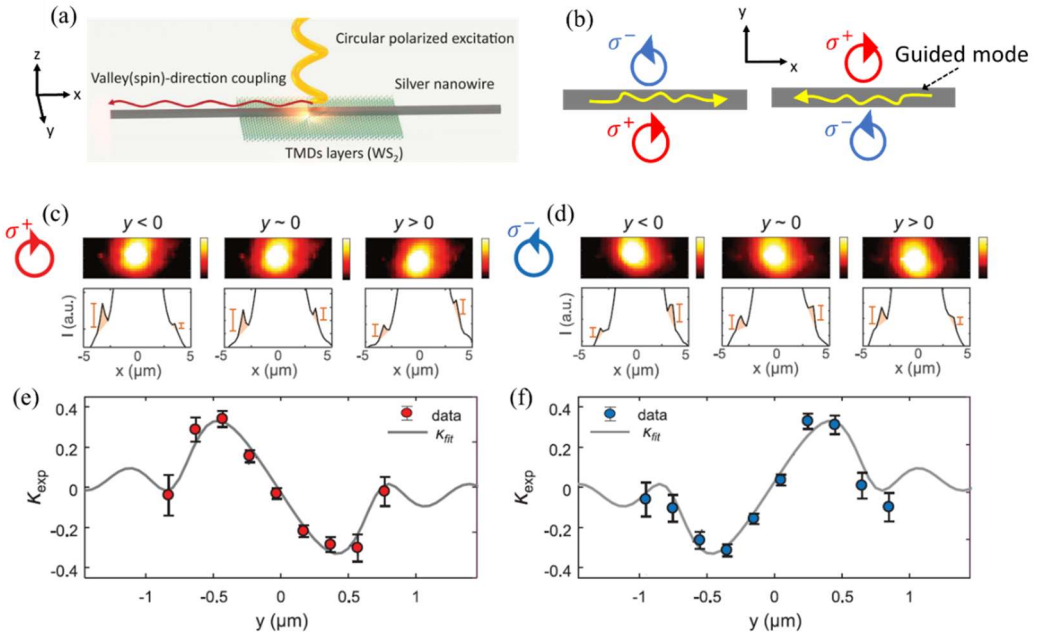

Fig. 1.11 (a) Conceptual demonstration of valley-polarized exciton emission in WS_2. (b) Illustration of the directional propagation, which is dependent on the exciton position and incident light helicity. (c, d) The fluorescence image of the valley polarized exciton emission and line cuts of the intensity profiles under (c) left- and (d) right-handed circular polarization excitation. (e, f) Directional coupling efficiency as the function of position with (e) left- and (f) right-handed circularly polarized incident light.

Although, the valley exciton separation is demonstrated in the mentioned study, the direction of valley separation highly depends on the position of the excitation laser spot relative to the nanowire, restricting the applications of the approach. Later in 2019, another group [69] demonstrated a more general design of a hybrid structure consisting of monolayer MoS_2 and plasmonic metasurface (asymmetric groove arrays as shown in Fig. 1.12a) to achieve separation of valley excitons (ρ) up to 18% (Fig. 1.12e). They did not observe any exciton valley polarization for the MoS_2 over symmetric nanogrooves (Fig. 1.12c) and MoS_2 over flat metal surface (Fig. 1.12d) at room temperature. However, by placing MoS2 on top of the asymmetric nanogrooves, it was not only valley excitons that

were separated in real space (Fig. 1.12b); emitted photons with different helicity were also separated in momentum space. They concluded that this valley index separation is facilitated by near-field coupling between excitons and guided surface plasmon polariton modes propagating along the grooves (channel polaritons).

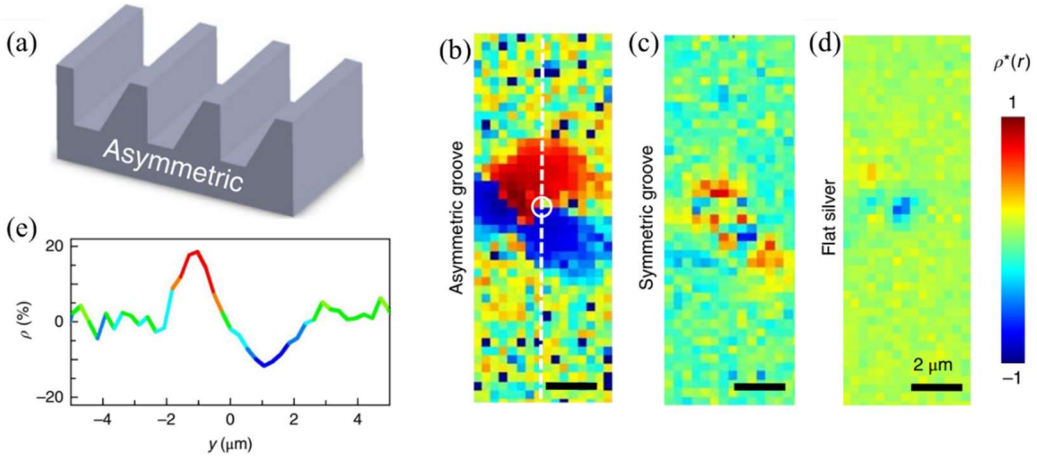

Fig. 1.12 (a) Asymmetric nanogroove array used to excite guided SPPs by circularly polarized light. b-d, Color plots of valley polarization contrast in real space measured for (b) MoS_2 asymmetric nanogrooves (c) MoS_2 symmetric nanogrooves and(d) MoS_2 flat silver film.

In another attempt, Chervy et al [70] designed and fabricated a sample with WS_2 over a plasmonic metasurface with rotated rectangular nanoapertures (Fig. 1.13a) that yielded exciton-valley contrast up to 40% at room temperature at the onset of strong coupling regime. The valley contrast persisted even after 200 ps lifetimes, while bare TMD valley polarized exciton lifetime is less than 10 ps [68]. As shown in Fig. 1.13b, the angle-resolved reflection spectra demonstrated a Rabi splitting of around 40 meV. As the result of the coupling, the momentum of the surface in the plasmonic array is locked to the valley degree of freedom in WS_2. This can be shown clearly in the angle resolved

differential left and right circularly polarized PL spectra in Fig. 1.13c. The optical spin–orbit interaction locks SPP modes propagating along $+x(-x)$ with the photon helicity $\sigma = +1(-1)$.

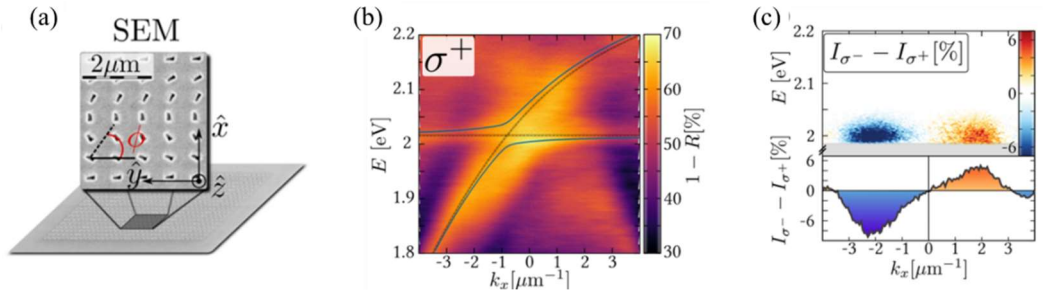

Fig. 1.13 (a) The plasmonic metasurface with ϕ-rotated rectangular nanoapertures. (b) Angle-resolved absorption spectrum of the sample analyzed in left circular polarizations, with the best fit drawn. (c) Angle-resolved differential left and right circularly polarized PL spectra.

The literature mentioned here demonstrates that the plasmonic structures are suitable to be used to control the valley index of freedom. The performance of these systems is dependent on SPPs propagation guiding feature, the ultrafast dynamics of excitons and howe these two states are entangled through plasmon-exciton coupling. Our approach differs from these studies as neither of them operated in a strong coupling regime. Additionally, the research on asymmetric nanogroove arrays [69] asserts that symmetric arrays are incapable of separating valley-polarized excitons. Here, we are designing simple symmetric nanogrooves within the strong coupling regime to achieve the same valley-polarized exciton routing with a different detection mechanism.

1.2.3 Summary of the literature review

In this section we reviewed the recent work on the role of plasmonic nanostructures to enhance and maintain the TMDs valley-polarized exciton emission. Enhancing the TMD exciton at room temperature is the base of the issue, maintaining and routing the valley polarized exciton emission at room temperature is the second order issue which needs to be resolved. The former problem is extensively investigated through numerous research on strong coupling between TMDs and various plasmonic nanostructures which is summarized in Table 1.1. However, the research on the latter is less extended. In Table 1.2 the literature about employing plasmonic nanostructures to direct and spatially separate TMDs valley polarized exciton emission is summarized.

Table 1.1 Summary of the literature on the strong coupling between TMDs and plasmonic structures.

Coupling mechanism	Advantage	Year	Structure	Distinct feature	Conclusion
Plasmon-exciton coupling with single nanoparticles	The simplest and basic structure	2017 [44]	Ag nanorod-1L WSe_2	Tunability through successive deposition of dielectric layer	Close to strong coupling $\hbar\Omega_R$=49.5 meV
		2017 [45]	Au nanorod-1L WS_2	Active control on tuning with temperature	Strong coupling achieved at room temperature. $\hbar\Omega_R$=91-133 meV
		2020 [46]		PL intensity enhancement and spectral broadening observed by strong coupling.	Strong coupling signature in PL emission was demonstrated.
Plasmon-exciton coupling with nanoparticles -over- mirror	Extremely small mode volume Good for single photon-exciton base coupling	2017 [47]	Au nanoparticle@ Au- ML WSe_2	Multilayer TMD gave better coupling with NPoM structure	Multilayer TMD better for NPoM structures
		2018 [49]	Ag nanocube @ Au-1L WSe_2	Increased confinement by shrinking nanocube size	At the border of strong coupling $\hbar\Omega_R$=36.7 meV
		2018 [34]	Ag nanocube @ Ag- 1L WS_2	Achieved strong coupling by adjusting spacer and nanocube size	$\hbar\Omega$R=145 meV at room temperature
		2019 [48]	Ag nanocube @ Au-1L MoS_2	Showed transition from weak to strong coupling by successive changing thickness of spacer	Largest Rabi to date $\hbar\Omega_R$=190 meV
		2020 [50]	Au nanoprism @ Au- 1L WS_2	Exciton # reduced to single digit. Good for quantum Q-bits	$\hbar\Omega_R$=163 meV at room temperature
Plasmon-exciton coupling with periodic arrays	Different types of resonances: (Lattice and individual resonance) more tunability	2016 [36]	Ag nanodisk arrays- 1L MoS_2	First observation of SPPs -MoS_2 exciton strong coupling by three resonances: Exciton-plasmon- lattice	Not very obvious splitting . at room temperature
		2016 [35]	Au hole arrays- 1L WS_2	Achieved room temperature splitting	$\hbar\Omega_R$=60 meV at room temperature
		2019 [58]	Ag deep nanogrooves- 1L WS_2	Thorough theoretical/numerical study of the effects of groove width, depth, and groove filling index on the strong coupling	Angle independent strong coupling?
Plasmon-exciton coupling with more complex structures	More degrees of freedom to enhance coupling	2019 [57]	Ag nanodisk arrays @ Ag- Inside FP cavity- 1L WS_2	Enhanced coupling by 3 coupled oscillator model: Exciton-plasmon-FP microcavity	Very large Rabi splitting up to 300 meV.
		2021 [30]	Ag nanodisk arrays @ Si_3N_4/SiO_2 1L WS_2	Enhanced coupling by 3 coupled oscillator model: Exciton-plasmon-dielectric waveguide	

Table 1.2 Summary of the literature on TMD exciton routing using plasmonic structures.

year	Structure	Result
2018 [68]	Ag nanowire – ML WS_2	Propagation direction of the nanowire guided mode is determined by a combination of excitation spot location and the chirality of incident light. Achieved valley dependent directionality up to 35%. Not in strong coupling regime.
2018 [70]	Plasmonic rotated rectangular nanoapertures -1L WS_2	Valley polarized exciton-plasmon was achieved at room temperature *close to the strong coupling regime.*
2019 [69]	Asymmetric Ag nanogrooves – 1L MoS_2	Nonradiative energy transfer between exciton-SPP caused room temperature valley polarization up to 18%. Not in strong coupling regime.
2019 [71]	Ag nanowire – ML WS_2	Routing of a chiral Raman signal into propagating surface plasmon polaritons along a silver nanowire based on spin-orbit interaction of light.

1.3 New platform for valley-polarized plasmon-exciton routing

1.3.1 Aims and objectives

As mentioned in the previous section, researchers have started employing integrated plasmonic nanostructures and TMDs to lay the foundation for Valleytronics, given that such hybrid structures perform very well at room temperature [15], [72]. However, this field of research is pretty new and there have been few clear directions for future research. Ideally, a simple plasmonic nanostructure without complicated and detailed components for fabrication purposes, with high performance in guiding the encoded information is desired. There is still a need to explore the potential and efficiency of different platforms for applications in Valleytronics.

Recently, our collaborators in Taiwan used a platform to investigate exciton routing and propagation angle (θ_{SPP}) on the surface. The experimental setup consists of an array of carved nanogrooves on the surface of a silver slab and a layer of WS_2 on top of it. The valley excitons generated by illuminating the monolayer WS_2 (alone) with a linearly polarized light are expected to have equal populations at both K and K′ valleys (Fig. 1.14a). The idea is that, with the proper design of a simple plasmonic nanostructure, we can enhance and direct the WS_2 exciton emissions from K and K′ valleys to different in-plane directions (based on their helicity) at room temperature (Fig. 1.14b, Fig. 1.14c). To aim for an efficient design, a complete knowledge of the light behavior in response to varying the geometrical parameters of the structure, such as period, width, and depth, is essential.

As shown in Fig. 1.16 and Fig. 1.15, in the experimental result, the propagation of valley emissions was detected for two nanogroove samples with different groove periods (Λ), widths (w), and depths (d). Fig. 1.16a and Fig. 1.15a show the unpolarized PL image of the two samples which does not indicate any asymmetry in k-space, as expected. Then,

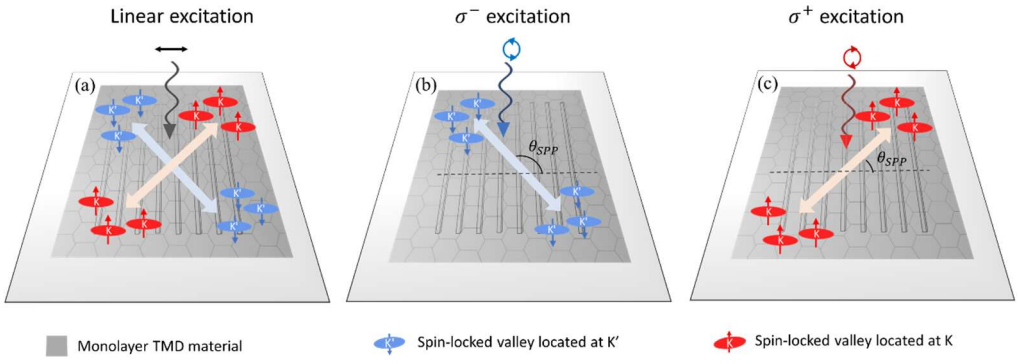

Fig. 1.14 The valley-exciton emission generated by illuminating the combination of monolayer TMD-Plasmonic structure. (a) Excitation by linearly polarized light excites exciton populations from K and K′ valleys in TMD, equally (b, c) Excitation by (b) right-handed and (c) left-handed polarized light just excites the population in K′ and K (K′ = -K), respectively. The role of the plasmonic structure is to propagate the coupled excitons and plasmons, to transfer information.

polarization-resolved k-space images were captured using a combination of polarizers and waveplates in the detection path. As is evident in Fig. 1.16b, Fig. 1.15b and Fig. 1.16, Fig. 1.15c, the propagation direction is different for right-handed (σ^-) and left-handed (σ^+) components of the PL emission. While the experimental results clearly show the spin-dependent direction of light propagation on the x-y plane, a complete investigation is needed to understand the relationship between the plasmonic nanogrooves' parameters and the performance of the system.

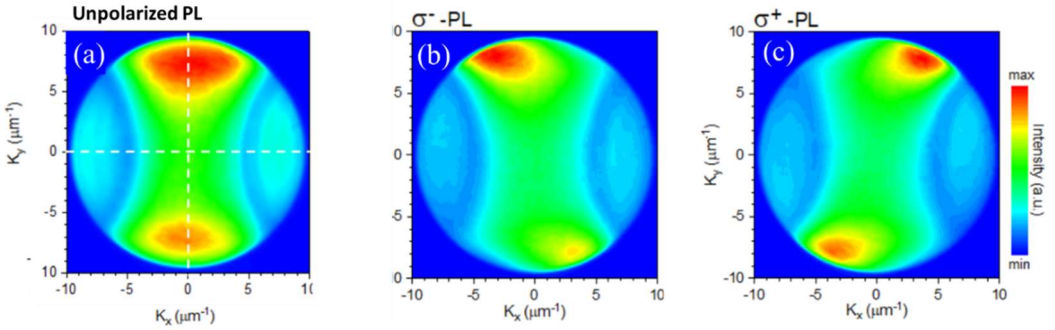

Fig. 1.16 Experimental k-space PL image of a sample with nominal values of Λ=400 nm, w=50 nm and d=70 nm (a) Unpolarized PL. (b) Right-handed PL. (c) Left-handed PL.

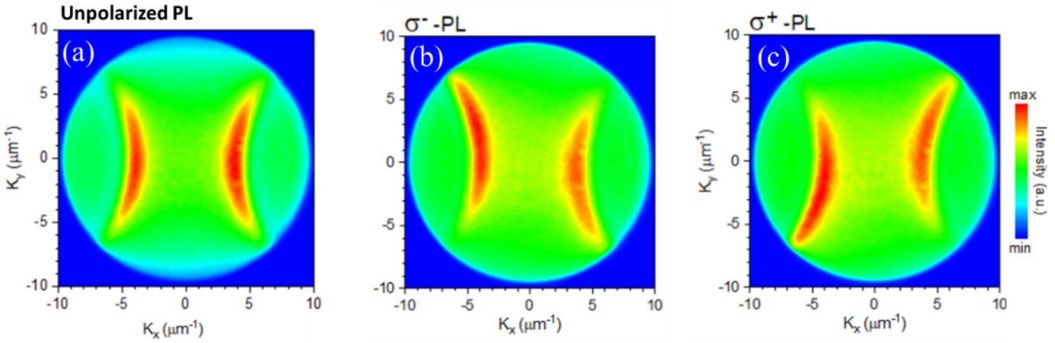

Fig. 1.15 Experimental k-space PL image of a sample with nominal values of Λ=400 nm, w=40 nm and d=30 nm (a) Unpolarized PL. (b) Right-handed PL. (c) Left-handed PL.

In this theoretical research, our aim is to comprehend and justify the mechanism of operation in plasmonic nanogrooves in maintaining the valley polarization of TMD excitons at room temperature. We want to control the plasmon-exciton direction of propagation on the surface (the chiral response of the structure) by manipulating the groove parameters, while maintaining the system in the strong coupling region. More specifically, the **first part** is focused on analyzing the interdependence between the groove parameters and the strong coupling regime.

In the **second part**, we will justify the origin of the polarization resolved far-field PL patterns obtained in the experiment. Mainly, the underlying reason for the difference between the left-handed and right-handed components of the far-field images. Then, by using the results from the first part, we will examine how the strength of the system in maintaining the circular polarization of TMD excitons is influenced by the strong coupling criteria, specifically the depth of the nanogrooves. In order to study this part, we take advantage of a combination of analytic calculations and numerical modeling with FDTD method and Mode Solution.

A list of topics that are addressed during this thesis are:

First part: We perform a detailed study on the effect of groove parameters on the strength of the coupling regime. These parameters include groove depth (d), groove width (w), groove wall angle (θ_g) and groove edge roundness (R).

- The investigation is initiated by the numerical calculation of the angle resolved reflection spectrum of the Ag nanogrooves-WS_2 with Finite-Difference Time-Domain (FDTD) method.
- Having the dispersion data and based on the absorption energy of WS_2, we identify the range of the proper groove parameters for the spectral overlap between nanogrooves and WS_2 to occur.
- By calculating the Rabi splitting for the cases with coupling, the strength of couplings is identified.
- Finally, by measuring the bandwidth of the individual WS_2 and nanogrooves, we will determine whether the coupling meets the criteria for strong coupling or not.

Second part: the purpose of this part is mainly to comprehend and investigate the performance of the structure in real applications.

- We start by analytical calculation for an ideal scenario. To facilitate calculations, we assume an ideal case of a single groove with infinite depth, instead of the real case of nanogrooves with finite depth. We also assume a single circular dipole representing TMD valley polarized excitons. Then we analytically calculate the Poynting vector of such dipole at the vicinity of the groove.
- Next, employing the optimal parameters for strong coupling (from part one), we calculate the structure's capability to distinctly route the valley information of the excitons. In order to do this, we capture polarization resolved far-field images in FDTD and quantify valley polarization in k-space by calculating the degree of polarization.

1.3.2 The significance of the work

This study will contribute to the nascent field of Valleytronics since it provides exact design parameters for an optimal nanostructure to strongly couple to the WS_2 monolayer. The design of groove parameters is the first step to build the hybrid structure. In addition to the initial design, a comprehensive knowledge about the effect of fabrication errors on the performance of the strong coupling is essential. By a proper design and knowing the effect of fabrication defects on the performance of the system, high degree of polarization can be achieved at room temperature.

The thesis will undoubtedly help to clarify the mechanism for achieving robust light-matter interactions in plasmonic nanostructures and TMDs, as a new pathway using spin-valley degree of freedom in 2D materials toward applications in Valleytronics.

1.4 Outline

The chapters of this dissertation are organized as follows. In CHAPTER 1, the context of the study was introduced. Following a brief review of the relevant literature, the research objectives were explained and signified. In CHAPTER 2, the methodology for different parts of the dissertation has been investigated. This includes the procedures applied to design the structure, along with the basic theory of the analytical calculations. This is followed by CHAPTER 3, which is dedicated to the first part of the thesis. There, we will demonstrate a detailed study on the effect of groove parameters on the strength of the coupling regime. It is demonstrated that the groove depth has the most significant effect

on the coupling between plasmons and excitons, compared to other groove parameters. In CHAPTER 4, supporting directionality by an ideal system is proved analytically. In the ideal system the dimensions of the grooves are considered to be infinite. Hence, to study a real case, we focus on the impacts of the groove depth in controlling exciton emission direction, through numerical FDTD simulations.

CHAPTER 2: DESIGN OF NANOSTRUCTURE & CONTROL OF EMISSION DIRECTION

As discussed in the introduction chapter, our main goal in this research is twofold. Firstly, to find an optimal design for the plasmonic nanogroove array to strongly couple to TMD valley polarized excitons at room temperature. Secondly, to examine and justify the performance of the designed structure in exciton emission routing. We start this chapter by discussing our structure design procedure to achieve strong coupling between plasmons and excitons. Following that, our analytical and numerical approach to investigate the effect of the surface geometry on the observed directionality is presented. We close the chapter with a brief conclusion section.

2.1 Structure design procedure

2.1.1 Choice of TMD

In order to make the strong coupling between plasmons and excitons occur, it is imperative to select materials and the structure architecture precisely. Monolayer TMDs with time reversal and broken inversion symmetry have appeared as good candidates for applications involving light-matter interactions. Among the choices of monolayer TMDs, monolayer WS_2 has the advantage of having well-isolated absorption peaks of the "A-exciton" at around 2.02 eV and the "B-exciton" at around 2.4 eV with energy separation of 0.38 eV (Fig. 2.1a-d). A-exciton and B-exciton refer to the lowest and second lowest excitonic state

in the TMDs. It also displays an intense luminescence peak at around 2.016 eV Fig. 2.1e). Thus, it is a good choice for our purpose of light-matter strong coupling in Valleytronics applications.

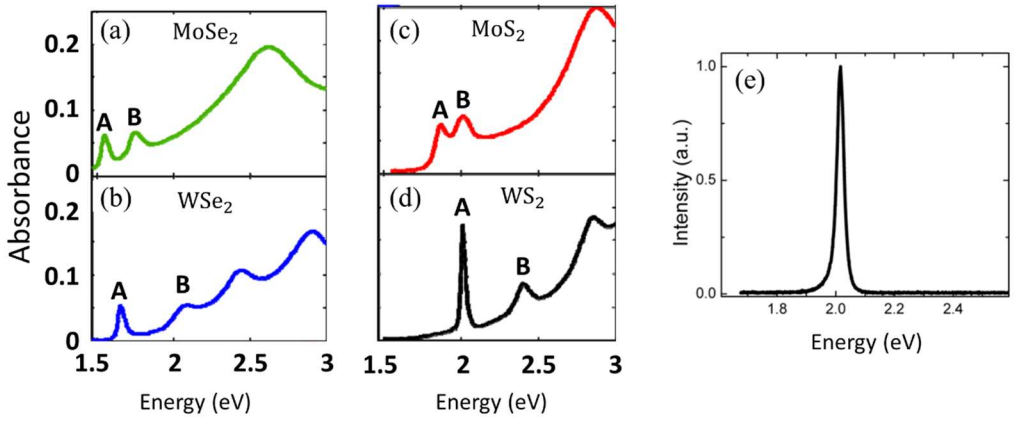

Fig. 2.1 Free stand absorbance of monolayers(a) $MoSe_2$ (b) WSe_2 (c) MoS_2 (d) WS_2. (e) PL spectrum of the monolayer WS_2.

2.1.2 Choice of the plasmonic nanostructure

Here, the role of the plasmonic structure is to sustain and propagate valley polarized exciton emission at room temperature. The radiative decay of the valley-polarized exciton emission is represented by a circular dipole. It has been demonstrated that circular dipoles with opposite polarizations and an out-of-plane component can couple to SPPs propagating in opposite directions on a flat metallic interface [39], [41]. However, TMDs' bright exciton transition dipole moment possess in-plane circular polarization $E_x \pm iE_y$ with no out-of-plane component [43], [56]. Having said this, a flat plasmonic surface cannot exhibit chiral response to these materials with in-plane circularly polarized dipoles, meaning that it cannot differentiate between TMD exciton emissions from **K** and **K′** valleys (Fig. 2.2). To resolve this issue, we introduced nanogrooves on the flat plasmonic

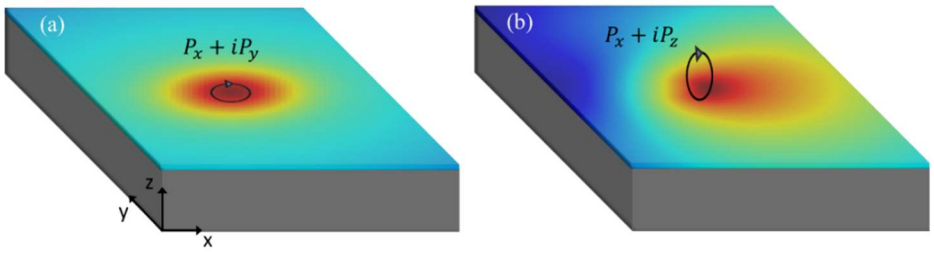

Fig. 2.2 (a) Thea emission of an in plane circular dipole near a metallic surface does not exhibit any directional propagation. (b) For a circular dipole with an out of plane component near the same metallic surface, directionality is observed.

surface. In this way, the in-plane dipoles generated in the TMD are now out of plane (perpendicular) with respect to the groove walls and we can somehow take advantage of the chiral response of the groove walls to the dipoles. It is best to design the plasmonic nanostructure in such a way that its resonance frequency matches with the TMD absorption frequency. Thus, we need to have a precise nanogroove design, which provides efficient coupling to the TMD excitons.

In our collaborator's experiment, the nanogrooves were fabricated with a rectangular shape and nominal geometrical values of Λ=400 nm, w=50 nm and d=70 nm. Fig. 2.3a

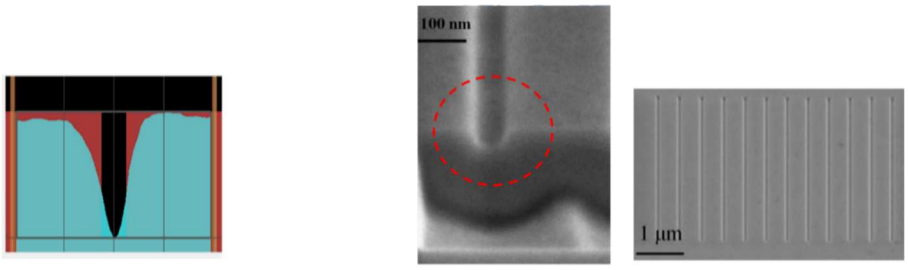

Fig. 2.3 (a) The fabricated groove based on the AFM data. The red structure is with nominal values, and the green one is the final product sketched on top of that. (b) The SEM image of the structure. Both images show deviations from the rectangular shape due to inevitable fabrication errors.

and Fig. 2.3b show the AFM and SEM images of the fabricated structure, respectively. The red area in Fig. 2.3a refers to the ideal groove with nominal parameters. As we see in both figures, due to the limits of fabrication methods, the outcome is more like a trapezoid than a rectangle. Also, the edges of the groove are not sharp. Other than the angled walls and curved edges, the width and depth of the final product may have deviations from the nominal values. Each of these four geometrical parameters along with the **k**-vector of the incident light, which is defined by θ_{inc} and ϕ_{inc} in Fig. 2.4 play a significant role in the condition and strength of the coupling.

2.1.3 Strong coupling between the monolayer TMD and plasmonic nanogrooves

In our model, the TMD over plasmonic nanostructure is illuminated by a linearly polarized incident light. Some part of the incident light is absorbed by the TMD and generates excitons. Another part is reflected and the remining portion transmits and hits the plasmonic structure. The generated TMD dipoles (excitons) originate from the separation of positive and negative charges in the TMD molecular structure by the electric field of incident light $\mathbf{E_{inc}}$. Hence, the generated dipoles are linear, with the direction corresponding to the direction of $\mathbf{E_{inc}}$. It worths to mention that we have the requirement of having an electric field component along the periodicity of the structure for all illumination conditions (Fig. 2.4)[61].

While the behavior of the TMD does not change by changing the angle of incidence, the response of the plasmonic structure is different to incident light with different **k**-vectors. The geometry of the groove is anisotropic along x (direction of periodicity) and y (along the grooves) direction. When the incident light provides a momentum component

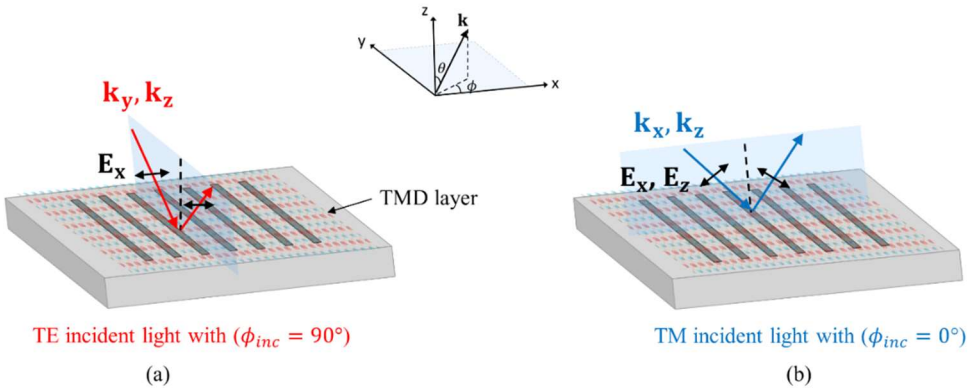

Fig. 2.4 Incident light wavevector and polarization direction for (a) TE incident planewave with $\mathbf{k_{inc}} = k_y\hat{\mathbf{y}} + k_z\hat{\mathbf{z}}$. In this case the polarization would be $\mathbf{E} = E_x\hat{\mathbf{x}}$. (b) TM incident planewave with $\mathbf{k_{inc}} = k_x\hat{\mathbf{x}} + k_z\hat{\mathbf{z}}$, with $\mathbf{E} = E_x\hat{\mathbf{x}} + E_z\hat{\mathbf{z}}$.

along the nanogrooves (the simplest case is when $\phi_{inc} = 90°$), the groove can support channel polaritons or channel modes [59], [60]. For the case with $\phi_{inc} = 0$, a wavevector component along the groove periodicity is provided and the excited modes can propagate along the periodicity of the structure and on the surface. Fig. 2.4 further clarifies the concept. Any incident light with $0° < \phi_{inc} < 90°$ can be decomposed into the two orthogonal directions with $\phi_{inc} = 0°$ and 90°.

As mentioned above, each individual component in this hybrid structure interacts with the incident light. If we consider the incident light as a ground state |0>, the TMD exciton's energy level as |1> and the plasmonic resonance state energy level as |1′>, the interaction between the incident light with the TMD and the plasmonic structure can be shown by |0>→|1> and |0>→|1′>, respectively (Fig. 2.5a). If the energy of the plasmon resonance approaches the TMD excitonic energy level(Fig. 2.5b), then a coherent energy exchange between the plasmon resonance and the excitonic emission occurs |1>↔|1′>.

As a result of such transition two new hybrid states of plasmon-excitons forms, which are different from initial plasmonic and excitonic states [58].

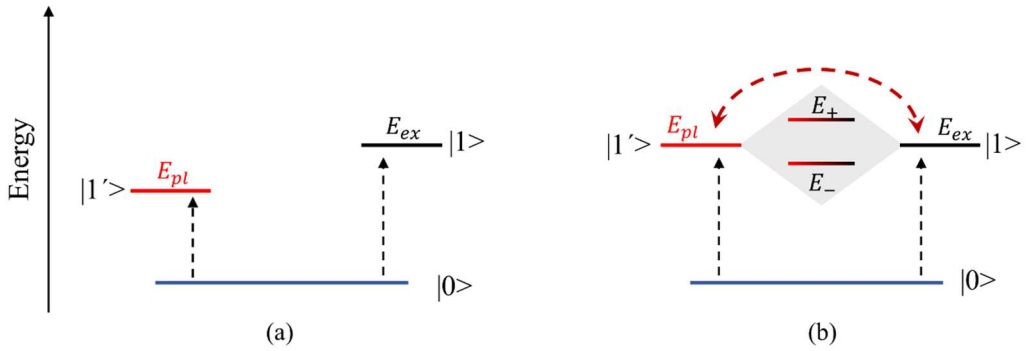

Fig. 2.5 (a) schematic interaction between incident light as a ground state |0>, with individual TMD exciton energy state |1> and the plasmonic state |1´>. (b) The coherent energy transfer between excitonic and plasmonic states as their energy level approaches together.

These two newly formed hybrid states can be described by the two-coupled-oscillator model [34]–[36], [44]–[48], [58] which satisfies the eigenvalue equation as:

$$\begin{pmatrix} E_{pl} - \frac{i\gamma_{pl}}{2} & g \\ g & E_{ex} - \frac{i\gamma_{ex}}{2} \end{pmatrix} \begin{pmatrix} \alpha \\ \beta \end{pmatrix} = E_{\pm} \begin{pmatrix} \alpha \\ \beta \end{pmatrix} \tag{2.1}$$

Where E_{pl} and E_{ex} refer to the energies of the uncoupled plasmon and exciton, respectively. The corresponding dissipation rates are given by γ_{pl} and γ_{ex} and characterized by the linewidth of the corresponding absorption peaks. E_+ and E_- are the eigen energies of the coupled system corresponding to upper energy branch (UEB) and lower energy branch (LEB), respectively. g is the coupling strength and α and β make the

eigen coefficients satisfying $|\alpha|^2 + |\beta|^2 = 1$. By solving the above eigen value equation, the energy of the hybrid states will be given by:

$$E_{\pm} = \frac{1}{2}\left[E_{pl} + E_{ex} \pm \sqrt{4g^2 + \left(\delta - \frac{i}{2}(\gamma_{pl} - \gamma_{ex})\right)^2} \right], \tag{2.2}$$

in which $\delta = E_{pl} - E_{ex}$ is the detuning energy between each individual state, here, plasmon and TMD A-exciton energy. The Rabi splitting of the hybrid structure is defined as:

$$\hbar\Omega_{\mathrm{R}} = E_{+} - E_{-} \quad at \quad \delta = 0 \tag{2.3}$$

So, we will have:

$$\hbar\Omega_{\mathrm{R}} = \sqrt{4g^2 - \frac{(\gamma_{pl} - \gamma_{ex})^2}{4}}\ . \tag{2.4}$$

There have been several criteria reported to distinguish the “strong” coupling regime [15], [73]. Arguably the simplest criterion for strong coupling is the splitting of the peak in the absorption spectra. So, the occurrence of an intensity minimum between two peaks would be considered as a strong coupling regime. However, this criterion alone can be misleading as it is possible to misinterpret original split spectra as being the splitting caused by strong coupling. This issue has led to the categorization of an “intermediate coupling regime” as identified in experiments involving strong coupling scattering [73].

Among the criteria considered for strong coupling [74], the most intuitive one for strong coupling criteria is defined as [32], [34], [48], [73], [75], [76]:

$$\hbar\Omega_R > \frac{\gamma_{pl} + \gamma_{ex}}{2} \quad , \tag{2.5}$$

in which $\frac{\gamma_{pl}+\gamma_{ex}}{2}$ represents the average linewidth of uncoupled excitonic and plasmonic states.

In this work, in order to define the strong coupling criteria and rule out intermediate and weak couplings, we follow the steps below. A structure which fulfills the first condition is in the intermediate coupling regime, and a structure passing both criteria will be considered as working in the strong coupling regime.

1. First, structures without mode splitting in their absorption spectra are ruled out. Here, mode splitting refers to the occurrence of a minimum between two maxima in the absorption spectrum. This criteria accounts for the spectral overlap and satisfies the intermediate coupling condition [73]. The upper panel in Fig. 2.6 corresponds to a situation passing this criteria. Fig. 2.6a) shows the dispersion pattern and an obvious splitting between the plasmonic and the excitonic states. The maximum points of the dispersion map are shown in fig Fig. 2.6b by small circles. The angle corresponding to the minimum amount of splitting (Rabi splitting $\hbar\Omega_{\mathrm{R}}$) between two states is the coupling angle and is shown as θ_C in Fig. 2.6c. Finally, fig Fig. 2.6d shows the absorption spectrum at the $\theta_{inc} = \theta_C$,which clearly presents the dip between two maxima.

   We disregard the cases with the minimum splitting at the limits of the incident angle (at normal or large incident angles). As we see in the lower panel of Fig. 2.6, specifically Fig. 2.6e and Fig. 2.6f, although the exciton and plasmon lines are

disturbed as the result of spectral proximity, and a dip is sandwiched between two maxima, there is no local minimum in the Fig. 2.6g depicting the energy difference between upper and lower energy states. This criteria guarantees that the observed dip in the spectrum is the result of coupling and anti-crossing between the two states and disregards any originally split spectra beside each other.

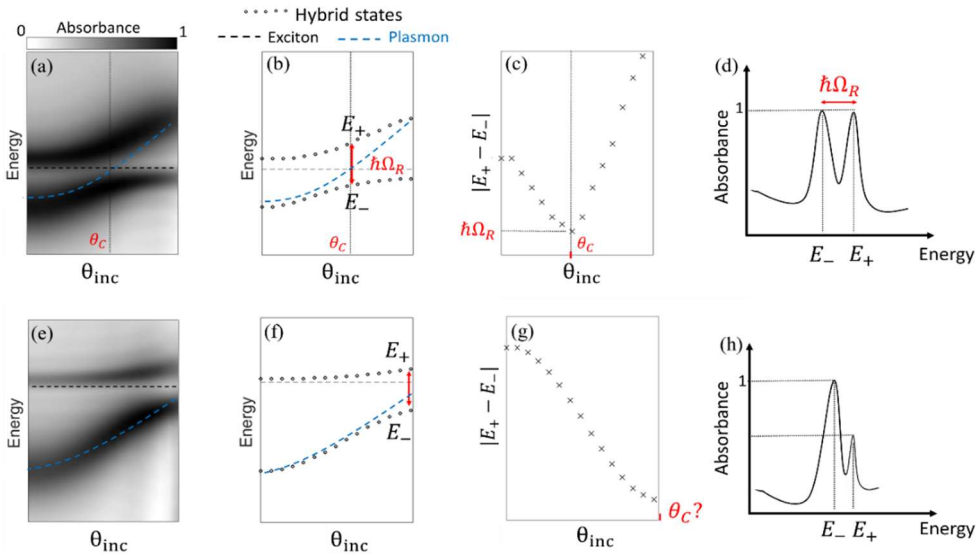

Fig. 2.6 **Upper panel:** (a)A clear demonstration of coupling between plasmonic and excitonic states in a dispersion map. (b)Extracted maxima from the dispersion map. (c)The energy difference between two states as a function of θ_{inc}. A local minimum in this plot is an indicator of strong coupling and its value shows Rabi splitting. (d) Absorption spectrum at θ_{inc}= θ_C showing the sandwiched dip between two maxima. **Lower panel:**(e),(f) Dispersion map and its maxima for a structure not fulfilling strong coupling criteria. (g) No local minimum in the energy difference vs. θ_{inc}. (h) Absorption spectrum showing a dip sandwiched between two maxima, although the structure is not considered in strong coupling regime.

2. After passing the above prerequisite, eq. (2.5) defines whether the strong coupling criteria is fulfilled or not. Based on this condition, if the peak splitting is larger than the average of the uncoupled peak linewidths, the system is in a strong coupling regime.

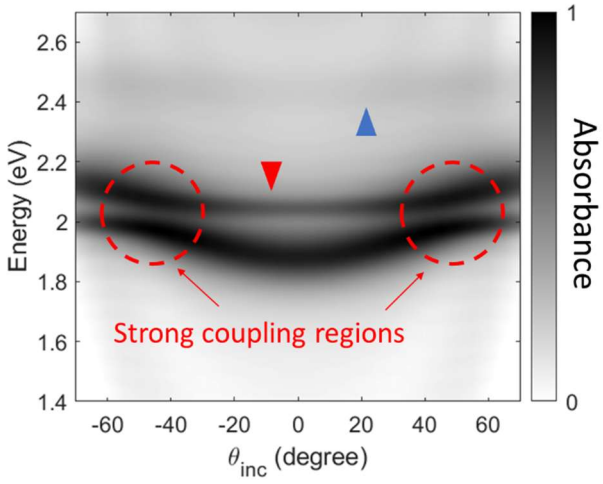

Fig. 2.7 A sample of angle resolved reflection spectra from the hybrid structure of TMD-nanogrooves with constant azimuthal angle $\phi_{inc} = 90°$. The red circles show the anti-crossings at strong coupling regions. The red and blue triangles point the A-exciton and B-exciton of WS_2, respectively.

Here, the effects of nanogrooves' parameters on the strength of plasmon-exciton coupling are analyzed in FDTD. Under a broadband plane wave source excitation, by varying the angle of incidence (θ_{inc}) and (at constant azimuthal angles of ϕ_{inc}= 90° and ϕ_{inc}= 0), reflection spectra of the hybrid WS_2-nanogroove structure are recorded. The regions of spectral overlap between the individual TMD and plasmonic nanogroove dispersion profiles are an indicator of the coupling and formation of the hybrid plasmon-exciton states. Fig. 2.7 represents an example of coupling region for the hybrid structure of WS_2-nanogroove and its dependence on varying θ_{inc} for $\phi_{inc} = 90°$. In the given angle-resolved reflection spectra, the nearly horizontal dark zones pointed by a small red and blue triangle represent the absorption line of WS_2 "A-exciton" and "B-exciton", which are almost constant at 2.02 eV and 2.4 eV for any angle of incidence. The curved dark zone is attributed to the dispersion of the nanogroove structure. As we see at the regions of

coupling, marked by red dash circles, the two profiles do not fully cross due to the anti-crossing phenomenon. As mentioned earlier, the anti-crossing behavior is a typical characteristic of enhanced light-matter interaction following the strong coupling [77], [78].

2.2 The effect of the surface geometry on directionality

As stated earlier, in monolayer TMDs the valley pseudospin response is different to incident lights with different circular polarizations. By incorporating metallic structures, we can preserve the valley distinguishability feature at room temperature. In the second part of this dissertation, our goal is to demonstrate the effect of the surface geometry on directionality theoretically and show that through engineering the metallic structure, we can control the angle of propagation on the surface.

Due to the limitations of analytical calculations which will be explained in the following section, we investigate an ideal case analytically. Then we transition to the numerical calculations using FDTD to thoroughly examine how surface geometry influences the observed exciton routing.

2.1.1 Analytical calculations

The radiative decay of the valley-polarized exciton emission is represented by a circular dipole. Our analytic calculations are based on phase matching condition between a circularly polarized dipole and the nanogroove plasmonic mode. To simplify the model, we replace the valley polarized TMD excitons with two opposite circularly polarized dipoles located close to the metallic structure. In mathematical study, an ideal case of

single groove is considered, instead of the case of periodic structure. By analyzing the "Poynting vector" of the coupled radiation of the dipole and the plasmonic mode, the possible control over directionality on the surface is investigated.

First, we consider a general dipole with dipole moment $\mathbf{P}$ located at $\mathbf{r_0} = (x_0, y_0, z_0)$ in an isotropic and homogeneous medium characterized by μ and ε. To find the vector potential of the dipole $\mathbf{A}(\mathbf{r})$ at position $\mathbf{r}$ in the medium, we need to solve the inhomogeneous Helmholtz equation

$$[\nabla^2 + k^2]\mathbf{A}(\mathbf{r}) = -\mu\mu_0\mathbf{j}(\mathbf{r}) , \tag{2.6}$$

where k is the wavenumber and $\mathbf{j}(\mathbf{r})$ represents the dipole current density given by:

$$\mathbf{j}(\mathbf{r}) = i\mu\mu_0\omega\ \mathbf{P}\ \delta(\mathbf{r} - \mathbf{r_0}) , \tag{2.7}$$

Here, $\omega = ck$ is the angular frequency of the field. Using the Green's function method, the spatial representation of the vector potential of the dipole will be obtained as:

$$\mathbf{A}(\mathbf{r}) = \mathbf{P}\frac{k^2}{i\omega\varepsilon\varepsilon_0}\frac{e^{\pm ik|\mathbf{r}-\mathbf{r_0}|}}{4\pi\ |\mathbf{r} - \mathbf{r_0}|} \quad , \tag{2.8}$$

which can be written in cartesian coordinate as:

$$\mathbf{A}(\mathrm{x},\mathrm{y},\mathrm{z}) = \mathbf{P}\frac{k^2}{i\omega\varepsilon\varepsilon_0}\frac{e^{\pm ik\sqrt{(x-x_0)^2+(y-y_0)^2+(z-z_0)^2}}}{4\pi\sqrt{(x-x_0)^2+(y-y_0)^2+(z-z_0)^2}} . \tag{2.9}$$

According to the Weyl identity, the vector potential at any arbitrary image plane (z=const.) is expressed as [78]:

$$\mathbf{A}(\mathrm{x},\mathrm{y},\mathrm{z}) = \mathbf{P}\frac{k^2}{8\pi^2\omega\varepsilon\varepsilon_0}\iint_{-\infty}^{\infty}\frac{e^{\pm i[k_x(x-x_0)+k_y(y-y_0)+k_z|z-z_0|]}}{k_z}dk_x dk_y \ , \tag{2.10}$$

where $k_z = \sqrt{k^2 - k_x^2 - k_y^2}$ with $Im\{k_z\} \geq 0$. Such assumptions of Weyl identity apply the plasmonic feature of the surface. The integrand in eq. (2.10) represents the expansion of the field into plane and evanescent waves (the angular spectrum representation).

Maxwell's equations give the electric field $\mathbf{E}(\mathrm{x},\mathrm{y},\mathrm{z})$ and magnetic field $\mathbf{H}(\mathrm{x},\mathrm{y},\mathrm{z})$, as

$$\begin{aligned}\mathbf{E}(\mathrm{x},\mathrm{y},\mathrm{z}) &= i\omega\left[1+\frac{1}{k^2}\nabla\nabla.\right]\mathbf{A}(\mathrm{x},\mathrm{y},\mathrm{z}) \ , \\ \mathbf{H}(\mathrm{x},\mathrm{y},\mathrm{z}) &= (\mu\mu_0)^{-1}\nabla\times\mathbf{A}(\mathrm{x},\mathrm{y},\mathrm{z}) \ .\end{aligned} \tag{2.11}$$

By representing the electric and magnetic fields as their inverse 2-D Fourier Transforms $\hat{\mathbf{E}}$ and $\hat{\mathbf{H}}$

$$\begin{aligned}\mathbf{E}(\mathrm{x},\mathrm{y},\mathrm{z}) &= \iint_{-\infty}^{\infty}\hat{\mathbf{E}}(\mathrm{k_x},\mathrm{k_y};\mathrm{z})e^{-i[k_x x+k_y y]}dk_x dk_y \ , \\ \mathbf{H}(\mathrm{x},\mathrm{y},\mathrm{z}) &= \iint_{-\infty}^{\infty}\hat{\mathbf{H}}(\mathrm{k_x},\mathrm{k_y};\mathrm{z})e^{-i[k_x x+k_y y]}dk_x dk_y \ ,\end{aligned} \tag{2.12}$$

the k-space Poynting vector of a dipole emission in the x-y plane will be given by:

$$\hat{\mathbf{S}}(\mathrm{k_x},\mathrm{k_y};\mathrm{z}) = \frac{1}{2}Re\{\hat{\mathbf{E}}(\mathrm{k_x},\mathrm{k_y};\mathrm{z})\times\hat{\mathbf{H}}^*(\mathrm{k_x},\mathrm{k_y};\mathrm{z})\} \ . \tag{2.13}$$

The above derivations are for a general form of a 3D dipole with dipole moment **P**. In our calculations, we assume a circularly polarized dipole in the x-y plane with the dipole moment $[p_x, p_y] = p_0[i \pm 1]$, to specifically represent in plane valley polarized excitons.

2.1.2 Numerical study of valley-polarized exciton routing

The FDTD method is employed to numerically study the polarization-dependent propagation due to the circularly polarized emission from different WS_2 valleys. To simplify the scenario, the radiative decay of the **unpolarized** TMD exciton is represented by a single linearly polarized dipole. This substitution provides all the possible angles of illumination (covering all θ_{inc} and ϕ_{inc}). The dipole is placed on top of the periodic structure at the location of the monolayer TMD. The propagation of the coupled plasmon-excitons is investigated by analyzing the k-space PL images due to their capability in simplifying our interpretation. A planar field profile monitor is placed on the horizontal surface and the k-space PL images are achieved by the projection of this surface monitor data to the surface of a hemisphere in the Far-field region. The final result is an image of the field intensity on the hemisphere, as viewed from above (Fig. 2.8a).

The coupling between exciton emission near-field with the SPP forms plasmon-exciton pairs that can propagate along the nanogrooves (the guided SPP in the y direction) and perpendicular to the nanogrooves (the surface confined SPP in the x direction). Fig. 2.8b shows an example of a far-field image detected at the wavelength corresponding to the strong coupling region ($E \sim 2.02$ eV, $\lambda \sim 616$ nm). The azimuthal angle in such polar image ranges from 0 to 2π covering the whole region of the in-plane monitor. The

azimuthal angles with high intensity of far-field show the propagation direction on the surface.

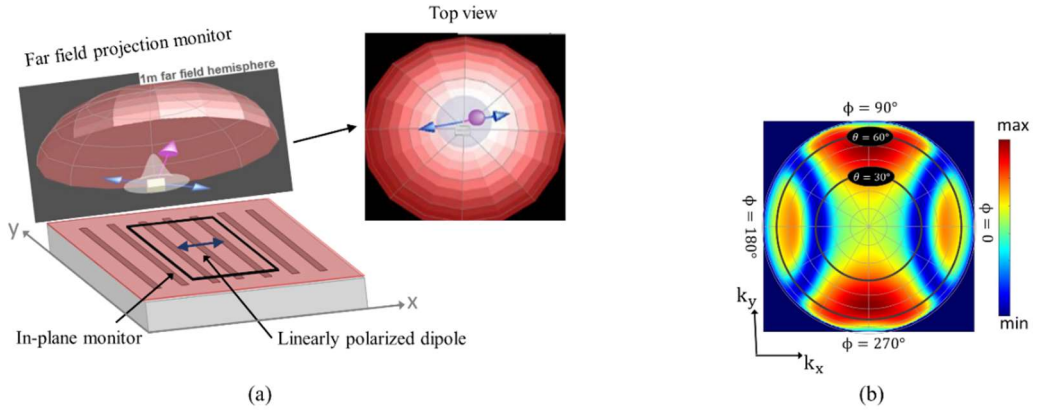

Fig. 2.8 The simulation setup and projection mechanism for obtaining far-field images. (b) An example of a far-field intensity image. Angle ϕ represent the azimuthal angle which corresponds to the angle of propagation in the surface.

After capturing the k-space PL distribution, we need to extract the polarization dependent PL coupling. As mentioned earlier, PL emission from different valleys of WS_2 carries opposite circular polarizations. In the experiments, this separation can be accomplished by using a combination of polarizers and waveplates in the detection path. In our simulated k-space images, we separate different circular polarizations by separating the electric field components through $E_x \pm iE_y$ with the negative sign for right-handed (σ^-) emission and the positive sign for left-handed (σ^+) emission. As a result, a separated emissions of $I(\sigma^+)$ and $I(\sigma^-)$ polaritons in momentum space can be observed. This separation qualitatively indicates that the polaritons at the K and K′ valleys are routed in opposite directions. However, to have a hybrid structure with the best performance, we need to quantify these polarization separations. This can be done by defining a parameter

"degree of circular polarization (DCP)" by dividing the difference between the two circularly polarized PL components by sum of them:

$$DCP(k_x, k_y) = \frac{I(\sigma^+) - I(\sigma^-)}{I(\sigma^+) + I(\sigma^-)} \ . \tag{2.14}$$

The DCP at any point in the k-space can range between 1 to -1 corresponding to maximum possible left/right-handed polarization content. This number can quantify the amount of circular polarization at each point in the k-space. However, to efficiently find the location in k-space with maximum of both field distribution and degree of circular polarization, we need to calculate the coupling strength in that specific location. The position dependent coupling coefficient is defined as:

$$\kappa(k_x, k_y) = \frac{I(\sigma^+) + I(\sigma^-)}{max\ [I(\sigma^+) + I(\sigma^-)]} \tag{2.15}$$

Combining these two above parameters gives the chiral coupling strength or $\kappa_{chiral}(k_x, k_y)$ at each points in the k-space.

$$\kappa_{chiral}(k_x, k_y) = \kappa(k_x, k_y).DCP(k_x, k_y). \tag{2.16}$$

This parameter can range from -1 to 1 depending on the structure. For a specific structure, the maximum positive (negative) value shows the location in k-space with the best possible degree of coupling strength for left- (right-)handed circular polarization.

2.3 Summary and conclusion

In summary, this chapter outlined the research methodology for both parts of this dissertation. We started with the procedures applied to design the monolayer TMD-nanogrooves hybrid structure. This includes the selection of TMD material, choice of groove parameters and the criteria necessary for achieving a strong coupling regime. In the second section, we presented the analytical approach and FDTD mechanism that were employed to explore and quantify the capability of the designed structure to guide valley polarized TMD exciton emissions into different directions.

CHAPTER 3: STRONGLY COUPLED PLASMONS AND EXCITONS

Given the constant and non-dispersive absorption of TMDs, achieving strong coupling between monolayer TMD and plasmonic nanogrooves requires a precise nanogroove design. This design should ensure not only the resonance frequency of the TMD, and nanostructures coincide, but also the strong coupling regime is achieved. The resonance frequency of the metallic nanogrooves is highly sensitive to the geometrical features of the groove (groove period, width, and depth). Other than these nominal parameters, errors in the fabrication process are inevitable parts of the experiments, while they impact the conditions of the strong coupling. That being said, a complete knowledge about the relation between each geometric feature and the resultant coupling in the hybrid structure would be desired.

We start this chapter by presenting our numerical findings regarding the effects of the nanogroove parameters on the occurrence of strong coupling in the hybrid structure of monolayer WS_2-nanogroove. The discussion and interpretation of the data will follow the results section.

3.1 Geometry and design of nanogrooves: simulation structure

Our first purpose is to theoretically investigate how varying each individual geometrical parameter of the nanogrooves can change the strong coupling condition where the anti-

crossings (spectral overlap) between WS_2 and nanogrooves absorption occur. We study this in FDTD by evaluating the status of the coupling as a function of an individual groove parameter (depth and width) while others are fixed.

As mentioned in the methodology chapter, we design an infinite periodic Ag grooves with rectangular cross section. The refractive index of the Ag is chosen from Lumerical data base "Ag(Silver) – Palik (0-2 um)". In order to match with an actual structure which is commonly used in experiments, a 4 nm uniform coating of Al_2O_3 with Palik refractive index covers Ag to protect it from oxidation. A single layer of WS_2 with 0.618 nm thickness and adopted experimental dielectric function from [79] is placed on top. See Fig. 3.1 for a clear picture of the structure. For brevity, whenever we call the structure "WS_2-nanogrooves" we mean the hybrid structure of "monolayer WS_2 and coated Ag nanogrooves".

The infinite periodicity of the grooves is applied by employing periodic boundary condition (PBC) in the x direction. The minimum mesh size around the groove region is chosen 0.5 nm in x and z directions to precisely account for variations in groove width

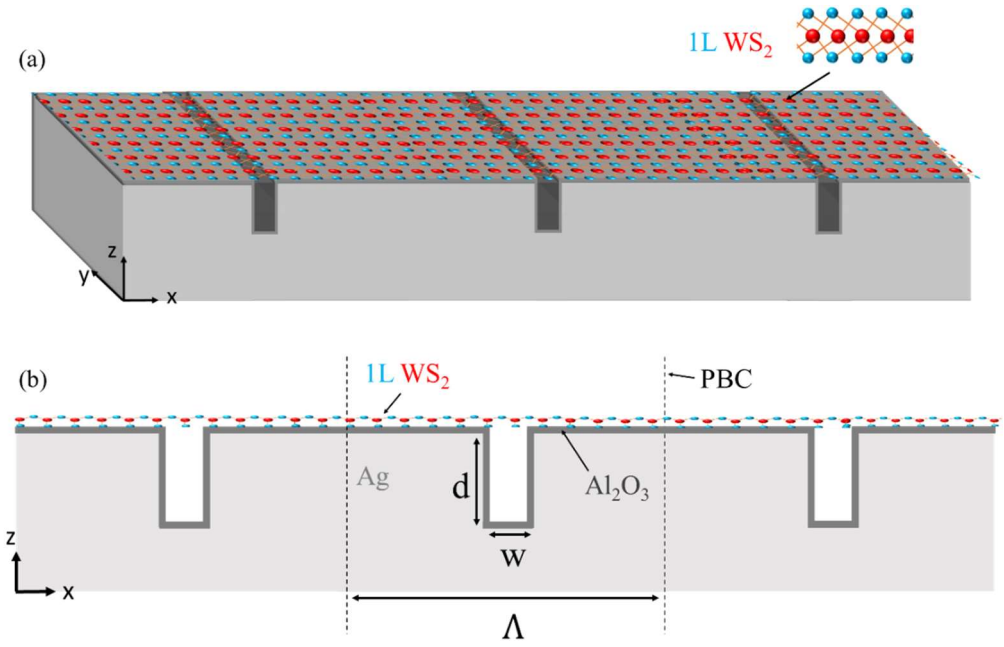

Fig. 3.1 (a) The simulation setup consisting of an infinite array of Ag nanogrooves, coated with 4 nm Al_2O_3 and a layer of WS_2 on top. (b) Side view representation of the structure.

and depth. To resolve the extremely thin region of the monolayer WS_2, a mesh size of 0.1 nm is employed along the vertical direction (z) of the layer.

Under a broadband plane wave excitation, by scanning the angle of incidence (θ_{inc}) and at constant azimuthal angles of ϕ_{inc}= 90° and ϕ_{inc}= 0 the reflection and -following that- absorption spectra are recorded by varying one of the groove parameters, while others are fixed. We have done the study of four -isolated- errors, errors in 1. depth, 2. width, 3. straightness of groove walls and 4. roundness of the groove edges. In all cases the coupling is sensitive to deviations from nominal values. TM and TE polarizations for the incident lights are chosen such that the electric field at the illuminated point always has a component along the periodicity of the structure. To clarify please refer to Fig. 2.4.

Introducing the Al_2O_3 coating to the nanogrooves causes a redshift due to the dielectric screening which is caused by higher refractive index of the coating compared to that of air [80]. The amount of the redshift depends on the thickness of the coating chosen. As mentioned above, we keep the coating as a uniform layer of 4 nm for all the study. Fig. 3.2a shows an example of the angle resolved absorption spectra of coated Ag nanogrooves without the WS_2 with p=400, d=50 and w=50 nm (constant ϕ_{inc}= 90°). Upon introducing the monolayer WS_2 in Fig. 3.2b , not only the coupling between two states occurs, but also

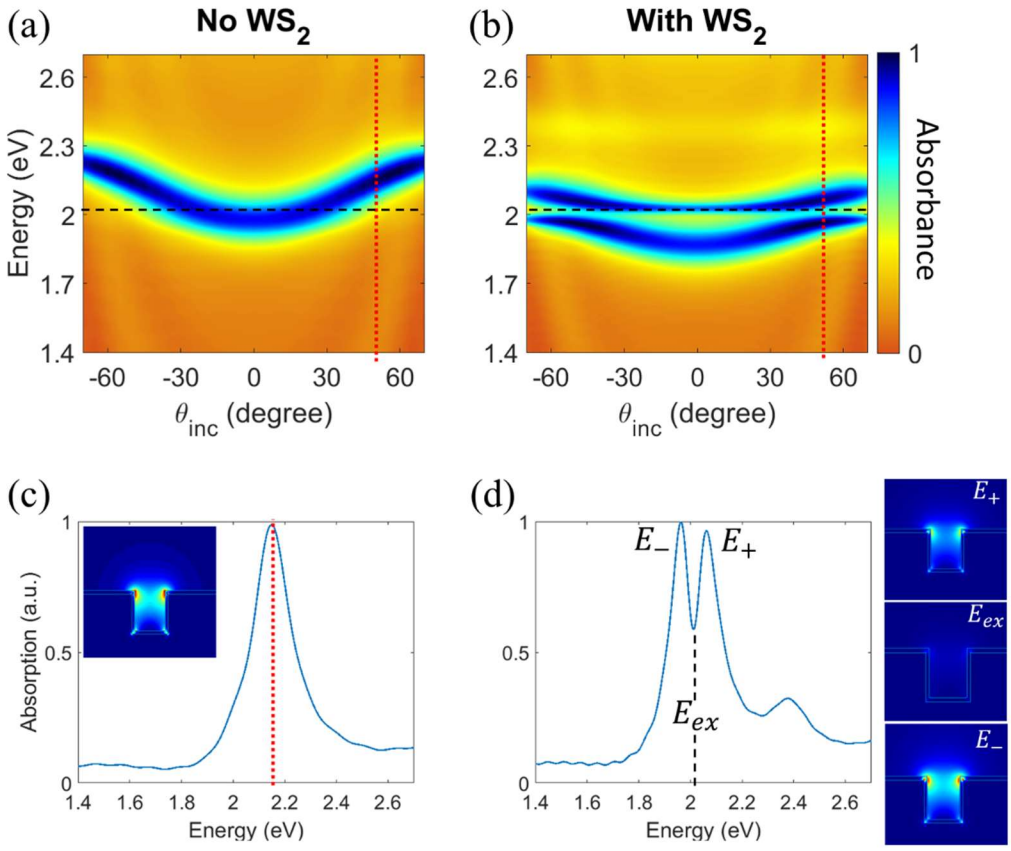

Fig. 3.2 Angle resolved absorption spectra of (a) Al_2O_3 coated Ag nanogrooves. (b) hybrid structure of coated nanogrooves-WS_2. The redshift and anti-crossing after adding WS_2 to the structure is observed. The dashline is WS_2 absorption line. (c) The absorption spectrum at fixed angle of incidence = 50°, along the red dot line in fig (a). The inset shows the electric field intensity at peak. (d)) The absorption spectrum at the coupling angle (θ_{inc} = 50°) along the red dot line in fig (b). The insets shows the electric field intensity at labled energies by E_+, E_{ex} and E_- from top to bottom, respectively.

the absorption profile of the nanogrooves is red shifted due to the much larger refractive index of the WS_2 [44].

3.2 Results and discussion

3.2.1 The effect of depth on the coupling (ϕ_{inc}= 90°)

After characterizing the structure and the effect of each component in the resonance spectrum, we move on to study the effect of individual groove parameters on the coupling. To this aim, the angle resolved absorption spectra of WS_2-nanogrooves by varying individual groove parameters are recorded. Fig. 3.3 monitors the absorption spectra and the coupling for sharp-edged rectangular grooves with Λ=400 nm, w=50 nm and varying groove depths with ϕ_{inc} fixed at 90° . In Fig. 3.3a the WS_2 "A-exciton" line at around 2.02 eV does not cross the dispersion curve of the nanogrooves implying that no coupling with "A-exciton" exists there. The bright green line around 2.4 eV is an indicator of the spectral proximity of the nanogroove resonance with WS_2 "B-exciton", which is out of the scope of our topic. In Fig. 3.3b and Fig. 3.3c, the nanogroove dispersion shifts to lower energies (redshifts) and couples to WS_2 by passing its absorption line. In Fig. 3.3d the spectral overlap is at the very edge of the large incident angles. We do not consider the cases with the spectral overlap at the limit of large (or small) incident angles. This guarantees that the observed dip in the spectrum is the result of coupling and anti-crossing between the two states, not just two individual absorption lines close together (refer to Fig. 2.6).

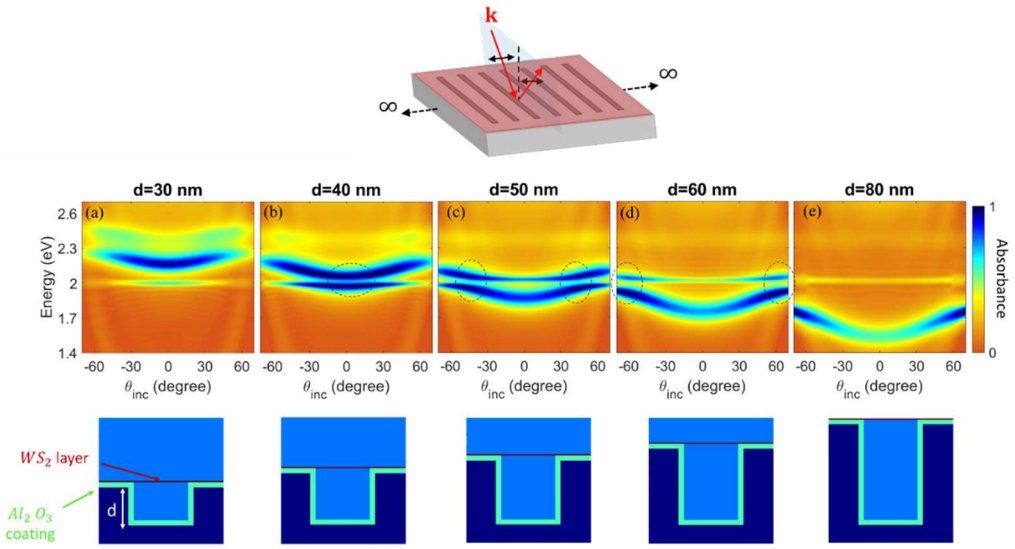

Fig. 3.3 FDTD simulated angle resolved absorption spectra of the hybrid structure with Λ=400 nm, w=50 nm, and varying depths by scanning θ_{inc} and constant ϕ_{inc}=90°. The grooves are rectangular with sharp edges. The dashed lines show the range of θ_{inc} at which the coupling occurs.

As is evident, the incident angle corresponding to the coupling regions increases for grooves with larger depths, meaning that by increasing the depth, to still get the coupling, we need to increase the angle of incidence for up to an upper limit of depth. Passing that limit, as it is seen in Fig. 3.3e, no coupling is achievable for d=80 nm by changing the angle of incidence.

As mentioned in the methodology chapter, not every anti-crossing indicates a strong coupling. In order to quantify the strength of coupling between two states, we measure the amount of splitting between two absorption lines at "anti-crossing" locations, i.e., the Rabi splitting. If the criterion imposed by Eq. (2.5) and its prerequisite are met, then we claim that the hybrid plasmon-exciton state is in the strong coupling regime.

In order to study the relation between the strength of coupling and depth variations with ϕ_{inc}= 90°, first, we rule out the cases without obvious mode splitting, which refer to the Fig. 3.3a and Fig. 3.3e with d=30 and 80 nm. Regarding the structure with d = 60 nm, the absorption maxima in the dispersion is depicted in Fig. 3.4a. The absence of a local minimum in the plot of ΔE vs. θ_{inc} (Fig. 3.4b) places this structure out of the strong coupling regime based on our criteria. This structure may show a local minimum if we scan angles further than 70°, but we just avoid such couplings at large incident angles.

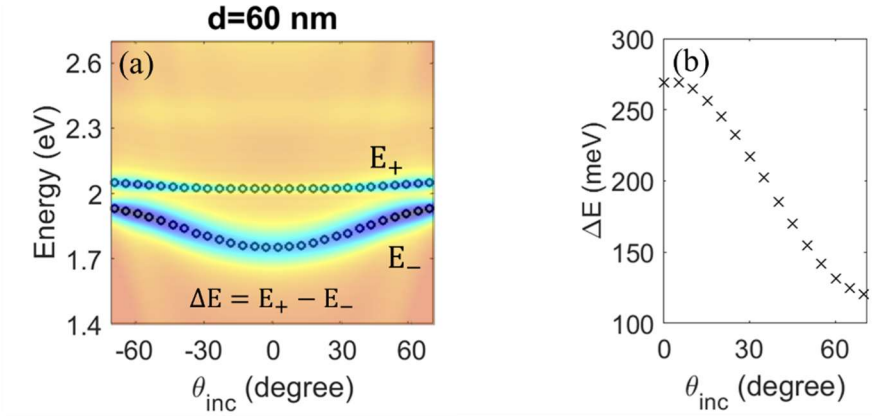

Fig. 3.4 (a)Absorption maxima in the dispersion plot of the structure with d=60 nm. (b) Energy difference between UEB and LEB as the function of incident angle.

For the remaining options, which are nanogrooves with d=40 and d=50 nm and two more interim cases with d=45 and d=55 nm, in Fig. 3.5 the Rabi splitting from the simulated absorption profiles are calculated. Each box corresponds to a specific groove depth. In each group, the top-left panel illustrates the absorption maxima in the angle-resolved dispersion profiles along with the amount of Rabi splitting. The bottom-left panel depicts the energy difference between the upper and lower states (ΔE) as a function of

incident angle. The range of angles corresponding to the minimum value of ΔE are the incident angles in which the coupling in the structure is possible and we call them θ_C . As an example, for the groove with d=40 nm, The minimum amount of splitting (Rabi splitting) between the two graphs in the dispersion map is $\hbar\Omega_R$=86.11 meV and this minimum splitting occurs at $\theta_{inc} = \theta_C \sim 1° - 10°$. This range of angles are marked with red arrow in the dispersion figure at the top left and circled with dashed red line in the ΔE graph at bottom left of the box (a) in Fig. 3.5.

The right panel in each figure group depicts the absorption spectra for different incident angles (θ_{inc} ranging from 0 to 70° with step of 5°). The absorption spectra at the angles corresponding to θ_C are shown in red; the spectra corresponding to the $\theta_{inc} = 1° - 10°$ for the case with d= 40 nm in box (a). While the angle resolved dispersion profiles clearly show the anti-crossing between the two states, the absorption profile and the ΔE graph can define the Rabi splitting and the angle at which the splitting has occurred.

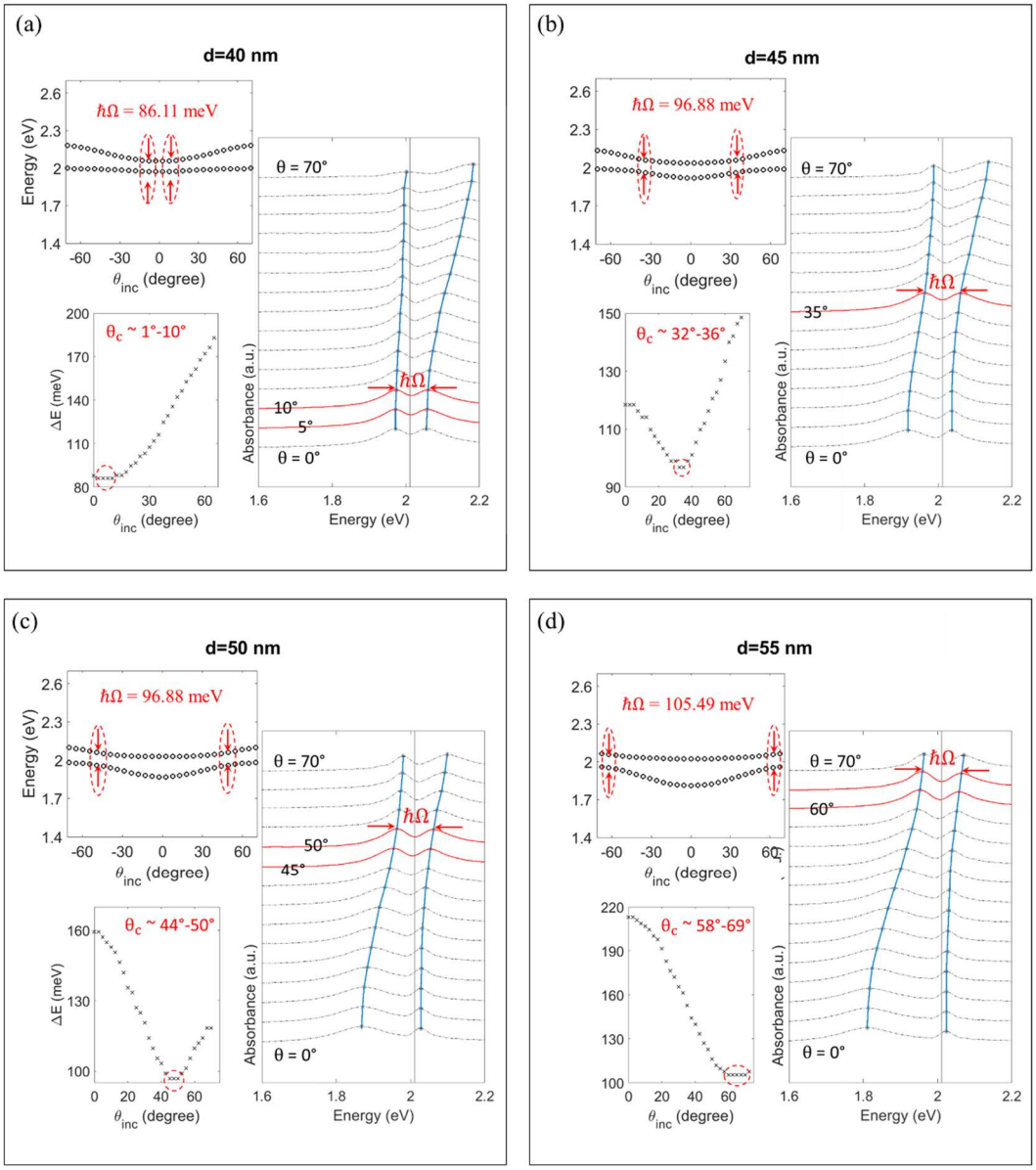

Fig. 3.5 Each figure group contains: **Top left:** the absorption maxima in the angle-resolved dispersion profiles. **Bottom left:** the energy difference between the upper and lower states (ΔE) as a function of incident angle. **Right:** absorption spectra for different θ_{inc} with the step of 5° for a hybrid structure with rectangular nanogrooves and Λ=400, w=50, (a) d=40 nm. (b) d=45 nm. (c) d=50 nm. (d) d=55 nm. ϕ_{inc}= 90° is constant for all cases.

Now using Eq. (2.5) we define whether these couplings fulfill strong coupling criteria or not. The mentioned equation looks for the structures with Rabi splitting larger than the average dissipation rate of the uncoupled plasmon and exciton states. The average dissipation rate is defined by the linewidth of the individual absorption peaks. The linewidth of WS_2 is obtained by fitting the complex dielectric function of WS_2 monolayer to the multi-Lorentzian model and is equal to γ_{ex} = 30 meV [79] . For the plasmonic nanogrooves linewidth, we record the absorption profile of the plasmonic nanogrooves without the presence of the WS_2 layer for each case at the angle that the coupling occurs. As an example, Fig. 3.6 shows the absorption line of the Ag nanogroove structure with d=55 nm under broadband planewave excitation at θ_{inc} = 60°. The groove parameters for this figure correspond to the structure in Fig. 3.3d and the 60° is the coupling angle. For the cases with more than one coupling angle, the average of the linewidths is considered.

Knowing the dissipation rates and the value of Rabi splitting, using Eq. (2.5) we define Figure of merit (FOM) for each case.

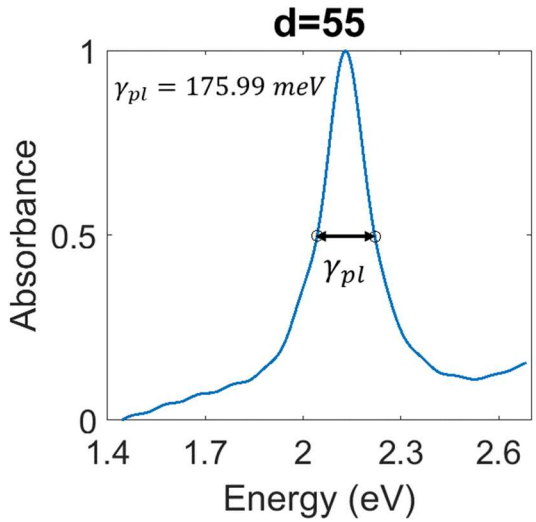

Fig. 3.6 The absorption line of the individual nanogrooves with d=55 nm at θ_{inc} = 60° (coupling angle).

$$FOM = \frac{\hbar\Omega_R}{\gamma_{av}}, \tag{3.1}$$

where, $\gamma_{av} = \frac{\gamma_{pl}+\gamma_{ex}}{2}$ is the average dissipation rate in the WS_2-nanogrooves structure. The cases with FOM larger than one, satisfy strong coupling criteria rigorously. Table 3.1 summarizes the status of the coupling (for $\phi_{inc} = 90°$), by varying groove depth. As we move toward deeper grooves, the amount of splitting between two states increases, however, only the structure with d=55 nm satisfies the strong coupling criteria. For d=40, 45, and 50 nm, although we observe coupling, they are not classified within the strong regime. Structures with d=30, 60, and 80 do not show coupling.

Table 3.1 Summary of the **groove depth** study when the incident angle has k-component along the grooves ($\phi_{inc} = 90°$). Rabi splitting ($\hbar\Omega_R$), the average dissipation rate (γ_{av}) and FOM are calculated for each case.

Depth Study - $\phi_{inc} = 90°$						
Λ (nm)	d (nm)	w (nm)	shape	$\hbar\Omega_R(meV)$	$\gamma_{av}(meV)$	FOM
400	30	50	rect	No splitting observed.		
	40			86.11	109	0.79
	45			96.88	112.5	0.86
	50			96.88	108	0.89
	✓55			105.49	102.99	1.02
	60			Splitting observed. No local minima in ΔE graph.		
	80			No splitting observed.		

3.2.2 The effect of width on the coupling (ϕ_{inc}= 90°)

Now, after identifying the effect of the depth variations on the coupling condition in the WS_2-nanogroove structure, we move to the investigation of the groove width. Fig. 3.7 depicts the dispersion graph and coupling region occurrence for sharp-edged rectangular grooves with depth of 60 nm and varying widths. Upon increasing the groove width from 50 nm to 90 nm, although we observe a blueshift in the nanogroove dispersion along with decrease in the incident angle required for coupling; the change is not as significant as the result for varying the groove depth. It means that the dispersion of the structure is less sensitive to the fabrication errors due to the width compared to the depth of the nanogrooves. Also, as the groove width increases, the anti-crossing region becomes less resolvable due to the broadening of the absorption lines.

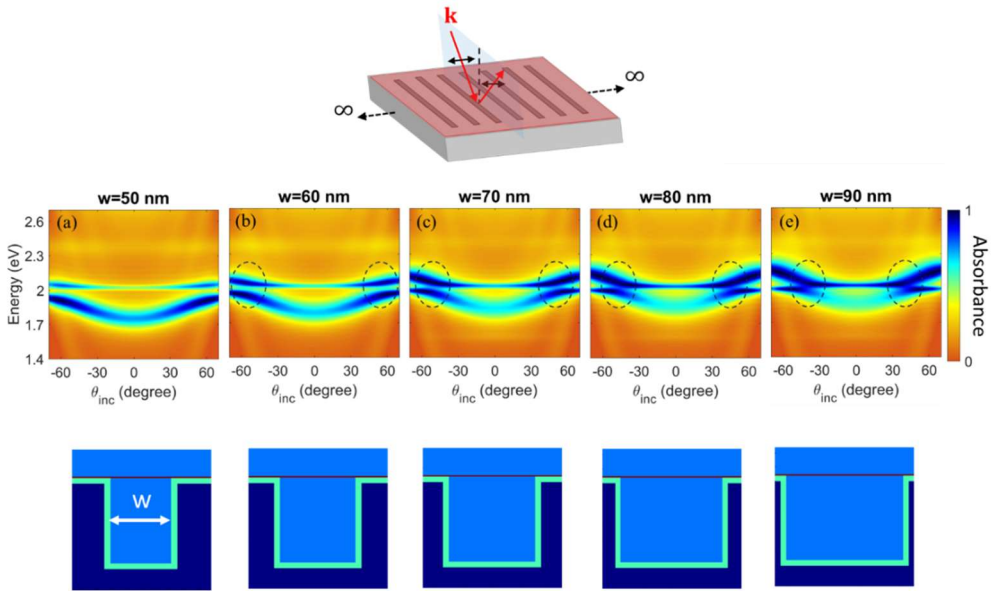

Fig. 3.7 FDTD simulated angle resolved absorption spectra of the hybrid structure with rectangular grooves Λ=400 nm, d=60 nm, and varying widths by scanning θ_{inc} and constant ϕ_{inc}=90°.

We have already investigated the dispersion observed in Fig. 3.7a for the nanogrooves with d=60 nm and w=50 nm. As shown in Fig. 3.4, due to the absence of a local minimum in the ΔE graph (Fig. 3.4b) we do not consider this as a good structure for strong coupling. For the remaining cases, we calculate the amount of Rabi splitting and the range of coupling angles, as we did for the groove depth study.

Fig. 3.8 shows the result of the width study. As a representative for each group of figures, in Fig. 3.8a for the groove with w=60 nm and d=60 nm, we observe splitting in the absorption maxima of the dispersion map at large incident angles. The minimum amount of splitting is 103.33 meV and based on ΔE graph at the bottom left of the box, we find that this splitting occurs at the angles within the range of 61°-65°.

The right panel depicts the absorption spectra for fixed incident angles (θ_{inc} ranging from 0 to 70). The spectra corresponding to the $\theta_{inc} = 65°$ is shown in red.

Now we use eq. (2.5) and (3.1) along with the linewidths of individual components of the hybrid structure to find whether any of these couplings can be classified as strong or not. The result of the calculation is summarized in Table 3.2. As we see, by increasing the groove width, the amount of Rabi splitting and the dissipation rate of the structure increase and the value of the FOM moves away from 1, which is the transition from intermediate to the strong regime. None of the structures in this group fulfill the strong coupling criteria.

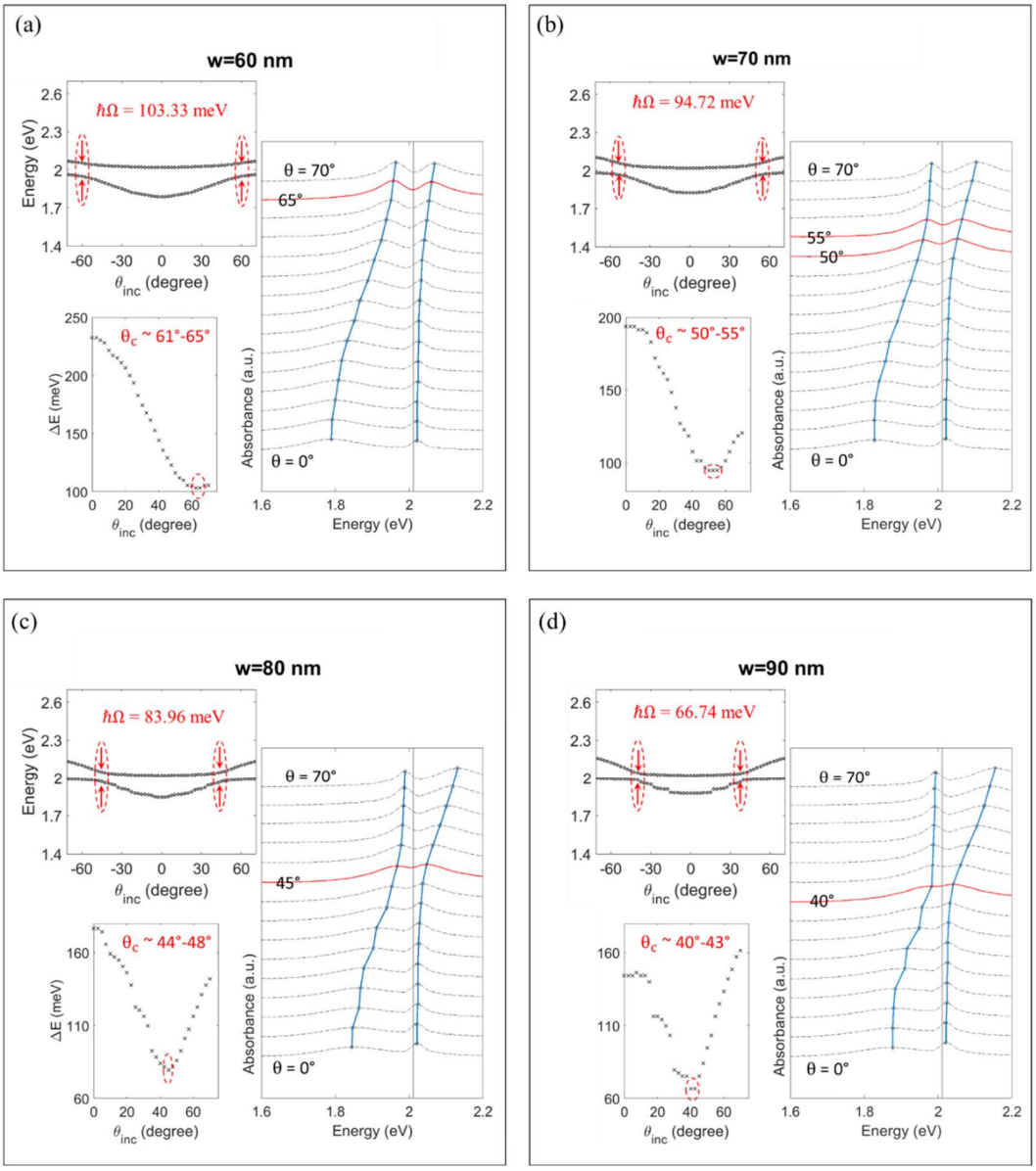

Fig. 3.8 **Top left:** the absorption maxima in the angle-resolved dispersion profiles. **Bottom left:** the energy difference between the upper and lower states (ΔE) as a function of incident angle. **Right:** absorption spectra for different θ_{inc} with the step of 5° for a hybrid structure with rectangular nanogrooves and Λ=400, d=60, (a) w=60 nm. (b) w=70 nm. (c) w=80 nm. (d) w=90 nm. ϕ_{inc}= 90° is constant for all cases.

Table 3.2 Summary of the **groove width** study when the incident angle has k-component along the grooves ($\phi_{inc} = 90°$).

Width Study - $\phi_{inc} = 90°$						
Λ (nm)	d (nm)	w (nm)	shape	$\hbar\Omega_R(meV)$	$\gamma_{av}(meV)$	FOM
400	60	50	rect	Splitting observed. No local minima in ΔE graph.		
		60		103.33	111.33	0.93
		70		94.72	122.16	0.77
		80		83.96	140.37	0.6
		90		66.74	157.77	0.42

3.2.3 Fabrication errors: The effect of groove wall angle and edge roundness on the coupling (ϕ_{inc}= 90°)

In addition to the errors in nominal values of the groove parameters, we also identified two possible geometrical errors. First, the deviation from a straight groove wall, which is quantified by the angle of the groove wall with respect to a perfect straight wall. Second, the deviation from sharp edged groove toward curved edges. We examine the effect of each individual error, while the groove parameters, "Λ", "d" and "w" are constant.

Fig. 3.9 shows the trend of the dispersion graph of a nanogroove with different groove angles with Λ=400, d= 60 and w = 50 nm. By increasing the deviation from a straight wall, we observe blueshift in the absorbance profile of the nanogrooves and following that a decrease in the coupling incident angle. The structure with θ_g= 0° corresponds to the same structure which was already investigated in Fig. 3.4 showing no

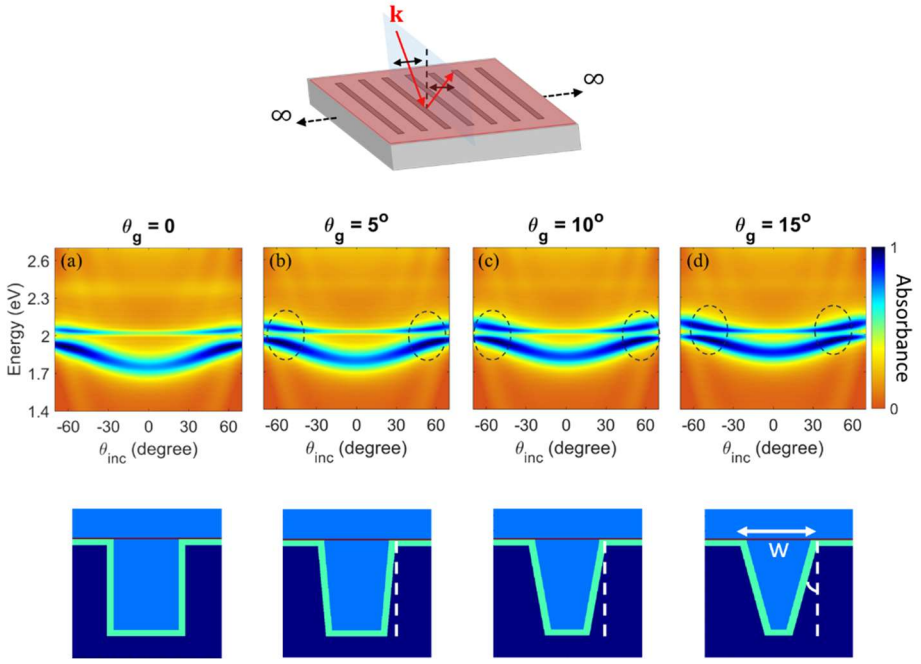

Fig. 3.9 FDTD simulated angle resolved absorption spectra of the hybrid structure with Λ=400 nm, d=60 nm, w=50 nm by scanning θ_{inc} and constant ϕ_{inc}=90°. The groove walls are tilted with varying angles in steps of 5°.

local minimum in the graph of ΔE vs. θ_{inc}. The ΔE plot for nanogrooves with the θ_g = 5° also do not show any local minima (Fig. 3.11) and we take it out of the coupling group. The Rabi splitting and coupling angles for the structures with θ_g= 10° and θ_g= 15° are demonstrated in Fig. 3.10. The value of the Rabi splitting, dissipation rates and FOM are summarized in the Table 3.3. None of the structures in this group satisfy the eq. (2.5) condition and the value of the FOM seems to degrade by increasing the groove wall angle, meaning that the more deviation from straight groove wall degrades the strength of the coupling.

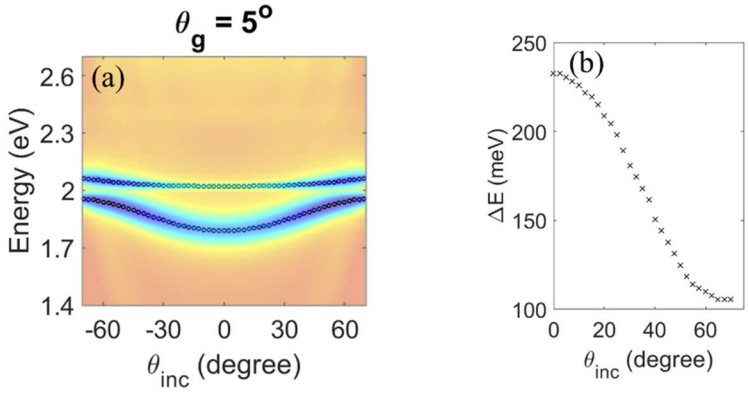

Fig. 3.11 (a)Absorption maxima in the dispersion plot of the structure with Λ=400, d=60, w=50 nm θ_g=5° (b) Energy difference between UEB and LEB as the function of incident angle.

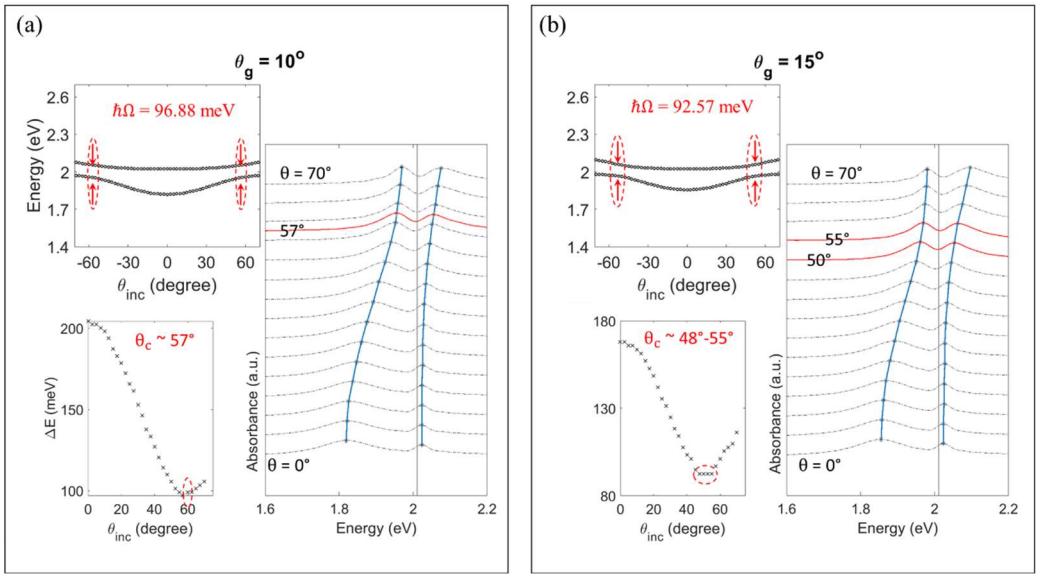

Fig. 3.10 Each figure group contains: Top left: the absorption maxima in the angle-resolved dispersion profiles. Bottom left: the energy difference between the upper and lower states (ΔE) as a function of incident angle. Right: absorption spectra for different θ_{inc} with the step of 5° for a hybrid structure which has nanogrooves with angled walls and Λ=400, d=60, w=50 nm (a) θ_g=10° and (b) θ_g=15°. ϕ_{inc}= 90° is constant for all cases.

Table 3.3 Summary of the **groove wall angle** study when the incident angle has k-component along the grooves ($\phi_{inc} = 90°$).

Groove wall angle Study - $\phi_{inc} = 90°$						
Λ (nm)	d (nm)	w (nm)	shape (θ_g)	$\hbar\Omega_R(meV)$	$\gamma_{av}(meV)$	FOM
400	60	50	0°	Splitting observed. No local minima in ΔE graph.		
			5°	Splitting observed. No local minima in ΔE graph.		
			10°	96.88	101.38	0.96
			15°	92.57	100.46	0.92

Now we proceed to the second error which is the deviation from rectangular shape groove toward curved edges. Fig. 3.12 shows the dispersion graph of curved edge grooves with Λ=400, d = 60 and w = 50 nm with different edge roundness. The amount of

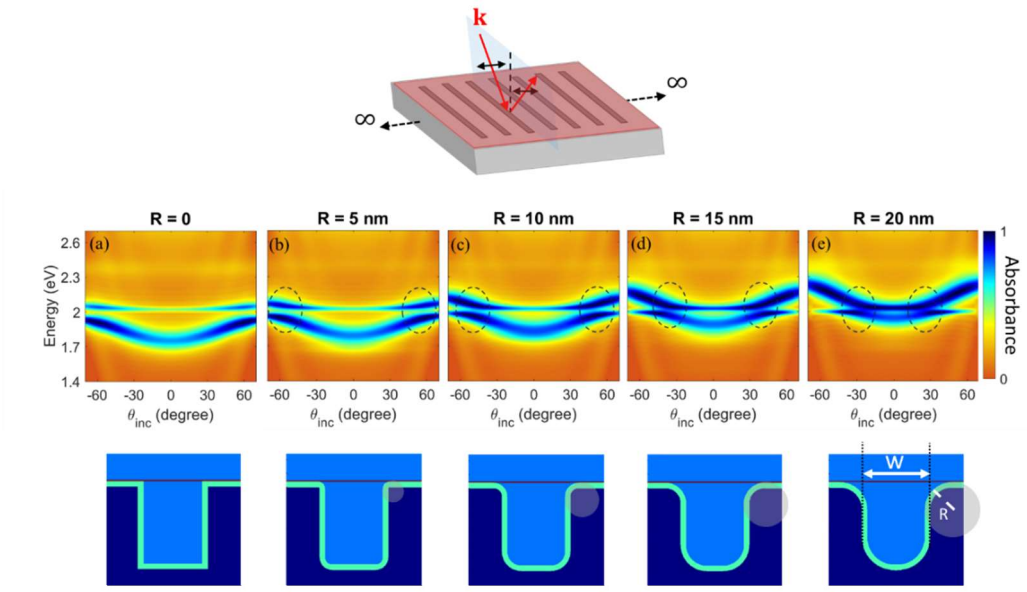

Fig. 3.12 FDTD simulated angle resolved absorption spectra of the hybrid structure with Λ=400 nm, d=60 nm and w=50 nm by scanning θ_{inc} and constant ϕ_{inc}=90°. The groove wall edges are curved with varying radii of curvature.

roundness is quantified by the radius of curvature of internal and external groove edges considering the existence of the 4 nm groove coating.

As the deviation from a sharp-edged groove increases, we observe blueshift in the trend of the graph. The rectangular shape groove with mentioned period, depth and width was out of the coupling group as we verified in Fig. 3.4b. For the other curve edged grooves the condition of coupling is investigated and depicted in Fig. 3.13. The amount of Rabi splitting, average dissipation rates and FOM are calculated and shown in Table 3.4. As we see for the case with R = 5 nm the coupling criteria is rigorously satisfied, however, as we deviate more from rectangular groove shape, the strength of coupling declines. For the the case with R =20 nm, the anti-crossing is not even resolved due to the broadening and small value of the Rabi splitting. This deviation also degrades the condition of strong coupling as the FOM reaches below 0.5.

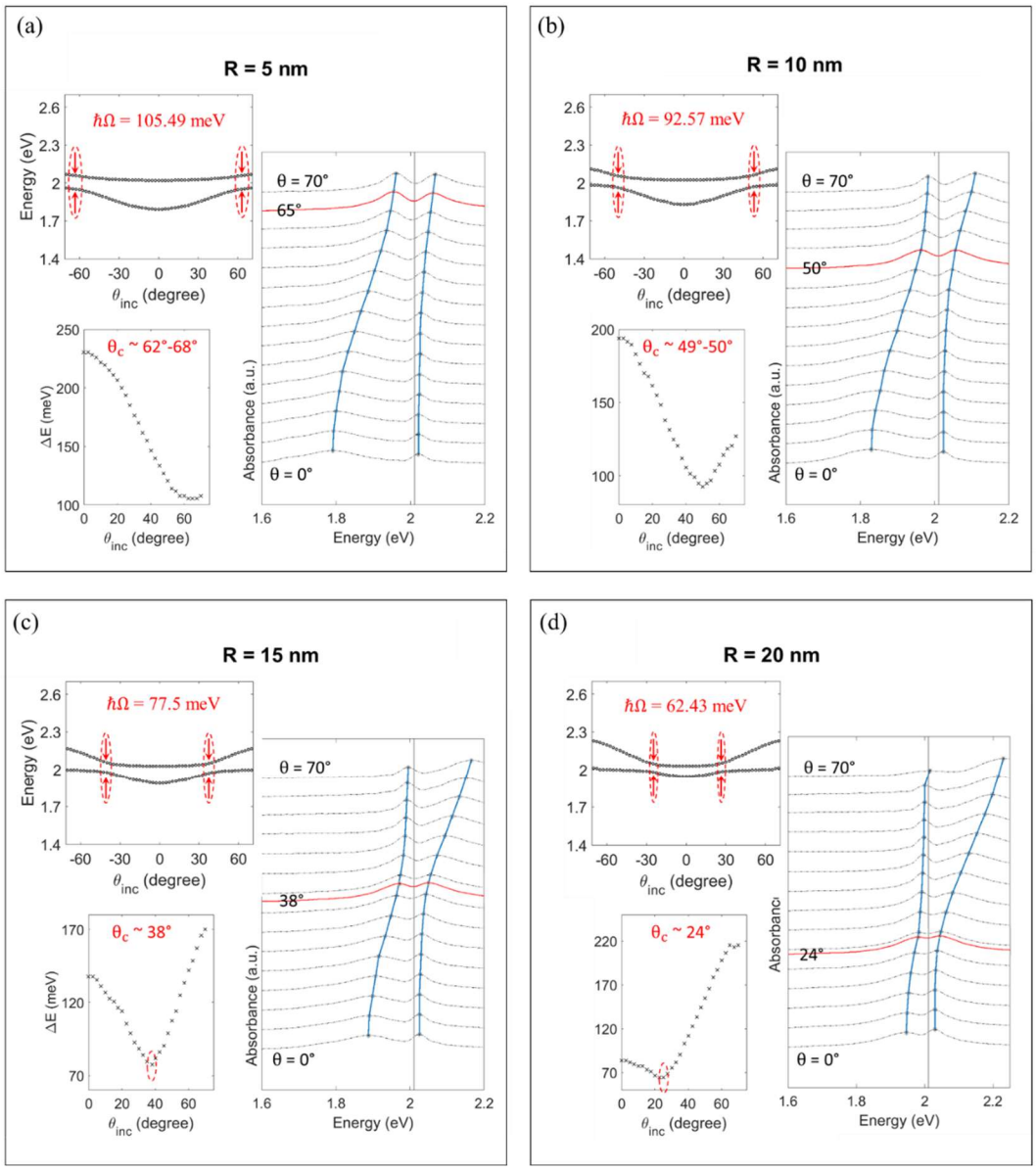

Fig. 3.13 **Top left:** the absorption maxima in the angle-resolved dispersion profiles. **Bottom left**: the energy difference between the upper and lower states (ΔE) as a function of incident angle. **Right:** absorption spectra for different θ_{inc} with the step of 5° for a hybrid structure which has nanogrooves with round edges and Λ=400, d=60, w=50 nm (a) R=5 nm, (b) R=10 nm, (c) R=15 nm and (d) R=20 nm. ϕ_{inc}= 90° is constant for all cases.

Table 3.4 Summary of the **groove edge roundness** study when the incident angle has k-component along the grooves ($\phi_{inc} = 90°$).

Groove Edge Roundness Study - $\phi_{inc} = 90°$						
Λ (nm)	d (nm)	w (nm)	shape (R)	$\hbar\Omega_R(meV)$	$\gamma_{av}(meV)$	FOM
400	60	50	0	Splitting observed. No local minima in ΔE graph.		
			5 nm	105.49	102.99	1.02
			10 nm	92.57	117.14	0.79
			15 nm	77.5	125.8	0.62
			20 nm	62.43	127.63	0.49

All the above-mentioned parameters play an important role in the strength and the region in which the strong coupling occurs. In all cases the coupling is sensitive to deviations from nominal values, but the sensitivity looks more prominent for variations of depth. The above results were obtained for the cases with constant azimuthal angle ϕ_{inc}=90°), however, we need to analyze the dispersion diagrams for ϕ_{inc}= 0° to cover all the possible illumination directions. Since the dispersion graph is more sensitive to the groove depth, only the dependence of dispersion pattern on the groove depth is investigated for the case of ϕ_{inc}= 0.

3.2.4 The effect of depth on the coupling (ϕ_{inc}= 0°)

The dispersion patterns for a sharp-edged rectangular groove with width of 50 nm and varying depths under the incident light with ϕ_{inc}= 0 is shown in Fig. 3.14. Here, we observe more interesting phenomena. First, just like the case for ϕ_{inc}= 90°, we observe

redshift in the groove dispersion as we go toward larger depths. In Fig. 3.14a and Fig. 3.14b the anti-crossing between the plasmonic nanogroove and the "A-exciton" of WS_2 around 2.02 eV is evident. For the depth of 50 nm in Fig. 3.14c the spectral overlap between WS_2 and nanogrooves is not full. In Fig. 3.14d and Fig. 3.14e the absorption profile of the nanogrooves is well below that of WS_2 and there is no anti-crossing between the two profiles.

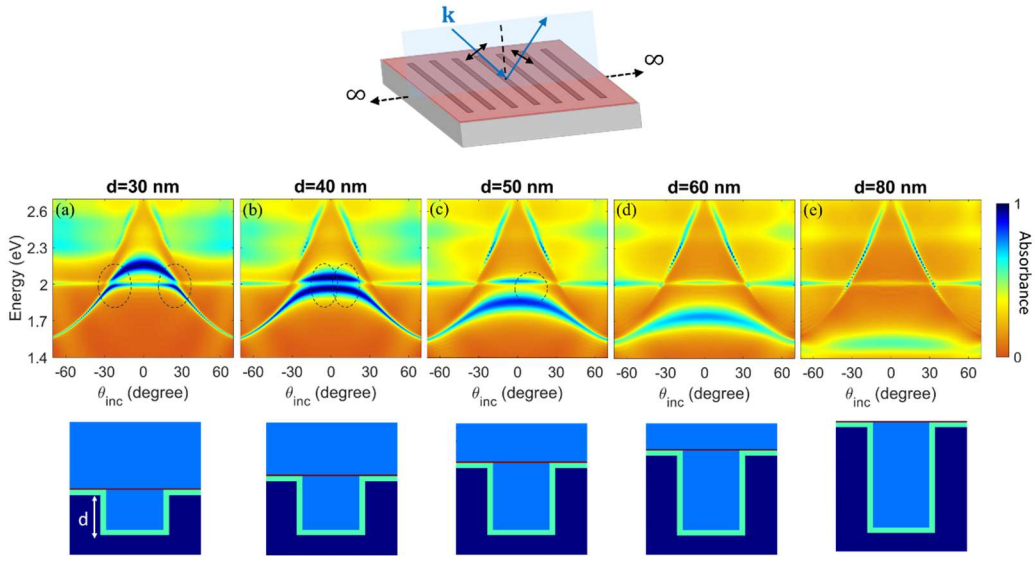

Fig. 3.14 FDTD simulated angle resolved absorption spectra of the hybrid structure with with rectangular grooves Λ=400 nm, w=50 nm, and varying depths by scanning θ_{inc} and constant $\phi_{inc} = 0$.

The sloped line, roughly fixed for all the cases is the Rayleigh anomaly which is a phenomenon that occurs when light interacts with a periodic structure [81]. It results in the appearance of anomalies or deviations in the scattering or diffraction pattern at certain angles. In this kind of anomaly, the scattered wave on the surface of the periodic grating emerges tangential to the surface. As we see, this feature was not present in the Fig. 3.3

dispersions with ϕ_{inc}= 90°, when the incident does not contain any **k**-vector component along the periodicity of the grooves. Writing the grating equation for an incident light with wavevector k_0 and incident angle of θ_{inc} on a periodic grating with periodicity of Λ:

$$k_0\left(sin\theta_{inc} \pm sin\theta_{diff}^{(m)}\right) = \pm mk_g \ , \tag{3.2}$$

with $k_g = \frac{2\pi}{\Lambda}$, $\theta_{diff}^{(m)}$ the m^{th} diffracted order angle, gives the incident angles that correspond to this anomaly. The Rayleigh anomaly solely depends on the gating period, appears in the dispersion of the structure as sharp, discontinuous changes in reflectivity/absorption, and is independent of the grating material [81]. Fig. 3.15a depicts the analytic angles which experience Rayleigh anomaly within the range of scanned energy in our study for a grating with the period of 400 nm. In Fig. 3.15b this anomaly is plotted on top of the dispersion plot from Fig. 3.14c.

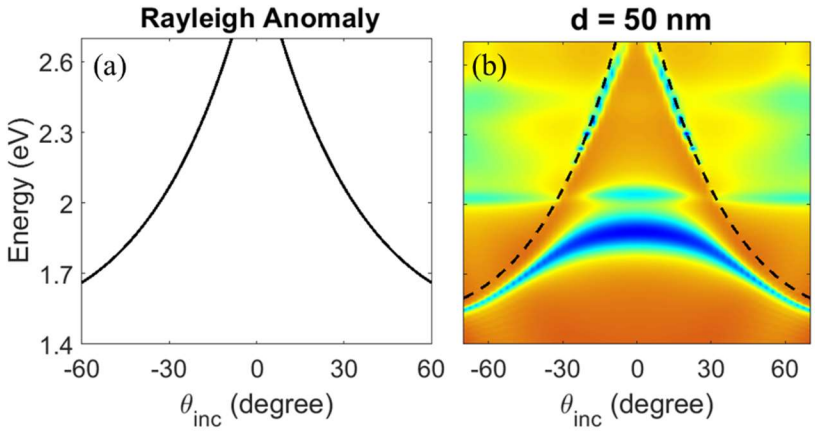

Fig. 3.15 (a) Rayleigh anomaly for a grating with the period of 400 nm derived from Eq. (3.2) (b) The analytic Rayleigh anomaly occurrence on top of the FDTD dispersion from Fig. 3.14c.

To study the the change in the coupling as the function of depth for this case, we follow the same procedure as we did for the cases with ϕ_{inc}= 90°. First, we rule out the cases without obvious mode splitting, which refer to the Fig. 3.14c, d, e with d=50, 60 and 80 nm. The dispersion and coupling in the nanogrooves with d=30 and d=40 nm and two more interim cases with d=35 and d=45 nm is shown in Fig. 3.16. Each box in this figure corresponds to a specific groove depth corresponding dispersion figure. We take out the groove with d=45 nm from coupling group, since in Fig. 3.16d the energy difference plot as the function of incident angle does not show any local minima.

Now using Eq. (2.5) we can check for the strong coupling criteria. The result of calculation for this case is given in the . As we move toward deeper grooves, the amount of splitting between two states increases, while the plasmonic linewidth decreases. For the structure with d=30 nm, despite the lower Rabi splitting compared to other cases, it exhibits a significantly better FOM, making it the structure with the strongest coupling. The nanogroove-WS_2 with d=35 nm also fulfills the criteria for strong coupling, whereas the case with a diameter of 40 nm does not meet the criteria.

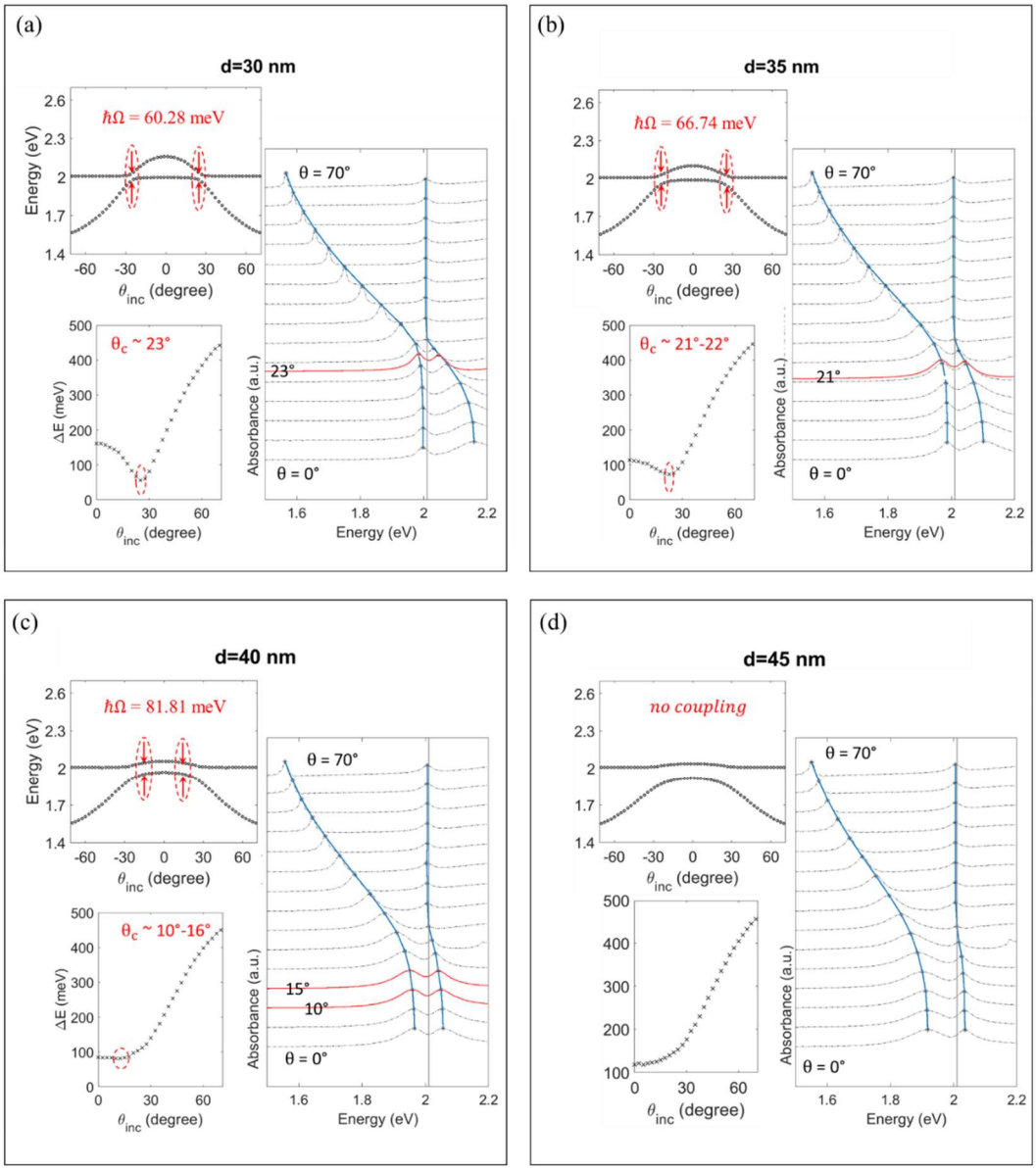

Fig. 3.16 **Top left**: the absorption maxima in the angle-resolved dispersion profiles. **Bottom left**: the energy difference between the upper and lower states (ΔE) as a function of incident angle**. Right:** absorption spectra for different θ_{inc} with the step of 5° for a hybrid structure with rectangular nanogrooves and Λ=400, w=50, (a) d=30 nm. (b) d=35 nm. (c) d=40 nm. (d) d=45 nm. ϕ_{inc}= 0° is constant for all cases.

Table 3.5 Summary of the **groove depth** study when the incident angle has k-component normal to the grooves ($\phi_{inc} = 0°$).

Depth Study - $\phi_{inc} = 0°$						
Λ (nm)	d (nm)	w (nm)	shape	$\hbar\Omega_R(meV)$	$\gamma_{av}(meV)$	FOM
400	✓ 30	50	rect	60.28	51.57	1.48
	✓ 35			66.74	87.48	1.14
	40			81.81	166.64	0.83
	45			Splitting observed. No local minima in ΔE graph.		
	50			No splitting observed.		
	60			No splitting observed.		
	80			No splitting observed.		

3.3 Summary and conclusion

This chapter started by presenting our FDTD findings regarding the impact of nanogroove parameters on the occurrence and strength of strong coupling in the hybrid structure of monolayer WS_2-nanogrooves. We conducted a detailed study on the effects of four isolated parameters, including the groove depth, width, straightness of groove walls, and roundness of the groove edges.

Initially, we recorded the absorption spectra of the hybrid structures by scanning the angle of incidence (θ_{inc}) at constant azimuthal angle of ϕ_{inc}= 90° for grooves, while varying individual parameters. In all cases, the coupling exhibits sensitivity to deviations

from nominal values, but the dependence on groove depth looked more prominent. So, to cover all the possible illumination directions, for the cases with ϕ_{inc}= 0°, we continued to focus on depth variations and studied only the dependence of coupling on the groove depth. Finally, we were able to identify a range of parameters for nanogrooves supporting strong coupling.

In the next chapter, we study the exciton emission routing on the WS_2-nanogroove structures. The effect of groove depth variations on exciton emission routing will be discussed in detail.

CHAPTER 4: DIRECTIONAL PROPAGATION ON WS_2-NANOGROOVE STRUCTURE

4.1 Analytical result

To understand the observed routing analytically, we calculate the Poynting vector of the coupled radiation of a circular dipole at the vicinity of a metallic nanogroove with infinite depth. Just as a reminder, the circular dipole represents the radiative decay of the TMD valley-polarized exciton emission. In order to avoid complications, a single dipole is assumed, although the number of TMD excitons in a real scenario is higher [15].

Fig. 4.1 shows a groove and a nearby single circular dipole. Here, we face 3 kinds of surfaces interacting with the circular dipole, the horizontal part of the surface (S) and the groove walls on the left and right side of the dipole (L , R). We study each surface independently and wrap up the individual results for a conclusion.

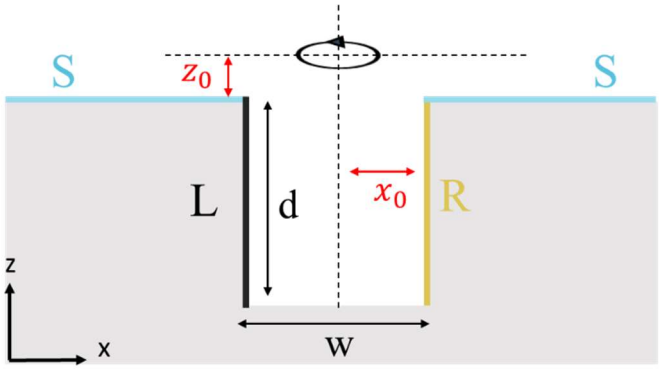

Fig. 4.1 Schematic representation of a single circular dipole close to an individual groove. Three kinds of surfaces are interacting with the nearby dipole.

4.1.1 Poynting vector on the flat horizontal surface

First, we only consider the horizontal part of the surface (S) below a circularly polarized dipole with $[p_x, p_y] = p_0[i + 1]$ to represent the emission from the TMD valleys with momentum K (blue area in Fig. 4.2a). In chapter 2, we described the analytical model to calculate the Poynting vector of a general dipole close to a metallic surface. So considering surface S, the TM component of the vector potential in angular spectrum representation is given by [78]:

$$\mathrm{A(x,y,z)} = \frac{1}{2\pi}\iint_{-\infty}^{\infty} \widehat{\mathrm{A}}(\mathrm{k_x},\mathrm{k_y};\mathrm{z})\, e^{\pm i[k_x(x-x_0)+k_y(y-y_0)+k_z|z-z_0|]} dk_x dk_y \,, \tag{4.1}$$

with the vector potential definition in k-space:

$$\hat{A}(k_x,k_y;z) = \int_{-\infty}^{\infty} dx \int_{-\infty}^{\infty} dy\, A(x,y,z) e^{-i[k_x x + k_y y]} \,, \tag{4.2}$$

that gives:

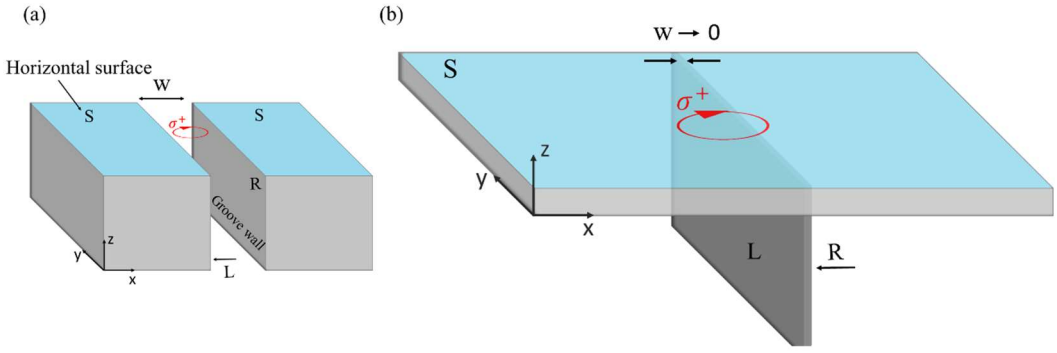

Fig. 4.2 (a) Considering the dipole interaction with horizontal surfaces of the nanogroove (surfaces S , colored blue). (b) Simplification of the analytic integral by assuming the limit of $w \to 0$, corresponding to an infinite flat/horizontal surface below the dipole.

$$\widehat{\mathrm{A}}(\mathrm{k_x}, \mathrm{k_y}; \mathrm{z}) = \frac{\omega\mu\mu_0}{4\pi} \frac{\mp p_x k_x k_z \mp p_y k_y k_z + p_z k_t^2}{k_z(k_t^2)}. \tag{4.3}$$

Here, k_x and k_y are surface propagating wavevectors with $k_t^2 = k_x^2 + k_y^2$ and k_z is the evanescent component normal to the interface with $k_z = \sqrt{k^2 - k_t^2}$ as an imaginary number. In order to solve the integral in eq. (4.2) analytically, we need infinite limits for the integral over dx, while for the case of single groove, based on Fig. 4.1 we will have:

$$\int_{-\infty}^{-w/2} dx + \int_{w/2}^{\infty} dx$$

To resolve this issue, we approximate the limit of $w \to 0$ which is equivalent to a case of flat infinite surface, as shown in Fig. 4.2b. Now the infinite dimensions in x direction are easily achieved.

Based on eq. (4.3), since we have no p_z components for the dipole, the k-space vector potential becomes:

$$\hat{A}(k_x, k_y; z) = \frac{\omega\mu\mu_0}{4\pi} \frac{\mp p_x k_x k_z \mp p_y k_y k_z}{k_z(k_t^2)}. \tag{4.4}$$

Following Eq. (2.11) and (2.13) we calculate the k-space electric field, magnetic field and the Poynting vector of a circular dipole coupled radiation near the surface in Fig. 4.2b. We are detecting the PL on the surface; we just care about in-plane components of the Poynting vector. The Poynting vector in the k_x-k_y plane is:

$$\hat{\mathbf{S}}\left(k_x, k_y; z\right) = \hat{\mathrm{S}}_{\mathrm{x}}\hat{\mathrm{x}} + \hat{\mathrm{S}}_{\mathrm{y}}\hat{\mathrm{y}}\ , \tag{4.5}$$

with $\hat{S}_x$ and $\hat{S}_y$ calculated as:

$$\hat{S}_x(k_x, k_y; z) = \alpha k_x e^{2ik_z|z-z_0|} \ ,$$
$$\hat{S}_y(k_x, k_y; z) = \alpha k_y e^{2ik_z|z-z_0|} \ , \tag{4.6}$$

that gives:

$$|S| = \alpha \ k_t e^{2ik_z|z-z_0|}, \tag{4.7}$$

where α is a wavelength dependent term

$$\alpha = \frac{\omega}{(8\pi^2)^2 \ \varepsilon\varepsilon_0} \frac{p_0^2}{2} \ . \tag{4.8}$$

Fig. 4.3a shows the magnitude of the Poynting vector of a circular dipole with $[p_x, p_y] = p_0[i + 1]$ near a flat metal surface. The Poynting vector is min at the center. Moving further away from the center radially, the exponential term decreases but, k_t

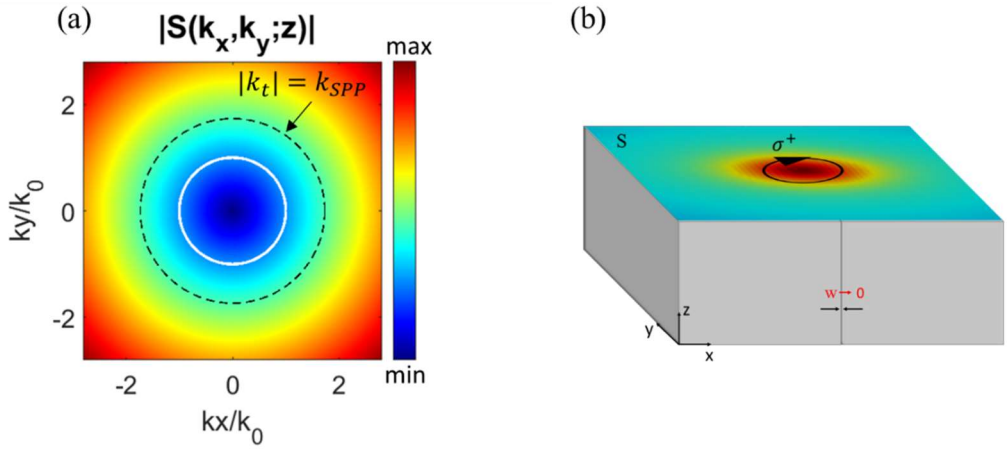

Fig. 4.3 The homogeneous distribution of the magnitude of the Poynting vector of a circularly polarized dipole emission near a flat metal surface (a) in k-space from analytical calculations (b) in real space as an interpretation.

increases dominantly. The dashed circle shows the region in which the in-plane propagation wavevector of the dipole radiation $\vec{k}_t = k_x\hat{x} + k_y\hat{y}$ is equal to the SPP wavevector $k_{SPP} = k_0\sqrt{\frac{\varepsilon_d\varepsilon_m(\omega)}{\varepsilon_m(\omega)+\varepsilon_d}}$ (with k_0 assumed to be incident light wavevector). As is evident, the k-space Poynting vector distribution is highly symmetric where the SPP condition is satisfied (and elsewhere) and no preferred directionality is observed. The interpreted real space picture of such k-space Poynting vector distribution on the surface is shown in Fig. 4.3b.

4.1.2 Poynting vector on the groove walls

Next, to investigate the groove wall effects, the Poynting vector of the same circular dipole for a vertically oriented plane in y-z plane is calculated (Fig. 4.4a). In this scenario, k_y, k_z are in-plane propagating wavevectors, and k_x is the evanescent wavevector in the angular spectrum representation. The same as the previous case, the complexity of the analytical

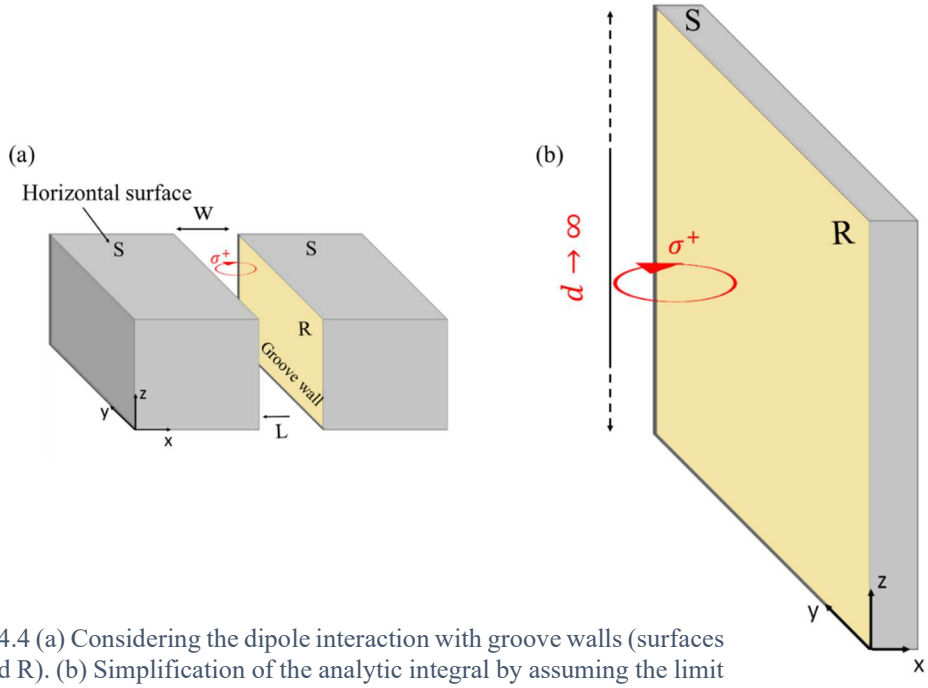

Fig. 4.4 (a) Considering the dipole interaction with groove walls (surfaces L and R). (b) Simplification of the analytic integral by assuming the limit of $d \to 0$, corresponding to a groove with infinite depth.

Fourier integral in eq. (4.2) forces us to consider an infinite wall (groove with infinite depth) as shown in Fig. 4.4b. Now the vector potential for the interaction of the dipole near surfaces R and L will become:

$$\hat{A}(k_y, k_z; x) = \frac{\omega\mu\mu_0}{4\pi} \frac{\mp p_y k_y k_x + p_x k_t^2}{k_x(k_t^2)} \ . \tag{4.9}$$

The sign $\mp$ depends on the location of the dipole with respect to the groove walls. Considering the interaction of the dipole with the left or right groove wall the upper and lower sign will be adopted, respectively. Similar to the method used for surface S, the y component of the Poynting vector on the groove walls is obtained as:

$$\hat{\mathbf{S}}_{\mathrm{y}}(\mathrm{k_y}, \mathrm{k_z}; \mathrm{x}) = \alpha \frac{k_y}{k_t^2 \ k_x^2} \left[k_t^2 \mp k_y \kappa_x\right] e^{2ik_x|x-x_0|} \ , \tag{4.10}$$

with $k_t^2 = k_y^2 + k_z^2$ as the total SPP wavevector and $k_x = \sqrt{k^2 - (k_t^2)} = i\kappa_x$ as an imaginary number. First, we assume the dipole emission near the left wall in Fig. 4.4a which takes the $-$ sign. The bracket demonstrates interference behavior and has two real terms: k_t^2 is always positive and the term $k_y\kappa_x$ with the sign depending on the sign of k_y, which is the propagation direction along y axis. For propagation along $+y$, $k_y > 0$ and the term inside the bracket is a subtraction, while having $k_y < 0$, the two terms add up to reinforce each other. This implies that the the propagation along $+y$ is suppressed, while $-y$ is enhanced. The magnitude of the y component of the Poynting vector in k-space for the left groove wall based on the derived analytic formula of Eq. (4.10) is shown in Fig. 4.5a with k_0 as the wavevector of air to be the dielectric medium. Fig. 4.5b shows the

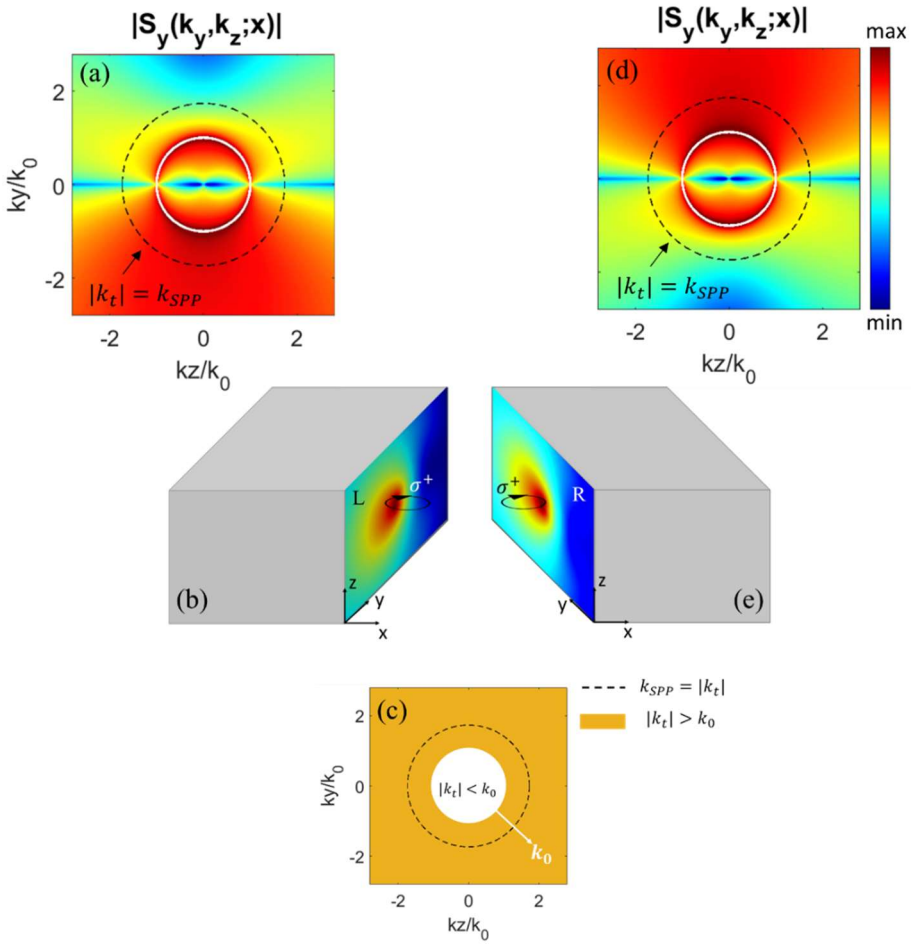

Fig. 4.5 (a) The k-space magnitude of Sy on the left infinite groove wall based on the analytic result. (b) Interpretation of the k-space distribution in real space. (c) Illustration on the behavior of the Poynting vector at different regions. The white area is where we have $k_0 > k_t$, which is inside the light cone. The colored area is out of light cone and where we have $k_t > k_0$. SPP momentum matching $k_{SPP} = k_t$ is satisfied outside the light cone. The black dashed circle represents the total k_{SPP} on the *y*-*z* plane. (d),(e) k-space and interpreting real space Poynting vector distribution for the right groove wall.

interpreted real space picture of the field distribution on the left groove wall. The figure explicitly indicates asymmetric distribution in the k_y-k_z plane outside the white circle. To clarify, in Fig. 4.5c, the colored area is the region in which $k_t > k_0$ (outside the light cone)

and the white area shows $k_t < k_0$ (inside the light cone). The SPP condition implies that $k_x^2 < 0$. Considering the momentum matching relation

$$\mathrm{k}_0^2 - k_{SPP}^2 = k_x^2 \ , \tag{4.11}$$

SPP condition is only satisfied outside of the light cone, meaning that we need to look at the colored area to see the role of SPP in directionality. In this area the distribution is asymmetric. However, the corresponding area to the white circle in Fig. 4.5a, is inside the light cone, perfectly symmetric, and with uniform distribution. So, the directionality is solely attributed to the propagating SPPs on the groove wall.

For the other groove wall (surface R) , we need to consider the + sign, which will indicate the opposite directionality with the same reasoning as shown in Fig. 4.5d and e.

4.1.3 Conclusion of the analytical calculation

In the last two sections we investigated the interaction of the dipole with each individual surfaces S, L and R. The result demonstrated homogeneous distribution of the Poynting vector on the horizontal part of the surface and asymmetric distribution on nanogroove walls based on the helicity of the nearby dipole. Fig. 4.6a wraps up the analytic result by showing all three individual surfaces and the corresponding real space Poynting vector distribution. What we are looking for is the proportion on the horizontal plane. The upper edge of the grooves is a shared boundary between the horizontal surface and the walls and incorporates groove wall's contribution to the detected field on the surface. So, the final detected field on the surface will take an asymmetric pattern, although the horizontal surface alone does support symmetrical. A pictorial explanation is demonstrated in Fig. 4.6b.

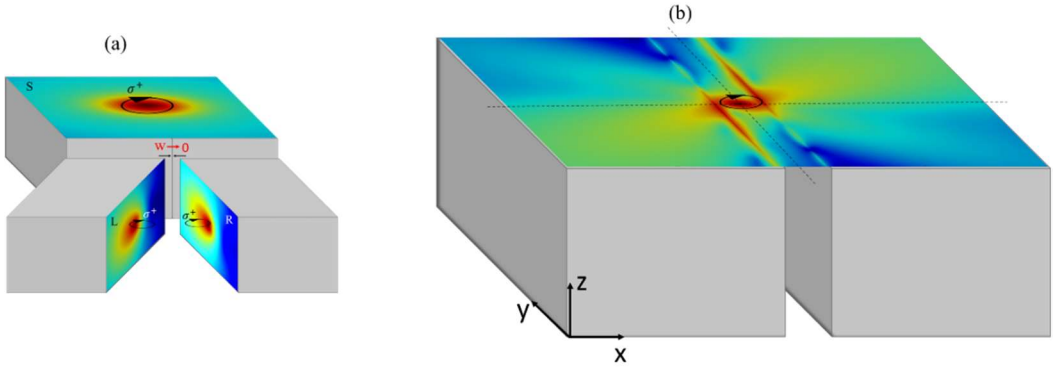

Fig. 4.6 (a) Interpretation of the analytic result for all the individual involved surfaces: horizontal surface (S) and two groove walls (L & R) with left-handed circular dipole as the excitation source. (b) The final Poynting vector distribution on the surface of the grating, considering all surfaces.

Although the above analytic study is proof of directional propagation detection on the surface, our calculations were based on two approximations. we have initially assumed a single nanogroove with zero width and infinite depth, which is unrealistic. In practice, several number of grooves will be targeted by the spot size of the incident beam. Therefore, the contribution of the groove edges on the horizontal plane field can add up and show a more significant effect. For the real case of arrayed nanogrooves with finite depth, and to find the relation between DCP and nanogroove parameters, we need to employ numerical calculations. In the next part, the numerical study of the groove depth using FDTD simulation is presented.

4.2 Numerical calculation of k-space images

Before demonstration of the valley exciton emission in the hybrid structure of WS_2-nanogrooves, we first calculate the unpolarized k-space (far-field) images for different

groove depths using FDTD software. With a linear dipole (P_x) representing the unpolarized TMD valley exciton emission, a sufficiently large simulation region and monitor are designed to minimize the effects of field truncation at the boundaries of the monitor. Using the collected near-field data by the black in-plane monitor in Fig. 4.7, we detect the far-field images as explained in section 2.2.1.

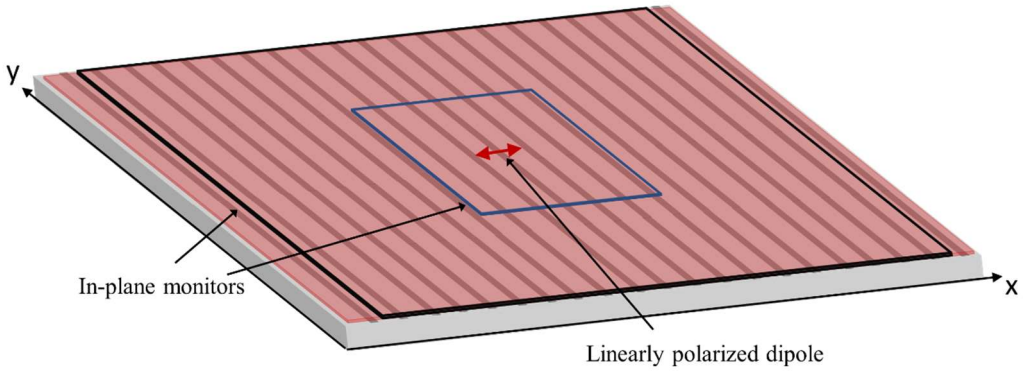

Fig. 4.7 The simulation setup for obtaining far field images. Blue and black rectangles represent two surface monitors, different in size, recording the near-field data.

To ensure the accuracy of far-field projections, it is essential that all the near-field radiation propagating to the far-field passes through the designated monitor on the surface. The assumptions made by far-field projection functions in FDTD assume that electromagnetic fields are negligible beyond the boundaries of the monitor. This effectively truncates the near-fields at the monitor edge and such truncation results in the presence of high-frequency ripples in the far-field projected data. The far-field filter option in FDTD allows us to apply a spatial filter to the near-field data, smoothly reducing the field to zero. When the fields go more smoothly to zero, instead of an abrupt cut, the

high frequency ripple is removed from the projection. Fig. 4.8a and c show the raw far-field image for a specific structure calculated from the blue and black monitors in Fig. 4.7, respectively. Although derived from the same simulation, the images look different, because a larger fraction of the near-field data from the blue monitor is truncated. Fig. 4.8b and d display the respective far-field data from the blue and black monitors, with the spatial filter implemented. The filter has effectively removed the ripples caused by field truncation at the boundaries of the monitor, however the total pattern for the larger monitor is less manipulated by the filter. Ideally, an excessively large monitor would be required to eliminate ripples, which is impractical. However, we aimed for time-wise efficiency and selected a monitor size that sufficiently minimizes manipulation. The interpretations of the far-field images will be discussed later in this section.

Fig. 4.9 illustrates the unpolarized far-field images of the grooves with depths corresponding to the structures exhibiting mode splitting in the absorption profile of the WS_2-nanogroove structure, as outlined in the depth-dispersion study in the sections 3.2.1

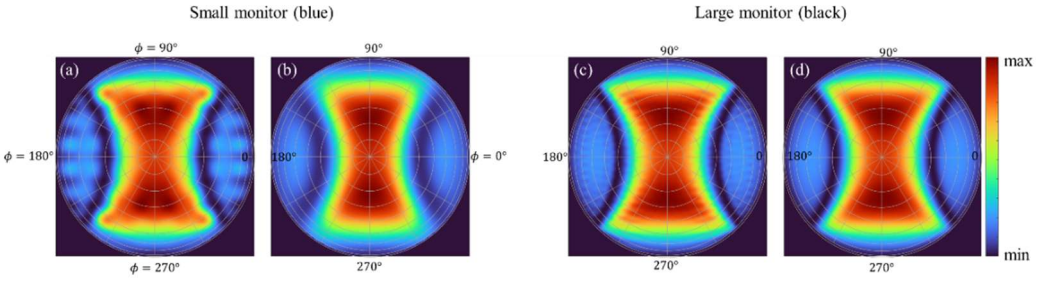

Fig. 4.8 The effect of monitor size and spatial filter on the far-field electric field patterns obtained from projection of data from surface monitors in Fig. 4.7. (a) Raw Far-field from small monitor. (b) Spatially filtered Far-field from from small monitor. (c) Raw Far-field from large monitor. (d) Spatially filtered Far-field from from large monitor.

(for ϕ_{inc} = 90°) and 3.2.4 (for ϕ_{inc} = 0°). To have better images with resolved colors, each figure is normalized to its own maximum intensity.

Before proceeding further, let's get some insight into the far-field images interpretation. As we move from shallow grooves to deeper ones, the field intensity distributes more along the vertical axis (k_y). This is in accordance with our dispersion data in the previous chapter. As shown in Table 4.1, the shallower gratings with a larger FOM demonstrate more pronounced coupling when ϕ_{inc}= 0°. By increasing the groove depth, the coupling for the cases with ϕ_{inc}= 90° becomes prominent. Based on Fig. 2.4, when ϕ_{inc}= 0°, there is no k_y component provided by the incident planewave and following the conservation of momentum [82], the SPPs generated in the structure do not possess k_y (net momentum component along y direction). The same holds for the cases with ϕ_{inc}= 90° and k_x component. So, when ϕ_{inc}= 0°, the coupling corresponds to a net SPP propagation along x axis, just as the coupling for the cases with ϕ_{inc}= 90° corresponds to propagation along y axis.

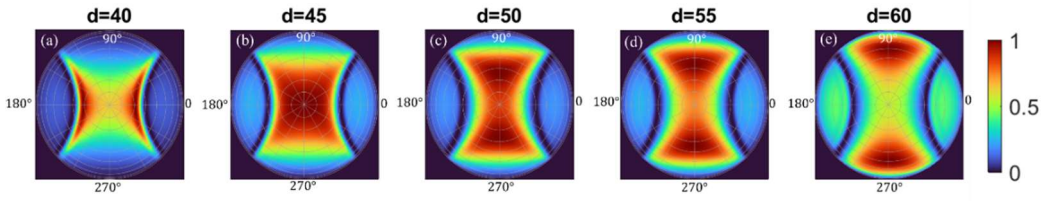

Fig. 4.9 Far-field intensity images and their relation to the dispersions for nanogrooves with Λ=400 nm, w=50 and varying groove depths. The azimuthal angle in such polar image ranges from 0 to 2π covering the whole region of the in-plane monitor.

Table 4.1 Comparing the trend in FOM variations as the result of groove depth changes.

Depth Study					
Λ (nm)	d (nm)	w (nm)	shape	FOM $\phi_{inc} = 0°$	FOM $\phi_{inc} = 90°$
400	30	50	rect	1.48	No splitting.
	40			0.83	0.79
	45			Splitting at the edge.	0.86
	50			No splitting.	0.89
	55			No splitting.	1.02
	60			No splitting.	Splitting at the edge
	80			No splitting.	No splitting.

In the far-field simulations, all the **k** components are provided by a dipole as the source. The shallower structures weakly couple with the k_y components though. The same scenario holds for the deeper grooves and k_x component. So, we expect that by increasing the groove depth, further propagation is supported along the grooves (channel polaritons on the groove walls), and this is what we observe in the far filed images with enhanced intensity along y direction (Fig. 4.9d and Fig. 4.9e). For the nanogroove structure with d=40, 45 nm, coupling in both directions is possible, and this is why the far-field pattern shows hybrid distribution along vertical and horizontal axis (Fig. 4.9a and Fig. 4.9b).

Also, there is no directionality observed in these unpolarized far-field images, and the reason is that due to the linear excitation source, the created valley exciton emissions

are expected to have equal populations at both K and K′ valleys. In the next section, we investigate the capability of these hybrid structures in separating right/left-handed circularly polarized emission, which defines the ability of the structure to support directionality.

4.3 Separation of valley-polarized emission in k-space

After realizing the formation of the unpolarized k-space PL distribution, we move on to examine the polarization-dependent PL of the coupled WS_2-nanogroove arrays. As mentioned earlier, PL emission from different valleys of WS_2 carries opposite circular polarizations. In the experiments, this separation can be accomplished by using a combination of polarizers and waveplates in the detection path. In our simulated k-space images, we separate different circular polarizations by separating the electric field components through $E_x \pm iE_y$ with the negative sign for right-handed (σ^-) emission and the positive sign for left-handed (σ^+) emission. Fig. 4.10 shows the polarization resolved k-space images by varying groove depth. A separated emissions of σ+ and $\sigma -$ polaritons in the momentum space can be observed in all cases. This separation qualitatively indicates that the polaritons at the K and K′ valleys are routed in opposite directions.

To quantify the performance of the hybrid structure in routing, we calculated the degree of circular polarization (DCP) and chiral coupling strength (κ_{chiral}) in k-space from Eqs. (2.14) and (2.16), and the calculation is given in Fig. 4.11a and Fig. 4.11b, respectively. From the figures we see that, although the value of DCP reaches up to 1,

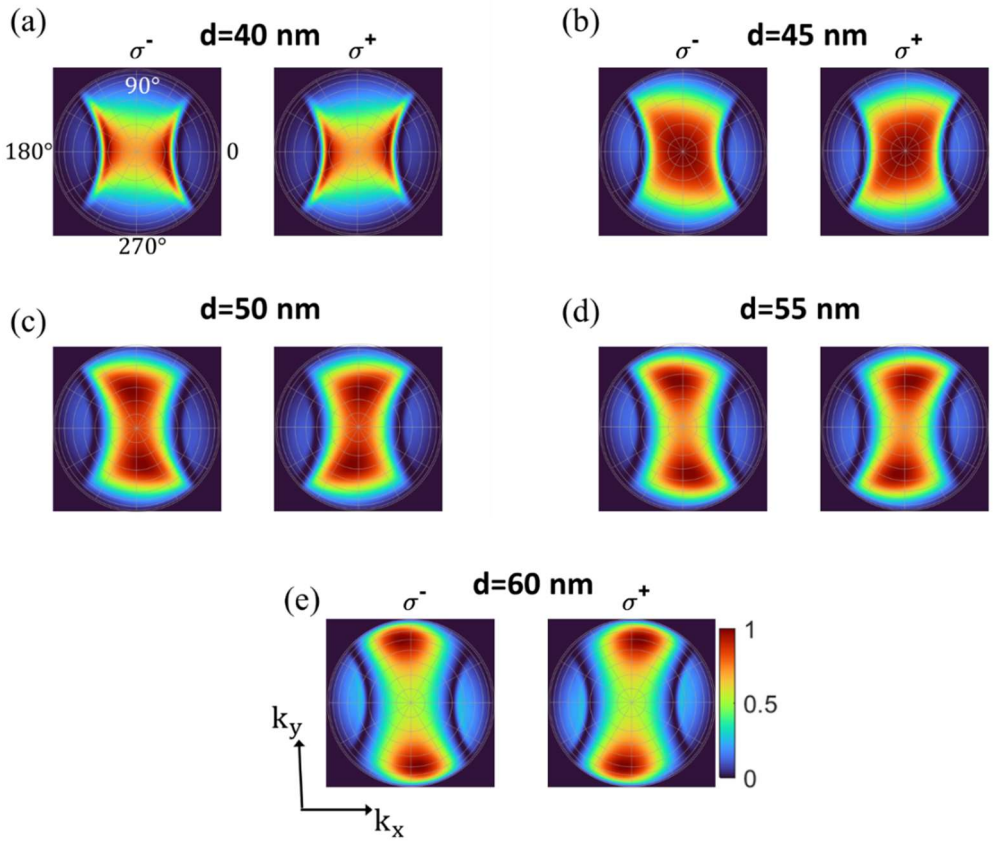

Fig. 4.10 Polarization resolved far-field images for nanogrooves with Λ=400 nm, w=50 and varying groove depths. In each group left to right: σ^- component measured with $E_x - iE_y$ and σ^+ component measured with $E_x + iE_y$, respectively.

which means 100% efficiency in separating opposite circular polarizations, the κ_{chira} for our studied structures does not exceed 0.16.

In Fig. 4.11b from left to right, we observe that by increasing the depth of the nanogrooves the amount of κ_{chi} increases. Such trend supports our analytic calculations indicating that the directionality of the structure is triggered by the modes propagating along the groove and the SPPs generated on the groove walls.

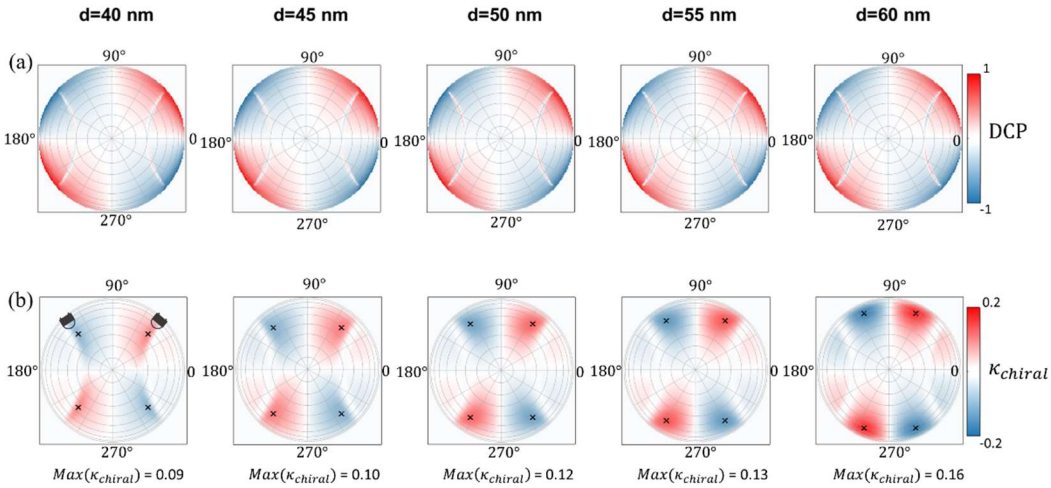

Fig. 4.11 (a) DCP and (b) chiral-coupling strength in k-space for nanogrooves with Λ=400 nm, w=50 and varying groove depths.

As mentioned in the chapter 2, the maximum value of κ_{chira} at any k-space location is an indicator of the best "coupling and DCP" in the structure. Also, the point with maximum value of κ_{chiral} can be an indicator of the angle of propagation on the surface with the best overall performance of the system. We defined such angle in for the studied structures and are shown by cross mark in Fig. 4.11b. The angular coordinate of this point increases as we move toward deeper grooves. This fact can be a guideline to spot the monitor for detection purposes.

4.4 Summary and conclusion

To understand the spatial separation of monolayer TMD valley excitons in the vicinity of a plasmonic nanogroove array, this chapter started with an analytical calculation for an ideal case. We calculated the Poynting vector of a circularly polarized dipole, as a representative of the valley-polarized exciton emission, near a single groove with infinite dimensions. The analytical computation aligns with experimental findings that suggest an "inclined orientation" in the PL resulting from opposite circular polarizations on the surface. However, in practice, more than one groove of the array is illuminated by the spot size of the incident beam. So, the detected field intensities in real experiments would be the collective response of several nanogrooves. Also, with the assumption of infinite dimensions for the slit, we were unable to observe the impact of groove parameters, such as width and depth, on the structure's performance.

Numerical study using FDTD simulations can be employed as an approach to facilitate transition from the ideal scenario to a real case. To this aim, we detected k-space intensity of a linear dipole emission located above the plasmonic nanogroove array. Then, the σ^+ and σ^- components of the PL emission in k-space were separated through post-processing. These components serve as the valley-polarized emissions of the TMD. The distinct emission patterns of σ^+ and σ^- components in momentum space indicate polarization-dependent routing of PL in different directions. Such distinct emission directions implies that the helicity of photons determines a preferred emission direction.

Finally, to quantify the relation between different groove depths and the performance of the structure, we calculated the degree of circular polarization (DCP) and chiral coupling strength (κ_{chira}). The chiral coupling strength is introduced as a rough measure of dominance of σ^+ and σ^- components in plasmon-exciton emissions with different polarization.

CHAPTER 5: SUMMARY & CONCLUSION

The idea of this research is to optimize the design of a miniature structure capable of generating a binary optical system to be utilized in electro-optical circuits. The most significant features of the output of this structure are the high efficiency and maximum separability of the two states. We have used the recently introduced 2D materials (monolayer TMDs) to provide a 2-state physical system as a bit source. Locked valley-spins in TMDs exhibit distinct responses to opposite circular polarizations of incident light. The purpose is to spatially separate the two excitations with high intensity. The excitations decay very fast at room temperature though. To maintain the high intensity and further the propagation distance, the coupling of the exciton emission to SPP modes is employed. To this end, TMD is placed on top of a metallic (silver) plate. However, the SPPs on a uniform metallic surface do not differentiate between the two valley-spin states of in-plane TMD excitons. To resolve the issue of indistinguishability of the flat surface, nanogrooves are carved on the metal slab. The groove walls, being perpendicular to the plane of TMD excitons, exhibit distinct responses from different valley-spins. This is proved theoretically through analytical calculation of the Poynting vector of a circular dipole near a nano-slit with infinite depth. This feature results in the propagation of SPPs, generated by distinct circular polarizations, in opposite inclined orientations. This feature facilitates the separation of the two bits.

The nanogrooves are designed as a rectangular shape with nominal values of depth and width. However, due to fabrication limitations, errors are indispensable. The

optimization is done by analyzing the effects of nanogroove parameters such as depth, width, sharpness of edges and the verticality of the groove walls with the aid of FDTD method. To quantify the strength of coupling between plasmons and excitons, the concept of Rabi splitting is introduced. Rabi splitting is a measure of the amount of splitting between the absorption profiles of TMDs and nanogrooves. We observed that the amount of Rabi splitting is sensitive to depth more than other parameters of the grooves. On the other hand, since the walls were analytically proved to be responsible for the directionality of SPPs propagation, the separation of the two circular polarizations is highly dependent on the depth. Therefore, by analyzing the combination of dispersion profiles and valley polarized k-space images in FDTD, we are able to find the nanogroove parameters, which can provide the best performance with valley-contrasting propagation. We evaluated the structure's ability to separate valley-polarized exciton emission by the chiral coupling strength parameter (κ_{chira}). This parameter captures the structure overall effectiveness in achieving valley-polarized routing with high-strength. A larger maximum value of κ_{chir} makes any structure a better candidate as an interface between photonic and valleytronic devices.

The study can be further improved by investigating the higher orders of the plasmonic mode inside the nanogrooves. By designing a hybrid structure involving monolayer TMD-plasmonic arrays with deeper nanogrooves, while keeping the system in the strong coupling regime, the chiral coupling strength of the system can be investigated. This would be advantageous, considering that the literature suggests such a structure can offer angle-independent strong coupling between the plasmonic and excitonic modes [58]. Additionally, an increased contribution of the channel mode in deeper grooves may

enhance the performance of the structure. This is supported by our findings, demonstrating that directionality is primarily facilitated by the mode inside the groove. This research can serve as a guideline for designing structures and pave the way to transport and read out the spin and valley degrees of freedom of valley excitons in two-dimensional materials, thereby contributing to potential applications in Valleytronics.

REFERENCES

[1] S. A. Wolf *et al.*, “Spintronics: A Spin-Based Electronics Vision for the Future,” *Science (80-.).*, vol. 294, no. 5546, pp. 1488–1495, Nov. 2001.

[2] I. Žutić, J. Fabian, and S. Das Sarma, “Spintronics: Fundamentals and applications,” *Rev. Mod. Phys.*, vol. 76, no. 2, p. 323, Apr. 2004.

[3] S. A. Vitale *et al.*, “Valleytronics: Opportunities, Challenges, and Paths Forward,” *Small*, vol. 14, no. 38, pp. 1–15, 2018.

[4] O. Gunawan, Y. P. Shkolnikov, K. Vakili, T. Gokmen, E. P. De Poortere, and M. Shayegan, “Valley susceptibility of an interacting two-dimensional electron system,” *Phys. Rev. Lett.*, vol. 97, no. 18, pp. 1–4, 2006.

[5] K. S. Novoselov *et al.*, “Electric field in atomically thin carbon films,” *Science (80-.).*, vol. 306, no. 5696, pp. 666–669, Oct. 2004.

[6] K. S. Novoselov *et al.*, “Two-dimensional gas of massless Dirac fermions in graphene,” *Nat. 2005 4387065*, vol. 438, no. 7065, pp. 197–200, Nov. 2005.

[7] Y. Zhang, Y. W. Tan, H. L. Stormer, and P. Kim, “Experimental observation of the quantum Hall effect and Berry’s phase in graphene,” *Nat. 2005 4387065*, vol. 438, no. 7065, pp. 201–204, Nov. 2005.

[8] D. Xiao, W. Yao, and Q. Niu, “Valley-contrasting physics in graphene: Magnetic moment and topological transport,” *Phys. Rev. Lett.*, vol. 99, no. 23, p. 236809, Dec. 2007.

[9] W. Yao, D. Xiao, and Q. Niu, “Valley-dependent optoelectronics from inversion symmetry breaking,” *Phys. Rev. B - Condens. Matter Mater. Phys.*, vol. 77, no. 23, p. 235406, Jun. 2008.

[10] K. F. Mak, C. Lee, J. Hone, J. Shan, and T. F. Heinz, “Atomically thin MoS2: A new direct-gap semiconductor,” *Phys. Rev. Lett.*, vol. 105, no. 13, p. 136805, Sep. 2010.

[11] A. Splendiani *et al.*, “Emerging photoluminescence in monolayer MoS2.,” *Nano Lett.*, vol. 10, no. 4, pp. 1271–1275, Apr. 2010.

[12] G. Eda, H. Yamaguchi, D. Voiry, T. Fujita, M. Chen, and M. Chhowalla, “Photoluminescence from chemically exfoliated MoS 2,” *Nano Lett.*, vol. 11, no. 12, pp. 5111–5116, Dec. 2011.

[13] H. Zeng, J. Dai, W. Yao, D. Xiao, and X. Cui, “Valley polarization in MoS 2 monolayers by optical pumping,” vol. 7, no. June, 2012.

[14] K. F. Mak, K. He, J. Shan, and T. F. Heinz, “Control of valley polarization in monolayer MoS2 by optical helicity,” *Nat. Nanotechnol.*, vol. 7, no. 8, pp. 494–498, 2012.

[15] J. Sun *et al.*, “Strong plasmon-exciton coupling in transition metal dichalcogenides and plasmonic nanostructures,” *Nanoscale*, vol. 13, no. 8, pp. 4408–4419, 2021.

[16] H. Zeng, J. Dai, W. Yao, D. Xiao, and X. Cui, “Valley polarization in MoS 2 monolayers by optical pumping,” *Nat. Nanotechnol.*, vol. 7, no. 8, pp. 490–493, 2012.

[17] T. Cao *et al.*, “Valley-selective circular dichroism of monolayer molybdenum disulphide,” *Nat. Commun.*, vol. 3, no. May, pp. 885–887, 2012.

[18] S. Haroche and D. Kleppner, “Cavity Quantum Electrodynamics,” *Phys. Today*, vol. 42, no. 1, pp. 24–30, Jan. 1989.

[19] S. Haroche and J. M. Raimond, “Exploring the Quantum: Atoms, Cavities, and Photons,” *Explor. Quantum Atoms, Cavities, Photons*, pp. 1–616, Jan. 2010.

[20] S. Wang *et al.*, “Phase transition of a perovskite strongly coupled to the vacuum field,” *Nanoscale*, vol. 6, no. 13, pp. 7243–7248, Jun. 2014.

[21] C. J. Hood, M. S. Chapman, T. W. Lynn, and H. J. Kimble, “Real-Time Cavity QED with Single Atoms,” *Phys. Rev. Lett.*, vol. 80, no. 19, p. 4157, May 1998.

[22] H. Deng, G. Weihs, C. Santori, J. Bloch, and Y. Yamamoto, “Condensation of Semiconductor Microcavity Exciton Polaritons,” *Science (80-.).*, vol. 298, no. 5591, pp. 199–202, Oct. 2002.

[23] J. P. Reithmaier *et al.*, “Strong coupling in a single quantum dot–semiconductor microcavity system,” *Nat. 2004 4327014*, vol. 432, no. 7014, pp. 197–200, Nov. 2004.

[24] J. Kasprzak *et al.*, “Bose–Einstein condensation of exciton polaritons,” *Nat. 2006 4437110*, vol. 443, no. 7110, pp. 409–414, Sep. 2006.

[25] T. Yoshie *et al.*, “Vacuum Rabi splitting with a single quantum dot in a photonic crystal nanocavity,” *Nat. 2004 4327014*, vol. 432, no. 7014, pp. 200–203, Nov. 2004.

[26] K. Hennessy *et al.*, “Quantum nature of a strongly coupled single quantum dot–cavity system,” *Nat. 2006 4457130*, vol. 445, no. 7130, pp. 896–899, Jan. 2007.

[27] N. J. Halas, S. Lal, W. S. Chang, S. Link, and P. Nordlander, “Plasmons in strongly coupled metallic nanostructures,” *Chem. Rev.*, vol. 111, no. 6, pp. 3913–3961, Jun. 2011.

[28] V. Giannini, A. I. Fernández-Domínguez, S. C. Heck, and S. A. Maier, "Plasmonic nanoantennas: Fundamentals and their use in controlling the radiative properties of nanoemitters," *Chem. Rev.*, vol. 111, no. 6, pp. 3888–3912, Jun. 2011.

[29] G.-C. Guo *et al.*, "Quantum plasmonics: new opportunity in fundamental and applied photonics," *Adv. Opt. Photonics, Vol. 10, Issue 4, pp. 703-756*, vol. 10, no. 4, pp. 703–756, Dec. 2018.

[30] X. Zong, L. Li, K. Yu, and Y. Liu, "Strong coupling between hybrid plasmonic–photonic resonances and excitons in metallic photonic crystal–monolayer WS2 nanostructures," *Results Phys.*, vol. 30, p. 104850, 2021.

[31] N. T. Fofang, T. H. Park, O. Neumann, N. A. Mirin, P. Nordlander, and N. J. Halas, "Plexcitonic nanoparticles: Plasmon-Exciton Coupling in Nanoshell-J- Aggregate complexes," *Nano Lett.*, vol. 8, no. 10, pp. 3481–3487, Oct. 2008.

[32] G. Zengin, M. Wersäll, S. Nilsson, T. J. Antosiewicz, M. Käll, and T. Shegai, "Realizing strong light-matter interactions between single-nanoparticle plasmons and molecular excitons at ambient conditions," *Phys. Rev. Lett.*, vol. 114, no. 15, p. 157401, Apr. 2015.

[33] R. Chikkaraddy *et al.*, "Single-molecule strong coupling at room temperature in plasmonic nanocavities," *Nat. 2016 5357610*, vol. 535, no. 7610, pp. 127–130, Jun. 2016.

[34] X. Han, K. Wang, X. Xing, M. Wang, and P. Lu, "Rabi Splitting in a Plasmonic Nanocavity Coupled to a WS2 Monolayer at Room Temperature," *ACS Photonics*, vol. 5, no. 10, pp. 3970–3976, 2018.

[35] S. Wang *et al.*, "Coherent coupling of WS2 monolayers with metallic photonic nanostructures at room temperature," *Nano Lett.*, vol. 16, no. 7, pp. 4368–4374, 2016.

[36] W. Liu *et al.*, "Strong Exciton-Plasmon Coupling in MoS2 Coupled with Plasmonic Lattice," *Nano Lett.*, vol. 16, no. 2, pp. 1262–1269, 2016.

[37] Y. M. Qing, Y. Ren, D. Lei, H. F. Ma, and T. J. Cui, "Strong coupling in two-dimensional materials-based nanostructures : a," 2022.

[38] A. Shalabney, J. George, J. Hutchison, G. Pupillo, C. Genet, and T. W. Ebbesen, "Coherent coupling of molecular resonators with a microcavity mode," *Nat. Commun. 2015 61*, vol. 6, no. 1, pp. 1–6, Jan. 2015.

[39] J. P. B. Mueller and F. Capasso, "Asymmetric surface plasmon polariton emission by a dipole emitter near a metal surface," *Phys. Rev. B - Condens. Matter Mater. Phys.*, vol. 88, no. 12, pp. 1–6, 2013.

[40] J. Petersen, J. Volz, and A. Rauschenbeutel, “Chiral nanophotonic waveguide interface based on spin-orbit interaction of light,” *Science (80-.).*, vol. 346, no. 6205, pp. 67–71, Oct. 2014.

[41] F. J. Rodríguez-Fortũno *et al.*, “Near-field interference for the unidirectional excitation of electromagnetic guided modes,” *Science (80-.).*, vol. 340, no. 6130, pp. 328–330, Apr. 2013.

[42] K. F. Mak and J. Shan, “Photonics and optoelectronics of 2D semiconductor transition metal dichalcogenides,” *Nat. Photonics*, vol. 10, no. 4, pp. 216–226, 2016.

[43] J. A. Schuller *et al.*, “Orientation of luminescent excitons in layered nanomaterials.,” *Nat. Nanotechnol.*, vol. 8, no. 4, pp. 271–276, Mar. 2013.

[44] D. Zheng, S. Zhang, Q. Deng, M. Kang, P. Nordlander, and H. Xu, “Manipulating coherent plasmon-exciton interaction in a single silver nanorod on monolayer WSe2,” *Nano Lett.*, vol. 17, no. 6, pp. 3809–3814, 2017.

[45] J. Wen *et al.*, “Room Temperature Strong Light-Matter Interaction with Active Control in Single Plasmonic Nanorod Coupled with Two-Dimensional Atomic Crystals,” *Nano Lett.*, vol. 17, no. 8, pp. 4689–4697, 2017.

[46] H. Chen, S. Deng, Y. Jiang, H. Wang, and S. Wen, “Resonance coupling in an individual gold nanorod-monolayer WS2 heterostructure: Photoluminescence enhancement with spectral broadening,” *ACS Nano*, vol. 14, no. 10, pp. 13841–13851, 2020.

[47] M. E. Kleemann *et al.*, “Strong-coupling of WSe2 in ultra-compact plasmonic nanocavities at room temperature,” *Nat. Commun.*, vol. 8, no. 1, 2017.

[48] S. Hou *et al.*, “Manipulating Coherent Light–Matter Interaction: Continuous Transition between Strong Coupling and Weak Coupling in MoS2 Monolayer Coupled with Plasmonic Nanocavities,” *Adv. Opt. Mater.*, vol. 7, no. 22, pp. 1–7, 2019.

[49] J. Sun *et al.*, “Light-Emitting Plexciton: Exploiting Plasmon- Exciton Interaction in the Intermediate Coupling Regime,” *ACS Nano*, vol. 12, no. 10, pp. 10393–10402, 2018.

[50] J. Qin *et al.*, “Revealing Strong Plasmon-Exciton Coupling between Nanogap Resonators and Two-Dimensional Semiconductors at Ambient Conditions,” *Phys. Rev. Lett.*, vol. 124, no. 6, p. 63902, 2020.

[51] S. Huang *et al.*, “Ultrasmall Mode Volumes in Plasmonic Cavities of Nanoparticle-On-Mirror Structures,” *Small*, no. 37, pp. 5190–5199, 2016.

[52] J. McKeever, A. Boca, A. D. Boozer, J. R. Buck, and H. J. Kimble, "Experimental realization of a one-atom laser in the regime of strong coupling," *Nat. 2003 4256955*, vol. 425, no. 6955, pp. 268–271, Sep. 2003.

[53] T. Volz *et al.*, "Ultrafast all-optical switching by single photons," *Nat. Photonics 2012 69*, vol. 6, no. 9, pp. 605–609, Aug. 2012.

[54] W. Chen *et al.*, "All-optical switch and transistor gated by one stored photon," *Science (80-.).*, vol. 341, no. 6147, pp. 768–770, Aug. 2013.

[55] A. Wallraff *et al.*, "Strong coupling of a single photon to a superconducting qubit using circuit quantum electrodynamics," *Nat. 2004 4317005*, vol. 431, no. 7005, pp. 162–167, Sep. 2004.

[56] Y. Zhou *et al.*, "Probing dark excitons in atomically thin semiconductors via near-field coupling to surface plasmon polaritons," *Nat. Nanotechnol.*, vol. 12, no. 9, pp. 856–860, 2017.

[57] B. W. Li *et al.*, "Large rabi splitting obtained in Ag-WS2 strong-coupling heterostructure with optical microcavity at room temperature," *Opto-Electronic Adv.*, vol. 2, no. 5, pp. 1–9, 2019.

[58] H. Li, M. Qin, Y. Ren, and J. Hu, " Angle-independent strong coupling between plasmonic magnetic resonances and excitons in monolayer WS 2 ," *Opt. Express*, vol. 27, no. 16, p. 22951, 2019.

[59] D. F. P. Pile and D. K. Gramotnev, "Channel plasmon–polariton in a triangular groove on a metal surface," *Opt. Lett.*, vol. 29, no. 10, p. 1069, 2004.

[60] I. V. Novikov and A. A. Maradudin, "Channel polaritons," *Phys. Rev. B - Condens. Matter Mater. Phys.*, vol. 66, no. 3, pp. 354031–3540313, 2002.

[61] A. Y. Nikitin, F. J. García-Vidal, and L. Martín-Moreno, "Oblique launching of optical surface waves by a subwavelength slit," *Phys. Rev. B - Condens. Matter Mater. Phys.*, vol. 83, no. 15, pp. 1–7, 2011.

[62] D. Xiao, G. Bin Liu, W. Feng, X. Xu, and W. Yao, "Coupled spin and valley physics in monolayers of MoS 2 and other group-VI dichalcogenides," *Phys. Rev. Lett.*, vol. 108, no. 19, pp. 1–5, 2012.

[63] X. Xu, W. Yao, D. Xiao, and T. F. Heinz, "Spin and pseudospins in layered transition metal dichalcogenides," *Nat. Phys.*, vol. 10, no. 5, pp. 343–350, 2014.

[64] B. Ding, Z. Zhang, Y. H. Chen, Y. Zhang, R. J. Blaikie, and M. Qiu, "Tunable Valley Polarized Plasmon-Exciton Polaritons in Two-Dimensional Semiconductors," *ACS Nano*, vol. 13, no. 2, pp. 1333–1341, 2019.

[65] J. Sun, H. Hu, D. Pan, S. Zhang, and H. Xu, "Selectively Depopulating Valley-

Polarized Excitons in Monolayer MoS2by Local Chirality in Single Plasmonic Nanocavity," *Nano Lett.*, vol. 20, no. 7, pp. 4953–4959, 2020.

[66] Y. J. Chen, J. D. Cain, T. K. Stanev, V. P. Dravid, and N. P. Stern, "Valley-polarized exciton–polaritons in a monolayer semiconductor," *Nat. Photonics 2017 117*, vol. 11, no. 7, pp. 431–435, Jun. 2017.

[67] S. Guddala, R. Bushati, M. Li, A. B. Khanikaev, and V. M. Menon, "Valley selective optical control of excitons in 2D semiconductors using a chiral metasurface [Invited]," *Opt. Mater. Express*, vol. 9, no. 2, p. 536, 2019.

[68] S. H. Gong, F. Alpeggiani, B. Sciacca, E. C. Garnett, and L. Kuipers, "Nanoscale chiral valley-photon interface through optical spin-orbit coupling," *Science (80-.).*, vol. 359, no. 6374, pp. 443–447, Jan. 2018.

[69] L. Sun *et al.*, *Separation of valley excitons in a MoS 2 monolayer using a subwavelength asymmetric groove array*, vol. 13, no. 3. Springer US, 2019.

[70] T. Chervy *et al.*, "Room Temperature Chiral Coupling of Valley Excitons with Spin-Momentum Locked Surface Plasmons," *ACS Photonics*, vol. 5, no. 4, pp. 1281–1287, Apr. 2018.

[71] Q. Guo, T. Fu, J. Tang, D. Pan, S. Zhang, and H. Xu, "Routing a Chiral Raman Signal Based on Spin-Orbit Interaction of Light," *Phys. Rev. Lett.*, vol. 123, no. 18, p. 183903, 2019.

[72] M. Cotrufo, L. Sun, J. Choi, A. Alù, and X. Li, "Enhancing functionalities of atomically thin semiconductors with plasmonic nanostructures," *Nanophotonics*, vol. 8, no. 4, pp. 577–598, 2019.

[73] P. A. Thomas, W. J. Tan, H. A. Fernandez, and W. L. Barnes, "A New Signature for Strong Light-Matter Coupling Using Spectroscopic Ellipsometry," *Nano Lett.*, vol. 20, no. 9, pp. 6412–6419, 2020.

[74] P. Vasa and C. Lienau, "Strong Light-Matter Interaction in Quantum Emitter/Metal Hybrid Nanostructures," *ACS Photonics*, vol. 5, no. 1, pp. 2–23, 2018.

[75] L. Zhang, R. Gogna, W. Burg, E. Tutuc, and H. Deng, "Photonic-crystal exciton-polaritons in monolayer semiconductors," *Nat. Commun. 2018 91*, vol. 9, no. 1, pp. 1–8, Feb. 2018.

[76] V. Savona, L. C. Andreani, P. Schwendimann, and A. Quattropani, "Quantum well excitons in semiconductor microcavities: Unified treatment of weak and strong coupling regimes," *Solid State Commun.*, vol. 93, no. 9, pp. 733–739, 1995.

[77] Z. He *et al.*, "Principle and applications of the coupling of surface plasmons and excitons," *Appl. Sci.*, vol. 10, no. 5, 2020.

[78] L. Novotny and B. Hecht, “Principles of nano-optics,” *Princ. Nano-Optics*, vol. 9781107005464, pp. 1–564, Jan. 2009.

[79] Y. Li *et al.*, “Measurement of the optical dielectric function of monolayer transition-metal dichalcogenides: MoS2, Mo S e2, WS2, and WS e2,” *Phys. Rev. B - Condens. Matter Mater. Phys.*, vol. 90, no. 20, 2014.

[80] G. Xu, M. Tazawa, P. Jin, S. Nakao, and K. Yoshimura, “Wavelength tuning of surface plasmon resonance using dielectric layers on silver island films,” *Appl. Phys. Lett.*, vol. 82, no. 22, pp. 3811–3813, 2003.

[81] A. A. Maradudin, I. Simonsen, J. Polanco, and R. M. Fitzgerald, “Rayleigh and Wood anomalies in the diffraction of light from a perfectly conducting reflection grating,” *J. Opt. (United Kingdom)*, vol. 18, no. 2, 2016.

[82] S. Y. Lee *et al.*, “Role of magnetic induction currents in nanoslit excitation of surface plasmon polaritons,” *Phys. Rev. Lett.*, vol. 108, no. 21, pp. 1–5, 2012.